NTNU – Trondheim
Norwegian University of
Science and Technology

Optical Properties and Composition of Fe:ZnS Films

Nelly-Ann Molland

Master of Science in Physics and Mathematics
Submission date: June 2014
Supervisor: Ursula Gibson, IFY

Norwegian University of Science and Technology
Department of Physics

Problem description

The goal of the thesis is to investigate optical and structural properties of Fe doped ZnS films deposited by vacuum co-evaporation for potential use in solar cells as a host material for an intermediate band device.

Master's thesis

Optical Properties and Composition of Fe:ZnS Films

Author:
Nelly-Ann Molland

Supervisor:
Prof. Ursula J. Gibson

NTNU – Trondheim
Norwegian University of
Science and Technology

Department of Physics,
The Norwegian University of Science and Technology
June 2014

Abstract

Iron doped ZnS thin films were deposited using the physical vapor deposition technique over a concentration range of 0-12% Fe. The thickness and composition of the films were measured with a profilometer and EDS, respectively, and confirmed a desired gradient composition of the films obtained by the geometrical separation of the zinc sulfide and iron sources. XPS revealed that Fe^{2+} had successfully substituted Zn^{2+} atoms, incorporating Fe in the ZnS structure while XRD and TEM indicated that the incorporation of Fe stabilizes small grain growth in the films. The latter technique confirmed a hexagonal structure.

Based on initial results, films made with Fe and ZnS were thought to be sulfur deficient and were annealed in a sulfur atmosphere. Additional Fe:ZnS films were deposited using FeS as iron source. However, poorer quality films were produced with this method since the films had a greater absorption and had non-uniform refractive indices.

The optical properties of the PVD films were measured and compared with those of films made under UHV conditions. Absorption studies of transmission measurements and various theoretical models were used to reveal an increase in absorption with increased Fe content, in addition to a broadened Urbach tail. The real part of the refractive index at a wavelength of 1000nm and the direct band gap of the films seemed to be unaffected by the doping level with estimated values of 2.29 and 3.5eV, respectively. While the real part of the refractive index is in agreement with published values, the direct band gap is lower than the theoretical values for ZnS. This is attributed to nano-crystalline grains found in the films.

A well isolated Fe^{2+} absorption at 2.7μm was observed for the thick films made under UHV conditions. This suggests that Fe:ZnS thin films may be useful material for saturable absorbers or mid-IR waveguide lasers.

Sammendrag

Jern-dopede tynnfilmer av Fe:ZnS med dopingkonsentrasjoner fra 0-12% er blitt deponert ved bruk av *physical vapor deposition* (PVD). Filmtykkelse og komposisjon er målt ved bruk av henholdsvis profilometer og EDS. Disse målingene bekreftet at en ønskelig gradient i filmkomposisjonene var oppnådd ved å skille sinksulfid- og jernkilden fra hverandre geometrisk under deposisjonen. XPS avslørte at jern hadde blitt innlemmet i ZnS strukturen ved en vellykket Fe^{2+} substitusjon av Zn^{2+} atom, mens XRD og TEM viste at de jern-dopede filmene bestod av små kornstørrelser. Den sistnevnte metoden avslørte en heksagonal filmstruktur.

Opprinnelige målinger viste at filmene deponert fra Fe og ZnS hadde et lavt innhold av svovel, og disse ble defor utsatt for *annealing* i svovelomgivelser. I tillegg ble flere filmer med FeS som jernkilde deponert. Disse filmene viste seg likevel å være av dårligere kvalitet enn de originale filmene, ettersom de hadde høyere absorpsjon og ikke-uniform brytningsindeks.

De optiske egenskapene til PVD-filmene ble målt og sammenlignet med de optiske egenskapene til filmer deponert under UHV forhold. Absorpsjonsstudier bestående av transmisjonsmålinger og ulike teoretiske modeller avslørte en økning i absorpsjonen med stigende jerninnhold, i tillegg til en utvidet *Urbach tail*. Realdelen av brytningsindeksen ved en bølgelengde på 1000nm samt det direkte bandgapet til filmene så ut til å være upåvirket av dopingnivået, med verdier estimert til henholdsvis 2.29 og 3.5eV. Mens realdelen av brytningsindeksen samsvarer med publiserte verdier, er det direkte bandgapet litt lavere enn teoretiske verdier for ZnS. Dette skyldes de nanokrystallinske kornene i filmen.

En godt isolert Fe^{2+} absorpsjon var observert ved 2.7 μm for de tykkere filmene deponert under UHV forhold. Dette antyder at Fe:ZnS tynnfilmer kan være et anvendelig materiale for *saturable absorbers* og *mid-IR waveguide lasers*.

Preface

This thesis is written as the final work for the degree of Master of Science at the Norwegian University of Science and Technology, under the 5 year engineering program of Physics and Mathematics. The thesis is concluding a specialization within Applied Physics, and are submitted to the Department of Physics at the Faculty of Science and Technology. It represents independent work over a 20 weeks period and is rewarded with 30 ECTS points.

Several people deserve an acknowledgement for their help during the weeks I have been working with the thesis. First of all I would like to send a special thank you to my fantastic supervisor Prof. Ursula Gibson, for being inspiring and enthusiastic in my work. She has always been available for great guidance and support, making her invaluable during the time I have been working on this project. A great thanks also goes to Eric Karhu for making me UHV films, in addition to being helpful in the lab and giving me good advices. I would also like to thank Zahra Ghadyani for helping me with ellipsometry measurements and for performing the subsequent modeling work, Mohammadreza Nematollahi for doing XPS measurements, Per Erik Vullum and Ruben Bjørge for investigating my samples with TEM and Julian Tolchard for his helpfulness at the XRD lab.

Contents

Chapter 1

Introduction

The annual consumption of energy in the world increased more than tenfold over the 20th century and is expected to increase further as the world population increases and the countries get more industrialized [[64], p.3]. Today, most of the energy comes from the fossil fuels coal, oil and gas, in addition to electricity from nuclear power. In addition to not being sustainable, the emissions from the combustion of the fossil fuel cause an increasing concentration of CO_2 in the atmosphere, enhancing the *greenhouse effect*. This will in turn lead to global warming, which could have adverse consequences considering the food production and water supply.

This is the worst case scenario, but to try to avoid situations like the one described above, it is important that renewable energy supplies are harnessed to a high extent, so that it could be replacing some of the unsustainable energy resources in the future.

Why not try to increase the harnessing of the most important energy source in the world, the sun? Already as early as in 1894, what believed is the first large area solar cell was prepared by Charles Fritts, by pressing a layer of selenium between gold and another metal [[10], p.2]. In 1954, Chapin, Fuller and pearson reported that the first silicon solar cell was demonstrated, which converted sunlight into electrical energy with an efficiency of 6%.

Today, silicon is the foremost photovoltaic material, and the typical efficiency of commercially produced solar cells of crystalline silicon lies in the range 13-16 % [[65], p.130]. The theoretical efficiency of conventional single junction solar cells are calculated to be 40.7 % under full concentrated light, and 31% under unconcentrated light [62], [66]. These common cells are examples of *first generation* solar cells [67].

For the past 25 years the, thin film technology has been an important factor in the development of the *second generation* solar cells. With the thin film solar cells the production costs was reduced, and mass production was enabled. An efficiencies of 22.8% has been demonstrated for a CIGS thin film solar cell [59].

A large increase in efficiency characterizes the *third generation* solar cells. This generation involves intermediate band solar cells (IBSC) and tandem cells, and common for these cells are that they contain several band gaps in order to utilize more of the solar energy. The theoretical efficiency of cells with multiple band gaps, involving a tandem cell with an infinite stack of independently operated cells or IBSCs with an infinite number of IBs, is 86.8% under concentrated sunlight [67].

Fe doped ZnS is an interesting candidate for IBSC, as several authors have reported a possibility of engineering the band gap of the material by adjusting the doping level [5], [6] [8]. An opportunity of tuning the band gap and the favorable large absorption coefficients of Fe:ZnS, would indicate that this material may also be useful in photoconversion both as absorber and window materials [5], [6]. In 2011 the first continuous wave Fe^{2+} doped ZnS laser was reported by Kozlovsky et. al. with a tunable wavelength range of 3.49 - 4.65 μm, a region enabling new applications of lasers in non-invasive medical diagnostics and environmental monitoring among others [25].

In this project thin films of Fe:ZnS has been deposited and investigated, with focus on optical properties, to see if Fe:ZnS could be identified as a potential candidate for IBSC.

Chapter 2

Theory

2.1 Energy bands

In this section fundamentals of energy bands are presented. It contains a description of how the value of the energy gap divides materials into semiconductors, insulators and metals and how this is related to electron bonding. Additionally, the difference between a direct- and indirect band gap is given, as well as the principles of doping and creation of a pn-junction, explained in terms of the Fermi energy level. This theory forms a basis for the understanding of direct- and indirect band gaps estimated for Fe:ZnS films with different doping levels, presented in section 5.3.3.

Solids are divided into different types of material, depending on its properties. One important property is the energy band gap, and in order to see how other properties depend on the band gap it is useful to have a closer look at the formation of energy bands. A reasonable way to start is to discuss the energy level of isolated atoms. Two isolated identical atoms have identical discrete energy levels, whose values are dependent on the quantum number of the orbital angular momentum l. When these atoms are brought together, however, they start interacting and the result is splitting of the energy levels. This energy splitting is the only way of fulfilling the Pauli exclusion principle, which states that two electrons in a given interacting system can not occupy the same quantum state. Thus, each energy level that now belongs to the atom pair is occupied with at most one electron. As a solid consists of many atoms the number of splittings within a level becomes so large, that the difference in energy of the splitted levels is comparable to the thermal energy. This causes the energy level to become a continuous energy band with allowed states for the electrons. The energy gap E_g refers to the distance between two such bands, and it is also given an additional name "forbidden band", as there are

no allowed energy levels for electrons to occupy in the case of a perfect crystal. The lower band is called the valence band (VB) while the upper band is called conduction band (CB). The process of electrons filling the energy states and the size of the band gap are essential in distinguishing different types of materials as we will see [[13], p. 59-61].

2.1.1 Semiconductors, insulators and metals

A semiconductor is a material which has a conductivity that is higher than for insulators, but less than metals. The band gap in a semiconductor is typically ∼2 eV. This means that it is possible for electrons in the VB to be excited to the CB if the electron has a sufficient amount of energy corresponding to the width of the band gap. In cases where electrons are excited across the band gap the material is conducting. The band gap of the insulating materials is too wide compared to the thermal energy of the electrons, in order for the electrons to get excited across the band gap, and these materials have zero conductivity. Metals on the other hand, have a much higher conductivity than insulators and semiconductors. This is due to overlapping of the VB and the CB, which results in electrons that are free to move in the presence of an electric field, and thereby could participate in an electric current. A sketch illustrating the prinsiples of the three types of materials is found in figure 2.1.

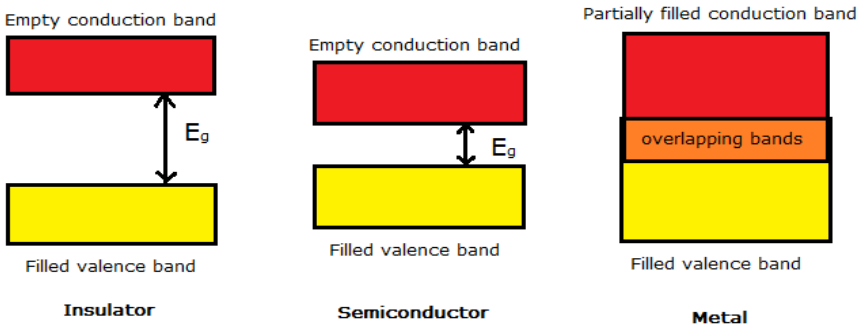

FIGURE 2.1: The material is considered to be an insulator when the VB is filled with electrons while the CB is empty. It behaves as a semiconductor if the VB is filled and the CB is empty at zero temperature, and if one or both of the allowed bands are slightly filled or slightly empty at finite temperature. In the third case of a metal, one or both of the allowed bands are partially filled. Based on [[11], figure 1 p.162].

Ionic crystals like NaCl is an example of a good insulator [[13], p. 56-57]. The Na-atom belongs to group I in the periodic table of elements which means that one electron occupy the outer shell. As the atoms prefer a filled outer shell the Na-atom gives up its outer electron to the Cl-atom. Cl belongs to group VII, and by receiving the eighth outer electron from Na, the Cl-atom now has a filled outer shell. The resulting Na^+ and Cl^- ions are attracted by electrostatic forces and form a ionic crystal. Since both of the ions have a closed-shell configuration there are no loosely bound atoms to participate in a current, which makes NaCl, and ionic crystals in general, good insulators.

In a metal, the atoms have only partial filled outer shells, usually by no more than three electrons. The atoms give these loosely bound electrons away to the crystal, so that the solid is made up of ions with closed shells surrounded by a sea of free electrons. Forces from the interaction of positive ion cores and the free electrons form a metallic bonding which holds the lattice together. When an electric field is applied the free electrons move around, and this makes metals good conductors.

Ge and Si exhibit the diamond lattices structure and are examples of semiconductors. Both elements belong to group IV, which means that they have four electrons in the outer shell. In the diamond structure each atom is surrounded by four nearest neighbouring atoms, and each of them share their four valence electrons with these neighbours. Between the shared electrons, quantum mechanical interactions occur, giving rise to binding forces. These forces are known as covalent binding forces, and each covalent bond is consituted by an electron pair, which now only belong to the bond, not the atoms. What makes these crystals semiconductors and not insulators, is the fact that the electrons can be excited by thermal or optical processes out of the covalent bond, so that they can be free to participate in a current flow. This is not the case for the diamond consisting of carbon, because of the strong bonds between the C-atoms.

In addition to elemental semiconductors from group IV like Si and Ge, which consist of only one type of atoms, there are also compound semiconductors consisting of elements within group IV like SiGe, or compounds of different groups like GaAs or ZnS. GaAs is a common III-V semiconductor, while ZnS is an example of a II-VI semiconductor. Compound semiconductors do not necessarily have covalent bondings only, there are also compounds where both covalent and ionic bonds are present [[13], p. 57-58]. The appearance of ionic binding forces becomes more important the further separation of the elements of the compound in the periodic table, in accordance with the increasing difference in electronegativity of the components.

2.1.2 Electron bonding and energy bands

Semiconductors containing a significant amount of ionic bonds exhibit large energy gaps. The bonding electrons are close to the atoms, so the bonds between the electrons of the different atoms are considered to be rather weak. This means that the interaction between the atoms are low, which leads to large a large energy gap. The II-VI compound ZnSe, which has a large energy gap of 2.7 eV confirms this connection [[13], p.524].

Another material property that depends on the energy gap is the size of the lattice constant in the crystal structure. Semiconductors with small lattice constants, exhibit strong interatomic forces and the outermost electrons are strongly bound to the lattice, which leads to a large band gap energy [[14], p.3]. This can be shown by comparing properties of Si crystals and diamond. In diamond the lattice constant is smaller than that of other materials with diamond crystalline structures. The interatomic separation of 1.544 Å between the C atoms is about 2/3 of the Si-Si separation [[14], p.61]. By comparing the energy gap of the same crystals, it is seen that the energy gap of diamond is 5 eV while Silicon has a band gap of 1.1 eV, which makes diamond an insulator and Silicon a semiconductor [[13], p.61]. The band gap of Ge which lies underneath C and Si in periodic table in the same group, is 0.67 eV [[13], p.524]. What is seen based on this section, is a tendency of increasingly large energy bands for semiconductors composed of light elements and for materials having a large degree of ionic bonding [[14], p.5].

2.1.3 Direct and indirect band gaps

As seen in the above section, the band gap is an important property that determines what type of material one is dealing with. By definition, the fundamental band gap E_g is the minimum amount of energy that which will promote an electron from the VB to the CB [[10], p.50-51], and light is a preferrable energy source for this purpose. The energy of light is inversely proportional to the wavelength of the propagating light. Similar proportionality yields for the wave function of the electron. The energy of the electron is proportional to the wave vector $\vec{k}$, of which the electron wave function propagates, and it is inversely related to the wavelength λ of the wavefunction through $k = 2\pi/\lambda$.

By plotting the energy of the band edges with respect to the wave vector, a band structure diagram of the material is created. By looking at the band structure, like the one in figure 2.2, one could tell whether the band gap is direct or indirect. In the case of a material with direct band gap the minimum energy of the CB and the maximum energy of the VB occur at the same $\vec{k}$-value, and in order to excite an electron across the

forbidden band a photon of energy E_g is sufficient. A photon of energy E_g on its own is however not sufficient to excite an electron from the VB to the CB in a material with indirect band gap. In this case the maximum VB and the minimum CB do not occur at the same value of the wave vector, therefore an additional phonon with the appropriate k-vector is required in the excitation process. A sketch of the band structure of both direct- and indirect bands is shown in figure 2.2.

The phonon, which is a lattice vibration, transfers its momentum to the photon in

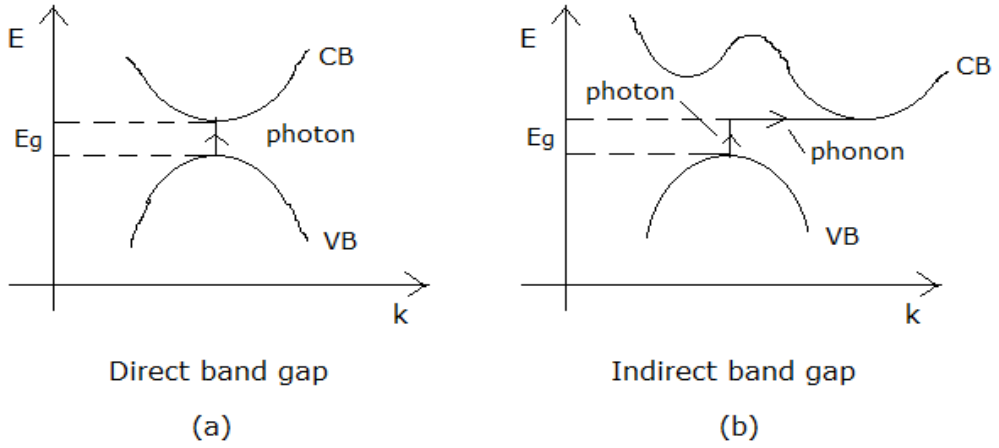

FIGURE 2.2: (a) shows a sketch of the band structure of a direct band gap semiconductor, where a photon of energy E_g is sufficient to excite an electron from the VB to the CB. (b) illustrates the band structure of an indirect band gap semiconductor. Here a phonon of correct k-value is required in addition to a photon of minimum energy of E_g in order to excite an electron across the forbidden band. Based on [[10], figure 4.5 p.162].

the same moment as the photon is absorbed by the material so that both energy and momentum are conserved in the process. Since a certain value of k-vector is required in order to excite an electron across the forbidden band in the indirect band gap materials, the absorption is generally weaker for these materials compared with the direct band gap materials where only photons with energies higher than E_g are required. It is thus convenient to study the absorption when determining whether the material has a direct- or indirect band gap. The absorption of different wavelengths is related to the transmission of light in the material through the equation [[10], p.88]

$$I(x) = I_0 e^{-\alpha x}, \tag{2.1}$$

where I is the intensity of the transmitted light at depth x in the material with uniform absorption coefficient α, and I_0 is the intensity of the incident light. Hence, by measuring the intensity of the transmitted light, the absorption can be calculated when the thickness of the material and the intensity of the incident light are known.

The absorption could further be used in determining the band gap of the semiconductor, and the following relation between the absorption coeffisients and photon energies for a material with direct band gap is

$$(\alpha hv)^2 \sim hv, \tag{2.2}$$

while for a material with indirect band gap the relation changes to

$$(\alpha hv)^{0.5} \sim hv. \tag{2.3}$$

Here h is the Plancks constant, v is the frequency of the light and α is the wavelength dependent absorption coefficient [6]. By plotting these relations with respect to the photon energy hv in a Tauc plot the value of the band gap E_g is found in the intersection of the linear regression with the energy-axis [37], [12].

2.1.4 The Fermi energy level

The Fermi energy level is an important term in order to understand the effect of doping, as this term is used to explain how introducing impurities into a material could effect the band gap and cause smearing of band gap edges.

At zero temperature the VB is completely filled and the CB is completely empty. This could be understood by looking at the electrons and how they occupy energy states. Electrons with no kinetic energy occupy the available states with the lowest energy, and keep filling up the available states until the Fermi energy level is reached. The Fermi level is defined as the level that has a 50% occupation of electrons, and it could be shifted as the material is exposed to external influence. In metals, the Fermi level corresponds to the the upper energy limit of the electron states that can be occupied at zero temperature.

In order to excite electrons to states of higher energies than the Fermi level, the electrons need kinetic energy, which they have at finite temperatures. The probability of occupation of an allowed electron state of any energy E, is given by the Fermi-Dirac distribution $f(E)$:

$$f(E) = \frac{1}{1 + \exp\frac{E - E_F}{kT}} \tag{2.4}$$

where k is the Boltzmanns constant, T is the temperature and E_F is the Fermi energy

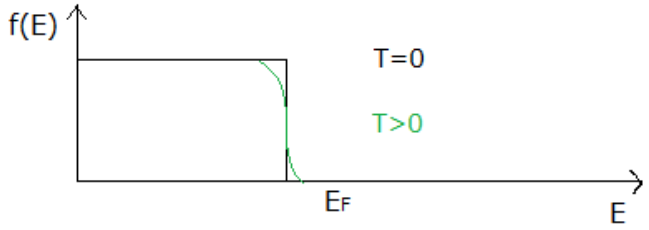

FIGURE 2.3: The plot of the Fermi-Dirac distribution shows that at zero temperature T the probability of occupation of a state with higher energy than E_F is equal to zero. When the kinetic energy of the electrons increases, indicated with temperature, there is a small chance that energy states with energies higher than E_F are occupied. [[10], based on figure 3.8 p.57].

level [[10], p.56]. In a semiconducting material the Fermi level lies in the forbidden band and in the case of a perfect, intrinsic semiconductor the Fermi level is positioned in the middle of the band gap. When the Fermi level is positioned in an allowed band, the material is no longer considered as a semiconductor, but rather as a metal, due to the resulting high conductivity. A graphical representation of the Fermi-Dirac distribution is shown in figure 2.3, and it illustrates the increasing probability of excitation as the kinetic energy of the electrons increases. The increase of kinetic energy is a result of thermal- and optical processes, which include increasing the ambient temperature and the amount of incident photons being absorbed by the material.

2.1.5 Doping

A common way to increase the probability of exciting electrons from the VB to the CB is to introduce dopants in the material. When elements are introduced in the semiconductor, which add extra holes or electrons in the material, it is said to be p-doped or n-doped, respectively. Acceptors are the elements that give the material excess of holes, which is a term used for vacant electron positions in the outer shell of an atom, and the donors are the elements that result in excess of electrons. A desired result of the doping is that the position of the Fermi level is changed, according to figure 2.4. As the figure illustrates, the Fermi level moves closer to the CB in n-doped materials. In these materials electrons occupy states with energy up to the donor level which is lower than the energy of the CB, but significantly higher than the energy of the VB. By using the argument that all donor states are filled at zero temperature, it is determined that the Fermi level must lie between the donor level and the lower energy of the CB [[10], p.62], see figure 2.4. Similarly, the Fermi level is closer to the VB in p-doped

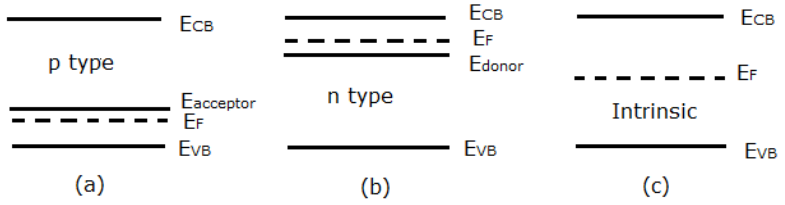

FIGURE 2.4: The position of the Fermi level is dependent on the impurity level. (a) The Fermi level is close to the VB in a p type material, (b) in the n type the Fermi level is positioned close to the CB, (c) while in an undoped intrinsic semiconductor the Fermi level lies in the middle of the band gap. Based on [[10]], figure 3.12 p.65.

materials, between the VB and the acceptor energy level which occurs as elements with excess of holes are introduced to the lattice. In both cases the conductivity increases, and by heavy doping impurity states close to the VB and the CB edges will effectively reduce the band gap such that less energy is required in order to excite electrons across the forbidden band [[10], p. 64-65]. The drawback is however, that heavy doping also increase the probability of an electron being recombined with a hole or being trapped in a defect state, increasing the resistivity of the material.

2.1.6 Pn-junction

When a p-doped material is combined with a n-doped material, a pn-junction appears at the intersection. A sketch of a pn-junction in figure 2.5 also illustrates that the n-side of the junction has a high density of electrons while there is a high density of holes on the p-side. To obtain a more stable condition the charges diffuse from high density to low density, hence the electrons go from the n-side to the p-side, in order to fill the holes on the p-side, and this leaves behind new holes on the n-side. In this way an electric field is established from the n-side to the p-side, as seen in figure 2.5. The electric field opposes further diffusion across the junction, by drifting electrons back towards the n-side and holes towards the p-side. When the drifting balances the diffusion an equilibrium condition is set. As described in section 2.1.5 concerning doping, the Fermi level lies close to the VB in the p-doped material, and close to the CB in the n-doped material. When these two materials are put together and form a pn-junction, the Fermi level stays constant through the junction at equilibrium. In order to have a constant Fermi level in the junction a so called band bending occurs [[10], p.126, 146]. This is illustrated in figure 2.5. The region where the bending occurs is called the depletion region, and within this region the material carries a net charge, which in turn establishes an electric

field as described above. The regions beyond the depletion layer are neutral [[10], p. 149].

In the case where an external voltage is applied or electrons are excited by photons, the system is driven away from equilibrium and the Fermi level is split into two quasi Fermi levels [[10], p. 66-69]. The splitting of the Fermi level occurs as a result of an increase in density of both holes and electrons, in the VB and the CB, respectively, due to the external disturbance. When the densities are increased above the equilibrium values, a single Fermi level is not enough to explain the charge distribution, hence one Fermi level E_{Fn} is needed in the description of distribution of electrons in the CB, and another Fermi level E_{Fp} is needed in the description of distribution of holes in the VB. Light or other disturbances that cause the Fermi level to split have now created a voltage that is equal to the difference in the quasi Fermi levels far from the junction, divided by the elementary charge [[10], p. 127]. In the case where the n-doped and p-doped material is the same, the junction is called a homojunction, and it is said to be a heterojunction if it consists of two different materials with different band gaps.

2.2 Principles of a solar cell

The energy gap is an important parameter when considering materials to be used in solar cells. As seen in the following section giving a presentation of the principles of the conventional-, intermediate- and multijunction solar cell, different band gap values and junctions are preferred in order to optimize the efficiency of the different solar cells.

The concept of the solar cell, e.g. photovoltaic cell, is converting solar energy into electric energy. Briefly speaking, this photovoltaic energy conversion results from charge generation, charge separation and charge transport [[10], p.119]. Incoming photons from the sunlight hitting the solar cell are absorbed by electrons, which get excited, and generate charges in terms of a electron-hole pair, and these charges are separated by a pn-junction [[10], p.145]. The pn-junction introduces asymmetry in resistance that drives the holes and electrons towards the contacts of an external circuit, and by connecting a load to this circuit the cell produces both current and voltage that could do electric work. The pn-junction is a classical model of a solar cell although other junctions like the p-i-n junctions, multijunctions or electrochemical junctions could be used for the same purpose.

In order to maximize the efficiency of the solar cell the number of photons that contribute to power generation needs to be maximized. One also need to make sure that the band gap of the semiconductor corresponds to the wavelengths with the highest intensity. It

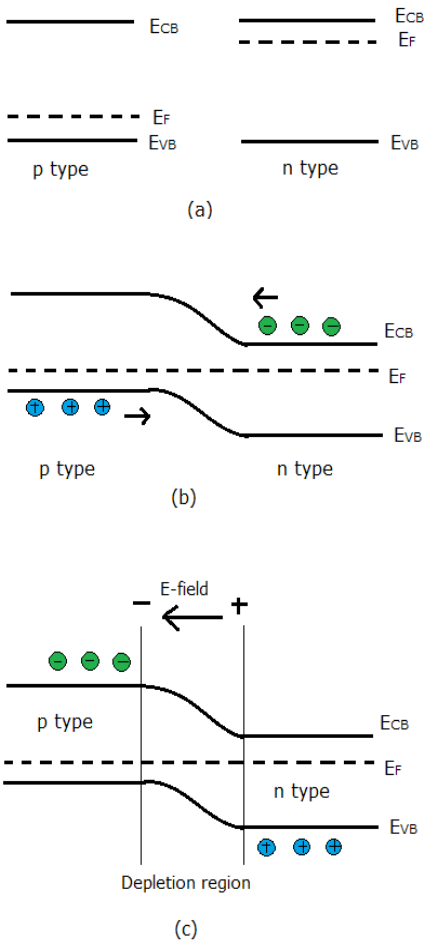

FIGURE 2.5: (a) shows the energy levels of a p-junction and an n-junction separated, (b) shows how electrons and holes drift/diffuse across the intersection of the two junctions brought together establishing a pn-junction, and (c) shows the the pn-junction in the equilibrium state, where an electric field is established in the depletion region. Based on [[10]], figure 3.8 p.57.

can be seen from the solar spectrum in figure 2.6 that the highest intensities are given by photons of wavelengths 400-600nm in the range of visible light, which corresponds to the energies 2-3eV. It is thus important to design the solar cell to have a band gap below this range when high efficiency is desirable, since only light of energy $hv > E_g$ will contribute to excitation of electrons. The photons of energy below E_g are transparent to the material with this band gap energy and will not be absorbed.

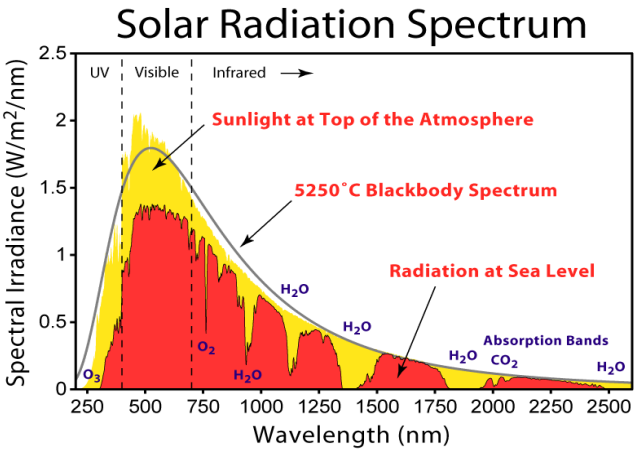

FIGURE 2.6: The solar spectrum from the sun. The yellow area represents the spectrum at top of the atmosphere, while the red area shows the spectrum at sea level. By comparing the spectrum at these levels the absorption in the atmosphere is given. The figure is taken from [36].

2.2.1 Principles of the multijunction solar cell

The multijunction solar cell is an attempt of utilizing as much as possible of the solar spectrum [[10], p.297-299]. As the name implies it contains multiple junctions of different band gaps that are stacked in optical series, with the purpose of extracting a higher power from the same spectrum. In order to maximize the power conversion, subcells are designed to have specific band gaps since the maximum power efficiency is obtained when the band gap energy is equal to the energy of the incident photon. The theoretical maximum efficiency of a conventional solar cell under full concentrated light is 40.7% while that of a two-terminal tandem cell is 55.4% [62].

2.2.2 Principles of the intermediate band solar cell (IBSC)

The IBSC is another photovoltaic concept that is developed with the purpose of extracting as much energy of the solar spectrum as possible, making the IBSC a high-efficiency solar cell just like the multijunction solar cell. In an IBSC, one or more intermediate bands (IB) are present in a single material, resulting in multiple band gaps over which electrons are excited under illumination of the cell. The IBs might be a result of the band structure or it could be introduced via impurities or quantum heterostructures, which introduce electronic levels into the band gap. Placing the IB material between a p-emitter and an n-emitter in a p-i-n junction an IBSC could be created [39], and unlike the conventional solar cell the electron populations in the different bands of the IBSC each form a quasi Fermi level in a quasi thermal equilibrium [[10] p. 303].

A sketch of an IB material with two CBs and a single VB is shown in figure 2.7. This

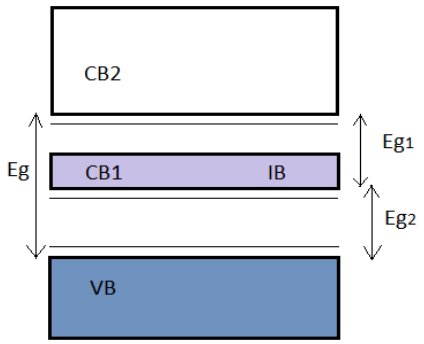

FIGURE 2.7: A sketch of the energy band diagram of a material with one IB, with three resulting band gaps. The sketch is based on figure 10.11 in [[10] p. 305].

IB system contains three band gaps. In addition to the excitation of electrons from the VB to the upper CB2 across the band gap E_g, which is the possible transition in a conventional solar cell, there are two other possible excitations where the IB is involved. In these excitations electrons move from the VB into CB1 and from CB1 into CB2, crossing the corresponding band gaps E_{g2} and E_{g1}, respectively. The notations of the different bands and band gaps follow from figure 2.7.

In order to maximize the efficiency of the IBSC, the photons should only be used to excite the electrons over the largest band gap they are capable of crossing. This could be achieved with careful choice of absorption coefficients, where the smallest band gap should have the smallest absorption coefficient. With optimal absorption coefficients and band gap values of $E_{g1} = 0.7$eV and $E_g = 1.93$eV the maximum theoretical efficiency of an IBSC with one IB is calculated to 63.1% [62].

2.3 Reflection and transmission

The optical characterization of the films in this project involves measurements of the reflection and transmission and subsequent modeling to retrieve values of the complex refractive index, as seen in section 5.3. In the section below, a decription of information contained in n and κ is given. The fundamentals of polarization, which form the basis of ellipsometry is presented, in addition to a detailed description of the reflection and transmission of a thin film.

2.3.1 The complex refractive index

The refractive index $\tilde{n} = n + i\kappa$ consists of a real part n, and an imaginary part κ, containing a lot of information about the optical properties of a material. The complex representation makes it convenient to describe light propagating in a medium, when there are losses due to absorption. By relating the complex refractive index to the wavenumber $\tilde{k} = 2\pi\tilde{n}/\lambda$ and inserting it into the expression of a plane wave given by the electric field component propagating in $\vec{z}$-direction, the following relation is obtained [[15], p.128]:

$$\vec{E}(z,t) = \vec{E_0}e^{i(\vec{\tilde{k}}z-\omega t)} = \vec{E_0}e^{i(\frac{2\pi}{\lambda}(n+i\kappa)z-\omega t)} = e^{(-\frac{2\pi\kappa z}{\lambda})}\vec{E_0}e^{i(\vec{k}nz-\omega t)}. \tag{2.5}$$

The amplitude $\vec{E_0}e^{(-\frac{2\pi\kappa z}{\lambda})}$ is seen to be exponentially attenuated with respect to the travel distance z, due to the absorption in the material. Since the intensity is being proportional to the square of the amplitude, the resulting attenuation constant, also known as the absorption coefficient α, can be written as

$$\alpha = \frac{4\pi\kappa}{\lambda} \tag{2.6}$$

showing that κ is proportionally related to the absorption.

From equation 2.5, the real refractive index n is seen to describe the oscillation of the wave, representing the phase velocity v_{phase} by the relation $n = c/v_{phase}$, where c is the speed of light in vacuum.

In addition to describe the behaviour of a propagating wave, the refractive index is used to express the amount of light being transmitted and reflected, when it travels from one medium to another. These relations are known as the Fresnel equations and are found by equation 2.18, 2.19, 2.20 and 2.21 in section 2.3.3, where the transmission and the reflection are described in detail.

As well as the refractive index determines the amount of light being transmitted across an interface between two media, it also contains information about the angle of which the transmitted light is refracted. With θ_1 being the angle between the intersection of the materials and the incoming light, the angle θ_2 of which the light is being refracted could be found by Snells law yielding

$$n_1 \sin\theta_1 = n_2 \sin\theta_2, \tag{2.7}$$

where n_1 and n_2 are the refractive indices of the respective media.

The fact that there is a wavelength dependency in n, $n(\lambda)$, known as dispersion, causes light consising of different wavelengths being refracted at slightly different angles. Passing light through a prism which results in splitting the light into a rainbow of colours, illustrates the wavelength dependency in n. It also shows how n being wavelength dependent can be utilized in monochromators.

2.3.2 Polarized light

Light is electromagnetic waves in the wavelength range 380nm - 740nm [[15] p. 72]. The exact form of the light is called the state of polarization, which could be defined by the behaviour of the vector of the electric field $\vec{E}(\vec{z},t)$ observed at a fixed point in space $\vec{z}$ at time t [[51] p.1].

In the case of a linear polarized wave, the vector of the electric field is described as

$$\vec{E}(z,t) = \vec{E}_x(z,t) + \vec{E}_y(z,t) \tag{2.8}$$

with the constitutionals

$$\vec{E}_x(z,t) = \hat{\mathbf{i}} E_{0x} \cos(kz - \omega t) \tag{2.9}$$

$$\vec{E}_y(z,t) = \hat{\mathbf{j}} E_{0y} \cos(kz - \omega t + \epsilon) \tag{2.10}$$

which imply that the magnitude of the electric field vector $\vec{E}$ changes with time and position. In the expressions above, ω is the frequency of the oscillating waves while ϵ is the relative phase difference between the waves, both propagating in the z-direction. When ϵ is zero or an integer multiple of $\pm 2\pi$ the waves are said to be in phase, and if ϵ is an odd integer multiple of $\pm\pi$ the waves are 180° out of phase. Figure 2.8 (a) shows a two-dimentional sketch of a linearly polarized electric field oscillating back and forth in the first and third quadrants [[15] p.325-326].

For circular polarized light, which is illustrated in figure 2.8 (b) the constituent waves given in equation 2.9 and 2.10 have equal amplitudes, $E_{0x} = E_{0y} = E_0$, and a relative phase difference $\epsilon = -\pi/2 + 2m\pi$, where m is an integer. Accordingly, the constituent waves become

$$\vec{E}_x(z,t) = \hat{\mathbf{i}} E_0 \cos(kz - \omega t) \tag{2.11}$$

$$\vec{E}_y(z,t) = \hat{\mathbf{j}} E_0 \sin(kz - \omega t) \tag{2.12}$$

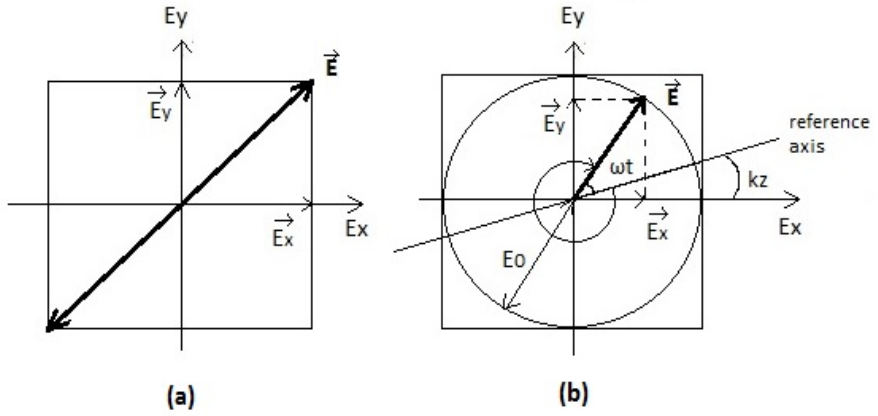

FIGURE 2.8: (a) shows the electric field linearly polarized in the first and the third quadrants. (b) illustrates the rotation of the electric field vector of a right-circularly polarized wave. Based on [[15]], figure 8.1 and 8.4 p.326-327.

with the resultant wave:

$$\vec{E} = E_0[\hat{\mathbf{i}}\cos(kz - \omega t) + \hat{\mathbf{j}}\sin(kz - \omega t)]. \tag{2.13}$$

When a wave of such polarization is moving towards an observer, this electric field vector $\vec{E}$ is seen to be rotating clockwise at an angular frequency ω, and it is referred to as right-circular light. In the case where $\epsilon = \pi/2 + 2m\pi$ with m being an integer, the electric field vector can be written as

$$\vec{E} = E_0[\hat{\mathbf{i}}\cos(kz - \omega t) - \hat{\mathbf{j}}\sin(kz - \omega t)]. \tag{2.14}$$

A sign change of the sinus term compared to equation 2.13 would lead to a counter-clockwise rotation of the electric field vector making the wave left-circularly polarized.

The linearly- and circularly polarized light are considered to be special cases of elliptical polarized light, as the resultant electric field vector $\vec{E}$ of this light is both rotating and changing in magnitude with respect to time and position. Based on the expressions for the curve traversed by the tip of $\vec{E}$ given by

$$E_x = E_{0x}\cos(kz - \omega t) \tag{2.15}$$

$$E_y = E_{0y}\cos(kz - \omega t + \epsilon) \tag{2.16}$$

the equation of an ellipse could be derived:

$$\left(\frac{E_y}{E_{0y}}\right)^2 + \left(\frac{E_x}{E_{0x}}\right)^2 - 2\left(\frac{E_x}{E_{0x}}\right)\left(\frac{E_y}{E_{0y}}\right)\cos\epsilon = \sin^2\epsilon, \tag{2.17}$$

and this expression shows that the endpoint of $\vec{E}$ will trace out an ellipse in the xy-plane as the wave propagates in the z-direction, as illustrated in figure 2.9 [[15] p.325-329].

In the case where the overall polarization changes in an unpredictable fashion and so

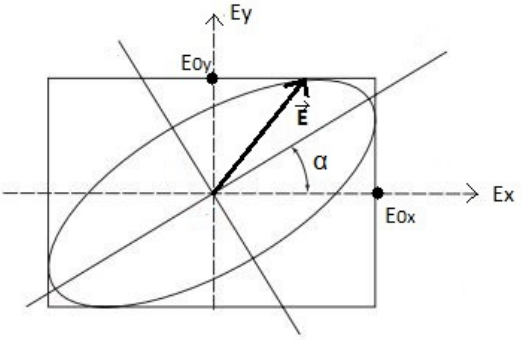

FIGURE 2.9: A sketch of elliptical polarized light. After one rotation, the endpoint of the electric field vector traces out an ellipse. In the figure, the ellipse is making an angle α with the (E_x, E_y) coordinate system. Based on [[15]], figure 8.6 p.329.

rapidly that a polarization state can not be measured, the light is said to be *natural* or *unpolarized*, and this is the case for the light that comes from the sun [[15] p.325-330]. By letting unpolarized light pass through socalled polarizers the light will become polarized in one of the states discussed above, depending on the polarizer. The polarizers come in many different configurations, but they are all based on one of the physical mechanisms (1) dichroism, which refers to selective absorption of one of the E_x- or E_y-component of the incident wave, (2) birefringence, which involves double refraction of light when passing through a medium, (3) reflection or (4) scattering [[15] p.332-333].

2.3.3 Waves at an interface

When light hits a boundary between two different media at an oblique incident angle, it is convenient to look at the p-polarized and s-polarized state of the electromagnetic wave. These polarizations are orthogonal to each other, where the electric field of the p-polarized wave is parallel to the plane of incidence, and the electric field of the s-polarized wave is perpendicular to the plane of incidence. The plane of incidence is defined as the plane spanned by the propagation vectors $\vec{k}$ of the incoming, reflected

and transmitted wave. A sketch of the two polarization states at an interface is shown in figure 2.10.

From Maxwell's equations the boundary conditions can be derived, and these states

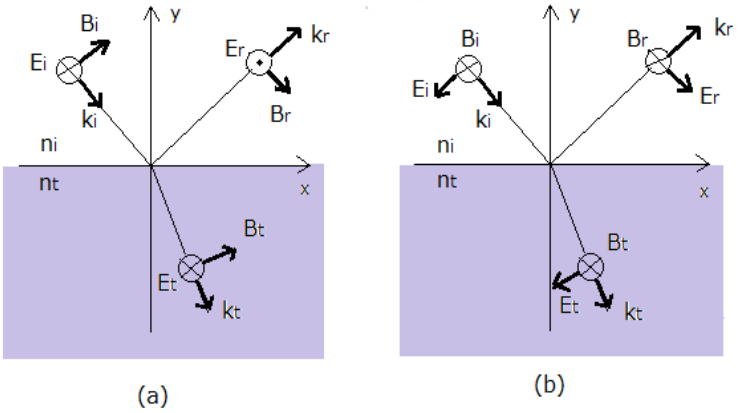

FIGURE 2.10: The figure shows an electromagnetic wave incident on a boundary, where (a) shows the field orientation of an s-polarized wave, while (b) shows the field orientation of a p-polarized wave. The magnetic field is denoted as B, the electric field as E, with the subscripts i, r and t indicating if the wave is incoming, reflected or transmitted, respectively. The xy-plane constitute the plane of incident, and n is the refractive index of the media. Based on [[15]], figure 4.43 p.117.

that the tangential components of both the electric and magnetic fields are continuous across the boundaries [[15] p. 427]. The boundary conditions together with the relations between the electric- and magnetic field given by the Maxwell equations, are used in the derivation of the expressions of the reflection r and transmission t of the electromagnetic waves on a single interface, known as the Fresnel equations [[15] p. 114-115]:

$$r_s \equiv \left(\frac{E_{0r}}{E_{0i}}\right)_s = \frac{n_i \cos\theta_i - n_t \cos\theta_t}{n_i \cos\theta_i + n_t \cos\theta_t} \tag{2.18}$$

$$t_s \equiv \left(\frac{E_{0t}}{E_{0i}}\right)_s = \frac{2n_i \cos\theta_i}{n_i \cos\theta_i + n_t \cos\theta_t} \tag{2.19}$$

$$r_p \equiv \left(\frac{E_{0r}}{E_{0i}}\right)_p = \frac{n_t \cos\theta_i - n_i \cos\theta_t}{n_i \cos\theta_t + n_t \cos\theta_i} \tag{2.20}$$

$$t_p \equiv \left(\frac{E_{0t}}{E_{0i}}\right)_p = \frac{2n_i \cos\theta_i}{n_i \cos\theta_t + n_t \cos\theta_i}, \tag{2.21}$$

where r_p, r_s, t_p and t_s are the reflection and transmission coefficient from the p-polarized and s-polarized wave, respectively. In these equations n_i and n_t are the refractive indices

of the incident and transmitting media respectively, while θ_i and θ_t are the incident angle and the angle at which the wave is transmitted, respectively.

While the reflection from the s-polarized wave r_s can never be zero, the reflection from the p-polarized wave r_p can be zero if the condition $\theta_i + \theta_t = 90°$ is fulfilled. In this case the wave is completely transmitted and the incident angle is known as Brewster's angle θ_B.

The Fresnel reflections of the p-polarized and the s-polarized light can be used to express the complex reflection ratio ρ, which in turn is determined by measuring the amplitude component Ψ and the phase difference Δ of the reflected wave:

$$\rho = \frac{r_p}{r_s} = \tan(\Psi)e^{i\Delta}. \tag{2.22}$$

This equation forms a basis for ellipsometry, a technique used for determination of optical constants of thin films, involving measurements of Ψ and Δ and subsequent model analysis, described in section 4.2.8.

2.3.4 Reflection and transmission of thin films

When the reflection and transmission of a thin film coated on a substrate are investigated, two interfaces must be taken into consideration, leading to the expressions of R and T being a little more complicated. A sketch of the different reflections occuring for such a two-layer-structure is shown in figure 2.11.

In order to obtain an expression for the total reflection and transmission, a suitable indexing of the parameters should be introduced. Using the notations given by figure 2.11, air corresponds medium 0, the film corresponds to medium 1 while the substrate corresponds to medium 2. Their respective refractive indices are denoted as n_0, n_1 and n_2. The amplitudes of the reflection and transmission at the different interfaces follow the indexing of the media with r_{01}, r_{10} and r_{12} representing the amplitude of the reflections from the air-film, film-air, and film-substrate interfaces, respectively, while the amplitudes of the respective transmission are represented by t_{01}, t_{10} and t_{12}.

As a wave propagates through the film with thickness d it undergoes a phase shift given by $\delta = \frac{2\pi}{\lambda} d \cos\theta_{ii}$ [[45], p. 81]. This could be expressed by a phase factor $p = e^{-i\delta}$ for a wave propagating the film once. For the second reflection, whose amplitude is given as $t_{01}t_{10}r_{12}$ according to figure 2.11, the phase factor becomes p^2, as the wave propagates the film twice, while that of the third reflection is represented by p^4.

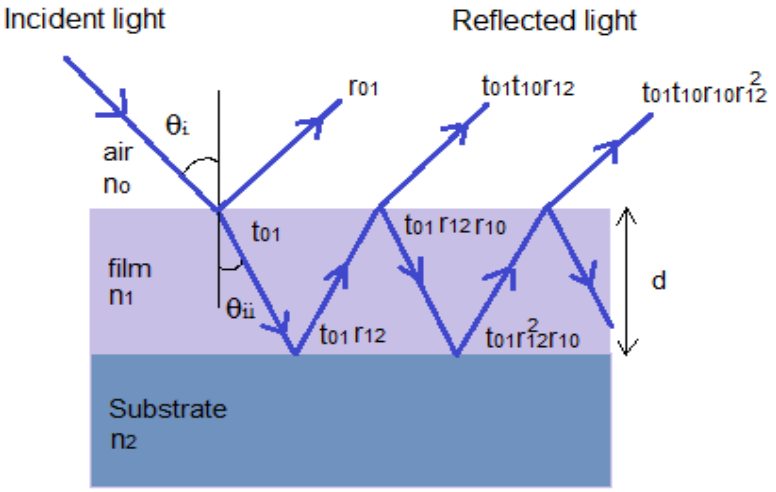

FIGURE 2.11: An sketch of the different reflections that are present in a thin film system. Based on [[15], figure 9.37 p. 417].

In order to obtain the total amplitude of the reflectivity of the two-layer-structure, the amplitudes of the reflectance at all the interfaces including phase factors must be added. Based on the notation introduced in the previous paragraphs the summation becomes:

$$r = r_{01} + t_{01}t_{10}r_{12}p^2 + t_{01}t_{10}r_{10}r_{12}^2p^4 + t_{01}t_{10}r_{10}^2r_{12}^3p^6... \tag{2.23}$$

(involving the four strongest reflections). This expresses a geometric series and by using the relation $r_{01} = -r_{10}$ a rewriting gives

$$r = \frac{r_{01} + r_{12}p^2}{1 + r_{01}r_{12}p^2}. \tag{2.24}$$

Correspondingly, the amplitude of the total transmission can be expressed as

$$t = \frac{t_{01}t_{12}p^2}{1 + r_{01}r_{12}p^2}. \tag{2.25}$$

Finally, the ratios of the reflected and transmitted light to the incident light are each given by the product of the respective amplitudes and their complex conjugate of the amplitude,

$$R = rr^* = \frac{r_{01}^2 + 2r_{01}r_{12}\cos 2\delta + r_{12}^2}{1 + 2r_{01}r_{12}\cos 2\delta + r_{01}^2r_{12}^2} \tag{2.26}$$

$$T = tt^* = \frac{n_2t_{01}^2t_{12}^2}{1 + 2r_{01}r_{12}\cos 2\delta + r_{01}^2r_{12}^2}. \tag{2.27}$$

Chapter 3

Background

3.1 ZnS

ZnS is a II-VI semiconductor. This material occurs naturally in the two different crystal structures Zincblende and wurtzite, which are cubic and hexagonal structures, respectively [1]. Because of this dualism, ZnS can also exist in a polymorphous state [9]. The Zincblende structure is the most stable structure at room temperature, and it transforms into wurtzite at 1020°C [28]. In both structures each Zn atom is connected to four S atoms in a tetrahedral arrangement, with a mixed bonding of covalent and ionic binding forces between the atoms [[13], p. 58]. An increasing amount of ionic bonds in the semiconductor would lead to an increase of the interelemental forces, which in turn could lead to shorter distances between the atoms. As a result, the crystal structure would change from Zincblende to wurtzite. Since the energy gap increases with the amount of ionic bonds in a semiconductor, this could explain why the bandgap is crystal structure dependent [[14], p. 3]. This could be confirmed by looking at ZnS, which has a band gap of 3.84 eV in the cubic structure, and a bandgap of 3.94 eV in the hexagonal structure [1].

The wide bandgap makes ZnS transparent from the ultraviolet (UV) to the infrared (IR) region. This transparency combined with chemical and thermal stability makes ZnS attractive for many applications [3]. The wide bandgap makes this semiconductor attractive as an antireflection coating for heterojunction solar cells [2], host material in solid states lasers [4], as well as a promising host material for ultraviolet light-emitting diode [7]. When doping ZnS with transition metals (TM) like Cr^{2+}, Ni^{2+} and Fe^{2+} intermediate bands have been shown, which makes ZnS a promising host material in IBSC [27]. Introducing TM in ZnS has also shown to affect the band gap of the material. This

suggests the possibility of tailoring the band gap [32], which is an important factor in the development of high efficiency solar cells.

3.2 Thin films

Thin films have a number of application areas, for example as photovoltaic material in solar cells [[10], p. 211]. A motivation for the ongoing research in this field, is to find photovoltaic materials of good quality, which can be grown more cheaply than the expensive single crystals in conventional solar cells. Suitable candidates like amorphous silicon (a-Si) and polycrystalline cadmium telluride (CdTe) have been produced by physical or chemical deposition techniques, which satisfy mass production. A higher absorption of light is preferable for the thin film semiconductors compared to the bulk materials, as the efficiency of a photovoltaic cell is dependent on the amount of incident photons being absorbed by the semiconductor. In other words high absorption reduces the cell thickness. However, silicon which is among the most widely used semiconductors in conventional solar cells, does not absorb light as strongly as other materials suitable for thin film photovoltaics. Several materials of II-VI binary compounds and I-III-VI ternary compounds have proven high optical absorption relative to silicon, and have been used for thin film photovoltaics, including CdTe, $CuInGaSe_2$ (CIGS) and $CuInSe_2$ [[10], p. 213]. A maximum efficiency of $CuInGaSe_2$ thin film solar cell is reported to be 22.8 %, which is close to the efficiency of a commercial conventional silicon solar cell [59].

Another important application of thin films, is as an anti reflection coating on the front surface of the solar cell. Both the thickness and the refractive index of the material are important parameters in the selection of an appropriate anti reflection coating in order to capture as much relevant incident light as possible and thereby maximize the photocurrent generation [[10], p. 180]. ZnS is a good candidate for this purpose and as a host material for novel concept solar cells [60], [27].

3.2.1 Thin film ZnS deposition

The optical and structural properties of a material are dependent on growth conditions and growth technique. A few common techniques for thin film deposition include chemical vapor deposition (CVD) [16], chemical bath deposition (CBD) [17], [18] and physical vapor deposition (PVD) [19]. Kumar *et al.* used PVD to deposit ZnS thin film on glass substrates that were held at temperatures 200° and 250° [19]. XRD measurements of these films confirmed the wurtzite structure of ZnS, and the authors reported that the films showed good transparency exhibited by an interference pattern. A band gap of

3.50 eV was calculated, which is significantly smaller than the 3.94 eV band gap reported for the bulk wurtzite [1].

ZnS thin films grown by chemical bath deposition on glass and SiO_2 were reported for the first time by Luque *et al.* [18]. Properties of ZnS films grown with different deposition times were studied. It was concluded that the ZnS films on glass substrates were homogenious and compact, while the films grown on SiO_2 had a non-homogenious morphology due to an insufficient amount of Zn^{2+} and S^{2-} ions. Furthermore, the band gap was determined to be 3.62 eV, which is related to a high transparency of 80% in the visible range. XRD analysis of the ZnS on SiO_2 revealed a Zincblende structure.

In optical studies of semiconducting sulphide and selenide thin films, Nkum *et al.* reported that the small grain sizes in the chemically deposited films would lead to a higher energy gap in the films when compared to the single crystals of the films. The small grain sizes were shown to cause a quantum well structure or electrical isolation of individual grains. In this study the energy gap of ZnS was determined to be 3.72 eV [21].

A typical problem which often occurs by using the chemical bath method, is the presence of oxygen molecule impurities in the film, in which ZnO and $Zn(OH)_2$ has been reported [29]. Nkum *et al.* observed a low activation energy in oxygen contaminated ZnS films, and suggest that this energy could correspond to the energy required for the transition between the trap levels of the impurities and the CB of the film [21].

3.2.1.1 Effect of annealing on structure and energy gap

An annealing process could be carried out to reduce the oxygen contamination in ZnS films. Ahn *et al.* post-annealed Zn(S,O) thin films grown by CBD at temperatures up to 300°C for one hour, which proved to reduce the amount of Zn-O bonds while the number of Zn-S bonds was increased. A decrease of about 71% of the concentration ratio of Zn-O/Zn-S was reported, without any change in the crystallinity. However, the purpose of annealing is often to improve the crystallinity of the material, which happens by increasing the grain sizes in the sample [31]. It has been demonstrated a change of ZnS from amorphous to polycrystalline phase [23] and an improved crystallinity of polycrystalline CdO after annealing of the thin films at 500°C in vacuum for 1 hour [30]. In an electrodeposited Fe_x:$Zn_{1-x}S$ thin film the average grain sizes were 300, 400 and 700 nm after annealing in argon atmosphere for 5 minutes at 285, 350 and 450°C, where the largest grain size was determined when x=0.33 [6]. XRD measurements confirmed

the improved crystallinity at higher annealing temperatures in terms of sharper and narrower peaks in the XRD spectrum.

A change in crystallinity also suggests a change of the optical band gap in a material. Several works have demonstrated that the band gap decreases with increasing annealing temperature and in the review of Ates *et al.* it was reported that the band gap of a CBD grown ZnS film decreased from 3.73 eV to 3.57 eV after annealing in nitrogen atmosphere at 250°C in three minutes [22], [23]. These results could be attributed the increase in crystallinity. In the same review it was reported that the energy gap was also decreasing with increasing thickness, which is explained by an increased grain size and the fact that some of the impurity levels from the edge of the CB can inoculate with the CB when the thickness of the film is increased.

3.3 Doped ZnS/ZnO

Additional elements introduced into a material, change its properties. This can be done on purpose by doping impurities into a crystalline environment. However this could also generate the undesired presence of defects. In the following sections, a number of effects generated by the appearance of impurities in ZnS and ZnO reported in the literature, are presented. In addition, examples of how doped ZnS could be applicable in IBSC and lasers are shown.

3.3.1 Fe doped ZnS

In recent years transition metal doped chalogenides have been a hotspot in scientific research, where new low-cost and nontoxic chalogenide-based semiconductors are in development. The properties of these materials make them applicable in lasers and sensors, in addition to electroluminescent and photoluminescent devices, which constitute an important, growth area of technology [6].

Studies show that ZnFeS thin film is an applicable material in photoconversion systems, both as absorber and optical window materials due to wide tuneability of the band gap and favorable large absorption coefficients [5], [6]. A wide tuneablilty is demonstrated, when combining FeS_2 and ZnS with band gaps of 0.95 eV and 3.58 eV, respectively, in ZnFeS thin films made by electrochemical deposition on tin oxide substrates [5]. As the Fe concentration in the film was increased, resulting band gap values from 3.1 eV to 0.37 eV were demonstrated. The decrease in the value of the band gap with increasing Fe content in ZnFeS thin film is also demonstrated in several other reviews [6], [8].

When iron is introduced in the zinc sulfide lattice, the Fe^{2+} atoms are substitute with Zn^{2+} atoms in a tetrahedrally coordinated S^{2-} environment [9]. In order to see how the electronic structure changes as Fe atoms are incorporated to the lattice, Feng *et al.* used X-ray Photoelectron Spectroscopy (XPS) to study the binding energies of the Zn 2p, Fe 2p and S 2p core lines and VB spectra of ZnS and ZnFeS compounds that were grown by low-pressure metalorganic chemical vapor deposition. The results from the measurements suggest that the bond strength of Fe-S is more covalent than Zn-S, which in turn could affect the band gap energy [8]. The band gap was decreased with increasing Fe content in the films, and simultaneously the crystal structure changed from hexagonal to cubic structure.

A demonstration of how the size of the band gap depends on the crystal structure of an electrodeposited Fe_x:$Zn_{1-x}S$ thin film is given by Kashout *et al.* [6]. In this work the structure and band gaps of films with different Zn/Fe ratio were studied, after annealing in 5 minutes at 285, 350 and 450°, respectively, in an argon atmosphere. XRD measurements revealed the presence of hexagonal pyrrhotite $Fe_{1-y}S$ and cubic pyrite structure FeS_2 in the films with high Fe content, and these films were determined to have low band gap values of 0.26 and 0.7 eV at 285 and 450°, respectively. The band gap value showed a slight increase with increasing Zn concentration, due to a formation of a cubic sphalerite phase, ZnS. The abrupt transition into the sphalerite phase, which

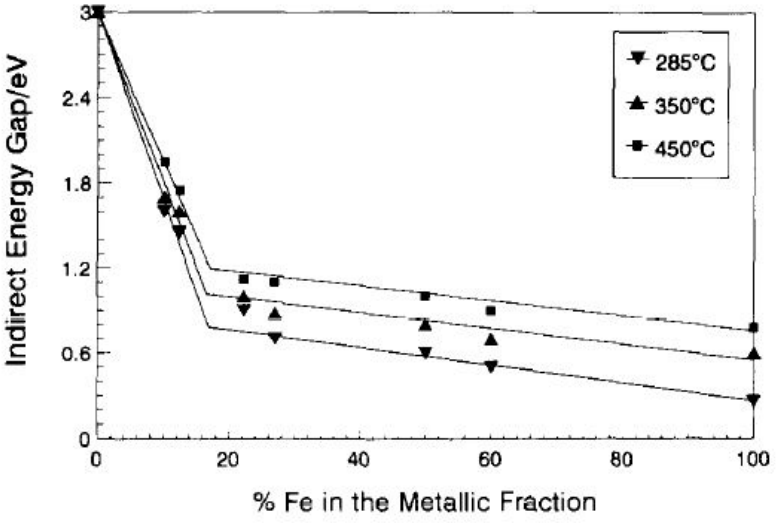

FIGURE 3.1: The variation of the bandgap with the iron percentage in the metallic fraction (Zn+Fe) of Fe_x:$Zn_{1-x}S$ thin films at different annealing temperatures. The authors assumed an indirect energy gap. This is figure 11 in [6].

is dominating at high Zn concentrations, is observed in terms of a rapid increase of

the energy gap for Fe_x:$Zn_{1-x}S$ at x$\sim$ 17% in figure 3.1, which shows the variation of the energy gap of the films at different Zn/Fe ratios and different anneling temperatures.

From the figure it is also observed that the increase of the annealing temperature has little effect on samples having high Zn concentrations, due to the absence of phase transitions. At smaller Zn concentrations, on the other hand, the appearance of phase transitions seems to be influenced by an increase of the annealing temperature, which in turn is observed to lead to a larger indirect band gap [6].

3.3.2 $ZnO_{1-x}S_x$

Another way to change the band gap of ZnS is to replace the S-atom rather than to substitute Zn^{2+} with TM^{2+}. Persson *et al.* studied the VB and CB of ZnS doped with O, and calculated the resulting band gaps of $ZnO_{1-x}S_x$ at different values of x [33]. The calculations reveal a strong VB offset at small S concentrations, whereas the CB only shows a weak increase. Large concentrations of S, on the other hand, reveal a strong CB offset while there is only a small increase of the VB. A schematic presentation of the band offsets are given in figure 3.2. The strong offset of the maximum value of the VB (VBM) is caused by ZnS-like bonds in the ZnO host material, and by looking at the density of states (DOS) of $ZnO_{0.89}S_{0.11}$ given in figure 3.3, this offset can be explained. As shown by the figure, the maximum energy value of the filled states of $ZnO_{0.89}S_{0.11}$ is $\sim$0.25 eV higher than of ZnO. Simultaneously, the minimum value of the CB seems to be approximately the same for $ZnO_{0.89}S_{0.11}$ as for ZnO, hence the band gap decreases with small contributions of S in ZnO. This review illustrates the importance of measuring the oxygen content in ZnS film materials.

3.3.3 Impurities and defects in Fe:ZnO

In an investigation of structure and formation energies of various defects in Fe-doped ZnO nanoparticles using the first-principle calculation, Xiao *et al.* reported increased iron doping up to a level of 18.25 at.% increased the stabilization of ZnO nanoparticles [42]. It was demonstrated that the Fe atoms preferred to be homogeneously distributed in the nanoparticles and that generation of Fe islands inside the ZnO lattice was shown to be energetically unfavorable. Substitutional doping was seen to be strongly favored and doping ZnO with Fe was reported to have small effects on the ZnO structure.

Furthermore, it was reported that the presence of composite defects, which involved interstitial O and Zn vacancies could not be excluded since their lattice parameters

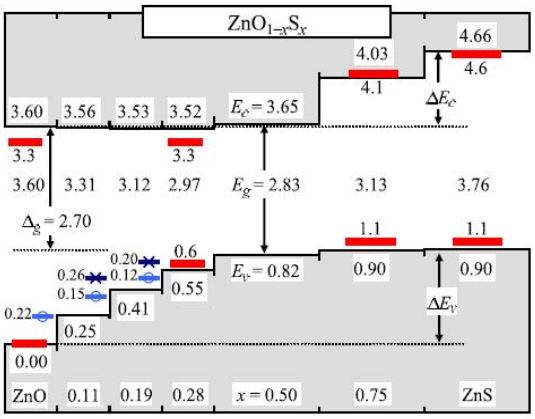

FIGURE 3.2: A sketch of the calculated energies of valence band, E_v, conduction band E_v and the band gap E_g of $ZnO_{1-x}S_x$ at different values of x. A large offset of the VB $E_v(x)$ is calculated for x <0.5, while the $E_c(x)$ value of the CB is nearly unchanged. At x>0.5 there is a large $E_c(x)$ offset of the CB, whereas the $E_v(x)$ of the VB increases only weakly. The smallest band gap is calculated at equal concentrations of S and O, and increases as the concentration ratio S/O changes. All energy values are given in units of eV, referred to $E_v(ZnO)$=0 eV, and with an estimated error bar of ±0.05 eV. This is a figure from [33].

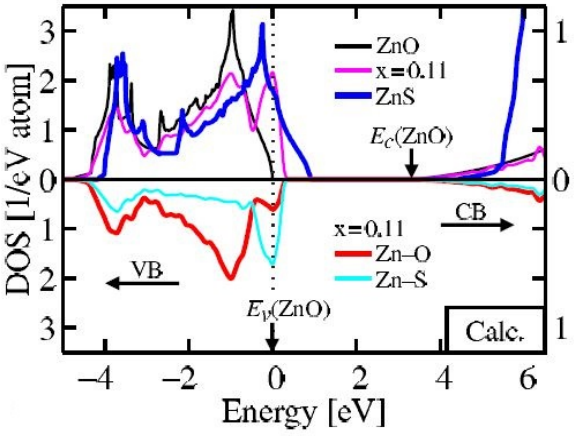

FIGURE 3.3: The calculated total DOS and the atomic-resolved DOS for a Zn-S and Zn-O dimer in $ZnO_{0.89}S_{0.11}$. The VBM of $ZnO_{0.89}S_{0.11}$ is calculated to be higher than that of ZnO and lower than the VBM of ZnS. The figure is given by [33].

when bonded to Fe was seen to be only slightly altered. This was in spite of the demonstration of Zn vacancies and interstitial O atoms introducing extra stress in the Fe:ZnO lattice, making it less stable. XRD measurements of pure and Fe-doped ZnO nanoparticles synthesized using the flame spray pyrolysis technique, revealed that an increased crystal disorder with increased amounts of Fe added to the nanoparticles, indicated a presence of defects.

3.3.4 Fe and Co impurities in ZnS

A presence of impurities could cause undesired effects of the properties of a material, with quenching of luminescence being an example. After addition of Fe^{2+} into ZnS nanowires, Wei *et al.* reported on quenching of the emission intensity of the nanowires prepared by the hydrothermal method at 180° [41]. The Fe^{2+} impurity states were identified as nonradiative centers positioned in the energy bandgap of the ZnS host, supported by the observation of no Fe-related emission peak appearing in the photoluminescence (PL) spectrum.

In addition of being a luminescence "killer", Fe^{2+} has also been demonstrated by Sharma *et al.* to decrease the life time of the emission in ZnS:Mn [40]. In PL studies of ZnS:Mn, ZnS:Mn,Fe and ZnS:$Mn_{(0.20)}$, Co nanophosphors prepared using a chemical precipitation method, the Fe and Co impurities of concentrations 0.5-1% were seen to decrease the life time of the emission in ZnS:Mn, with increasing impurity level, and the effect of Fe was reported to be comparable less than that of Co. Multiple trapping levels were responsible for radiative emission, and the different impurities were demonstrated to contribute from different centers in the band gap of the host material. Due to the small impurity concentrations a significant quenching of the luminescense was not observed. Decreasing the life time could be seen as a positive effect of impurities, regarding opto-electronic applications.

3.3.5 Urbach tails caused by disorder

An empirical rule for the optical absorption coefficient α, associated with the band gap in disordered solids was proposed by Urbach in 1953 [75]. From the rule which states $\alpha(E) = \alpha_0 e^{(E-E_1)/E_0}$, where E_0, E_1 and α_0 serve as fitting parameters while E is representing the photon energy, the Urbach tail is expressed when $n = 1$ in the exponent $(E-E_1)^n$ [71]. The corresponding Urbach energy E_U refers to the width of the exponential absorption edge [74]. Several authors have reported an appearance of Urbach tails in the optical absorption near the band gap attributed to optical transitions between the band edge states and some defects states in materials having thermal or structural disorder of different origins [71], [74], [76].

Kim *et al.* reported an increase in the Urbach energy with increasing doping level of Indium in ZnO thin films [74]. The In-doped ZnO films were deposited by sol-gel spin-coating method, and showed a decrease in the direct band gap as a larger amount of In was introduced into the films. Simultaneously, an increase in E_U was observed,

making the increasing In content responsible for the decreasing width of localized states in the optical band of the In:ZnO films. In this way, the E_U value was inversely changed with the band gap of the films, as illustrated in figure 3.4.

In addition of doping elements being the factor causing disorder resulting in the presence

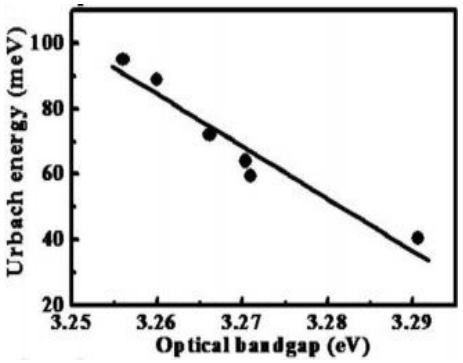

FIGURE 3.4: The figure shows how the value of the Urbach energy change inversely with the direct band gap of In-doped ZnO thin films. An increasing doping level is shown to be responsible for a decrease in the direct band gap and the corresponding increase in Urbach energy. The figure is a part of figure 6 in [74].

of an Urbach tail, also crystal grain sizes are seen to be significant in studies of this tail. In the studies of the tails of Urbach-Martienssen type in chemically deposited ZnSe and CdSe quantum dots in thin film form, Pejova reported a decrease in the Urbach energy with increasing particle size [76]. Thermal annealing was used in order to increase the size of the particles, and the reduction in E_U due to the increasing particle size was attributed a decrease in the density of dislocations, relaxation of the lattice strain and hence the degree of structural disorder.

3.3.6 Intermediate bands (IB) in TM:ZnS compounds

Partial filled intermediate bands (IB) in TM:ZnS compounds at TM= Cr^{2+}, Fe^{2+} and Ni^{2+} were reported by Zhang *et al.* in their investigation of the electronic structures and optical properties of different TM:ZnS systems [27]. Observation of total spin polarizations of wurtzite TM_x:$Zn_{1-x}S$ at $x = 0.028$, revealed an isolated partial filled IB close to the Fermi level for the three TM dopants. Thus, by incorporating Cr^{2+}, Fe^{2+} or Ni^{2+} in the ZnS crystal, electron transitions from VB to IB, and futher from IB to CB are permitted. This leads to a more efficient photon absorption, and this makes TM:ZnS compounds promising candidates for high efficiency solar cells and other opto-electronics devices.

In figure 3.5 the absorption coefficients of ZnS doped with different TMs are shown

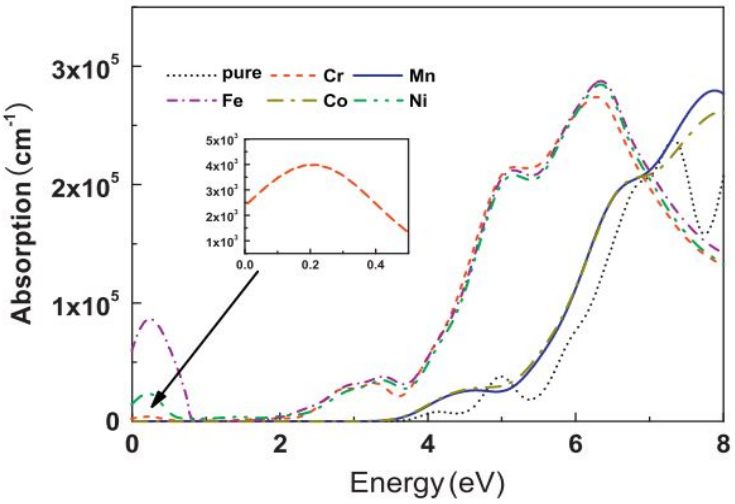

FIGURE 3.5: The absorption coefficients of TM:ZnS where TM corresponds to the transition metals Cr^{2+}, Mn^{2+}, Fe^{2+}, Co^{2+} and Ni^{2+}. There is an obvious red shift of the absorption peaks for Cr^{2+}, Fe^{2+} and Ni^{2+} and the distinct absorption peaks in the visible region between 2.0 to 3.5 eV are due to the interband transition between the $TM-3d$ and $S-2p$ conduction bands of the three TMs. The figure is taken from [27].

[27]. It is observed, an evident shift towards smaller wavelengths in the absorption spectra of Cr^{2+}, Fe^{2+} and Ni^{2+} doped films compared to pure ZnS and ZnS doped with Mn^{2+} and Cd^{2+}, where an IB was not obtained. The presence of IB in Cr^{2+}, Fe^{2+} and Ni^{2+} doped ZnS becomes apparent in the absorption peak in the visible region between 2.0 to 3.5 eV. This peak corresponds to the transition of the $TM-3d$ electron in the IB to the S-2d electron state in the CB. Looking at slightly higher energies, the absorption edge of pure ZnS is found at 3.63 eV in agreement with the experimental band gap value of 3.77 eV. A clear absorption edge for the TM:ZnS systems containing IB, however, does not seem to be obtained in this work.

A computation done by Saeed *et al.* showed a direct band gap of 1.58 eV in the $Zn_{0.75}Fe_{0.25}S$ compound, and the incorporation of Fe^{2+} in ZnS was demonstrated to give a larger decrease in the value of band gap than compared to incorporation of Ni^{2+} and Co^{2+}, which were calculated to have band gaps of 1.85 eV and 1.63 eV, respectively [32]. The dopant concentration was the same for all three ions. Common for the compounds mentioned, is that the Fermi level is located inside the impurity band, a property that makes the alloys half metallic. The half metallic band gaps of $Zn_{0.75}Fe_{0.25}S$, $Zn_{0.75}Ni_{0.25}S$ and $Zn_{0.75}Co_{0.25}S$ were 0.4 eV, 0.0 eV and 0.1 eV, respectively.

It is evident from the results in [27] that the absorption can be remarkably modulated by TM-doping, which would also indicate the potential applications in optical systems.

3.3.7 TM:ZnS in IBSC

The optimum band gap for a single junction cell is determined to be 1.39 eV, a value which is a result of a trade-off between a favorable low band gap maximizing the photon absorption efficiency and a desired high band gap maximizing the output voltage from the photovoltaic (PV) cell [34]. As seen in the previous section, decreasing size of the band gap of ZnS by TM-doping has successfully been demonstrated to give band gap values close to the optimal value for PV applications like IBSC. A band gap value of 1.58 eV has been determined in a first principle calculation of $Zn_{0.75}Fe_{0.25}S$ [32], while a band gap of 1.45 eV was reported by Kashyout *et al.* for an electrodeposited thin film of $Fe_{0.12}$:$Zn_{0.88}S$ [5].

In order to determine a suitable doping concentration several factors need to be taken into consideration. Too large doping concentrations have shown to broaden the IB such that it merges with the VB or CB, which would lead to solar cells of low efficiency. This supports the fact that formation of an IB is most probable for low dopant concentrations. However, it is important that the concentration is sufficiently high so that the impurities form a band and not a level [35].

3.3.8 Fe:ZnS in lasers

TM^{2+} doped wide gap semiconductor crystals were for the first time suggested and demonstrated for middle-infrared (mid-IR) lasing, as late as in 1996 [26]. Since then, the interest of TM doped II-VI compounds as host crystals in lasers has grown extensively, and in 2011 the first continuous wave Fe^{2+} doped ZnS laser was reported by Kozlovsky *et al.* with a tunable wavelength range of 3.49 - 4.65 μm [25]. Lasing in this mid-IR region provides new applications of lasers in non-invasive medical diagnostics and environmental monitoring among others, as these lasers operate over the "molecular fingerprint" which lies in the range from 2-15 μm.

When Fe^{2+} is incorporated in ZnS, it is substituting the Zn^{2+} atoms in a tetrahedrally coordinated S^{2-} environment forming a $Zn_{1-x}Fe_xS$ compound. The incorporated atom lies in the crystal field of the ZnS host, and this field splits the the ground term ^5D of the $Fe^{2+}(3d^6)$ ions into triplet $^5T_2$ and doublet ^5E. The only allowed transition is the transition $^5T_2 \leftrightarrow {}^5E$ between these two states. The large energy splitting of the ^5D

term featured by ZnS results in an absorption band and emission band shifted towards lower wavelengths for ZnFeS than other II-VI compounds doped with Fe^{2+}, and this gives ZnFeS unique spectroscopic characteristics. Cr^{2+} also attracts great attention as a dopant in ZnS. The energy splitting is similar to that of Fe^{2+}, but the absorption and emission band are shifted towards even shorter wavelengths compared to Fe^{2+} due to a larger crystal splitting. The absorption and emission band of Fe^{2+} and Cr^{2+} doped crystals corresponding to $^5T_2 \leftrightarrow {}^5E$ are shown in figure 3.6 [24].

Dual doped wide band gap materials are also of interest for laser development [38].

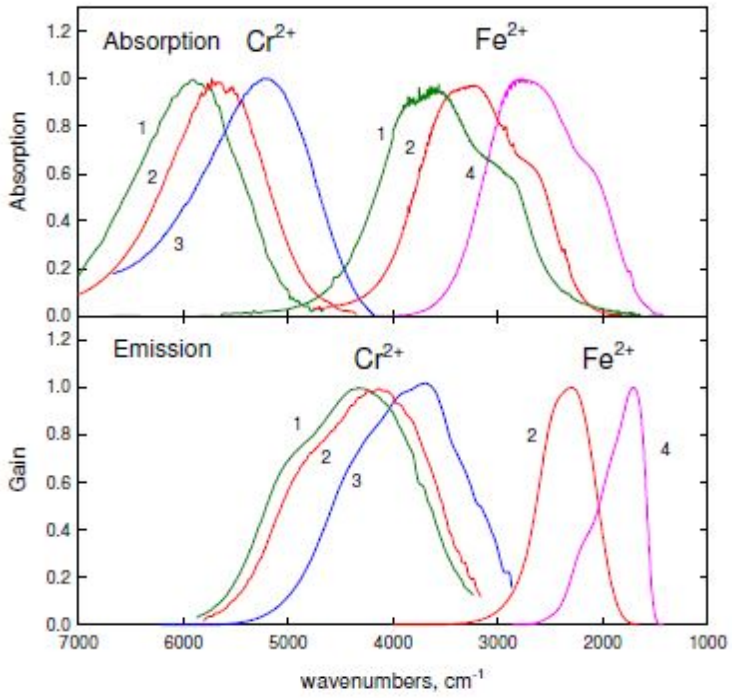

FIGURE 3.6: The absorption and emission spectra of chromium and iron doped ZnS (1), ZnSe (2), CdSe (3) and CdMnTe (4) crystals. The spectra of the iron doped crystals are shifted towards longer wavelengths compared to the crystals which are doped with chromium, due to the smaller crystal field splitting in iron. The ZnS compound has the largest crystal field splitting of the host materials included here, resulting in a shift towards smaller wavelengths compared to the other hosts. This is figure 1 in [24].

Chapter 4

Experimental

4.1 Physical vapor deposition, PVD

Physical vapor deposition (PVD) is a widely used method for thin film deposition. Among most common PVD processes are vacuum deposition (evaporation), sputter deposition, arc vapor deposition as well as ion plating. Among these, vacuum deposition including resistive heating is the most relevant process in this project, and will be presented below. The content of this section is based on chapter 1 and 6 in [43].

The films deposited by vacuum evaporation could be used as optical interference coatings, electrical conducting films, mirror coatings or decorative coatings just to mention some applications. As the name implies, the chamber in which the deposition takes place requires vacuum so that the evaporated material collides with no or a small number of gas molecules when it travels between the source and the substrate. A vacuum of 10^{-4} Torr or better is required for this to be the case, and usually the vacuum is in the range of 10^{-5} Torr to 10^{-9} Torr, depending on the desired quality of the film. The higher vacuum the less probability of a contaminated film [[43], chapt. 1].

The deposition rate is proportional to the vapor pressure, which means that in order to obtain a reasonable deposition rate, the vapor pressure of the material must be sufficiently high. The necessary value of vapor pressure is typically considered to be 10^{-2} Torr, and it gives a deposition rate that usually lies in the range of 10-100Å/s in PVD deposition. The equilibrium vapor pressure of a material is defined as the vapor pressure of the material in equilibrium, meaning that the number of atoms leaving the surface equals the number of atoms returning to the surface, with solid or liquid surface in a closed container. A subliming material is a material with vapor pressure of 10^{-2}

Torr above the solid, while an evaporating material is described as a material with vapor pressure of 10^{-2} Torr above a liquid melt. The fact that different elements have different vapor pressures at the same temperature can be utilized to purify alloys and mixtures by selective vaporization/condensation. When such purification is performed, the proportional relationship between vaporisation rate and the vapor pressure, also called Raoult's Law, is used.

In order to obtain an appropriate vapor pressure the material needs to be heated. This could be done by e-beams, inductive radio frequency heating, or resistive heating, where the latter method has been used in this project. Resistive heating involves heating the material by letting it be in contact with a hot surface, which is heated by passing a current through it. A common choice of such surfaces is a stranded wire, boat or a basket. The resistive heating is an appropriate method for heating below 1500°, while for higher temperatures it is common to use focused e-beams to warm up the material [[43], chapt. 6].

When the material vaporizes from the surface without colliding with other gas molecules in the space above the surface, the material is said to vaporize freely, and the free surface vaporation rate is given by equation (6.1) in [43], called the Hertz-Knudsen vaporation equation

$$\frac{dN}{dt} = C(2pmKT)^{1/2}(p* - p)sec^{-1} \tag{4.1}$$

where dN is the number of evaporating atoms per cm^2 of surface area, C is a constant that depends on the rotational degrees of freedom in the liquid and the vapor, $p*$ is the vapor pressure of the material at temperature T while p is the vapor pressure above the surface, k is Boltzmann's constant and m represents the mass of the vaporized species. The vapor rate is maximized when the vapor pressure above the surface is zero and there is only one rotational degree of freedom, i.e. $p = 0$ and $C = 0$. However, this is never the case in practice as $p > 0$ and $C \neq 0$ due to collisions in the vapor above the surface as well as contamination on the surface among other effects.

Another factor to be aware of when using PVD is how the evaporated material is distributed when it condenses on the substrate. Assuming no collisions within the gas, and low vaporization rates, the flux distribution could be described by the cosine distribution given by equation (6.2) in [43]:

$$\frac{dm}{dA} = \frac{E}{\pi r^2}\cos\varphi\cos\phi, \tag{4.2}$$

where dm/dA is the mass per unit area, E represents the total mass evaporated, r is the distance from the source to the substrate while φ and ϕ are the angles from the normal to the vaporizing surface and from a line from the source to a point on the substrate, respectively. The cosine distribution describing the thickness distribution of the condensed material on a planar substrate above a point source is shown in figure 4.1.

The basic function of the vacuum chamber associated with vacuum deposition is to

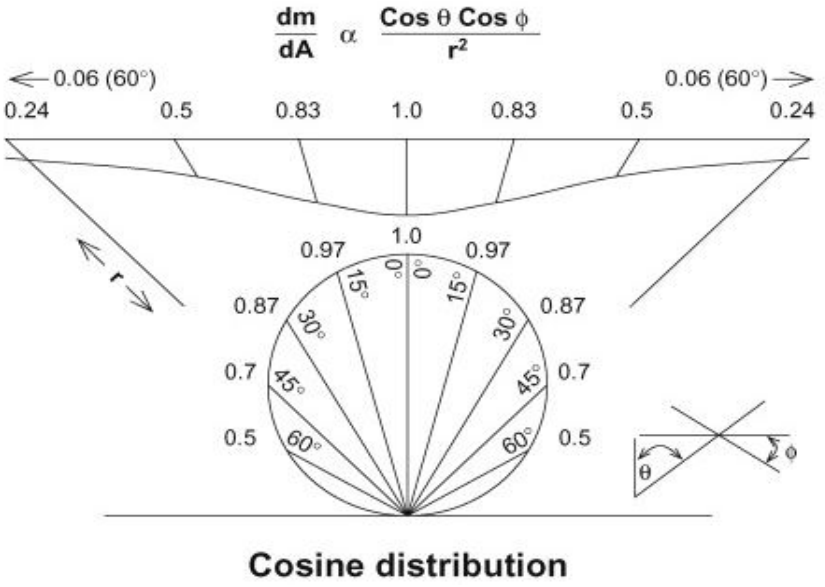

FIGURE 4.1: The distribution of atoms vaporized from a point source and the thickness distribution of the film formed on a planar surface above the source [[43], figure 6.4 p.200].

lower the probabilities of contamination of residual gases to a sufficient level. In order to decrease the contamination level further, one could let a cylindrical tube surround the volume between the source and the substrate, with the purpose that the molecules in the residual gas hopefully hit the cylinder rather than the film being deposited.

The source-substrate distance needs to be relatively large, so that the temperature of the substrate is sufficiently low for the evaporated material to condense when the substrate is reached, concerning the heat radiation from the evaporation source. One benefit of the large space within the chamber is that there are room for shutters to be installed above the source. The main function of the shutters is to prevent the vaporized material to reach the substrate when closed, in order to allow a uniform deposition rate to be established before the deposition takes place. It could also be convenient to define the deposition time by opening and closing the shutters.

It is usually important to monitor the deposition rate during PVD, as it highly affects the quality of the film. Other parameters like chamber pressure and temperature of source and substrate are also convenient to monitor, but the deposition rate is undoubtly the most important parameter. By knowing the deposition rate and the deposition time the mass and thickness of the film can also be determined, which are desired in most cases. The most typically used real-time deposition rate monitor for PVD processing is the quartz crystal deposition rate monitor (QCM). This single crystal quartz is a piezoelectric material, providing the properties of changing its volume when it is exposed to voltage. This voltage will cause the crystal to move, and this movement resonates with a frequency depending on the crystal orientation and the mass of the crystal. By utilizing the proportional relationship between the frequency change and mass added, the total mass of the deposited material is determined. Further, the deposition rate can be calculated calibrating the QCM with the density of the material.

Some of the advantages of the PVD processing is that it is relatively inexpensive compared to other coating techniques, and the deposition rate is tunable and could be easily monitored. Drawbacks of the same technique are however that it is difficult to obtain highly uniform films concerning the thickness.

The deposition was performed at Professor Ursula Gibson's lab with a CMK III vacuum deposition system.

4.2 Characterization

4.2.1 X-ray Diffraction, XRD

In XRD an X-ray beam is sent towards the sample with an incident angle θ, and gets scattered by the sample, before it reaches a detector positioned at an angle 2θ with respect to the incoming beam. As the detector is scanning over an appropriate range of angles, intensity peaks appear at some of these angles if the sample has a lattice configuration. The intensity peaks are a result of constructive interference between the incoming X-rays and the scattered X-rays, and the values of the angles where the intensity peaks appear, give valuable information about the structure of the sample. This information includes crystal symmetry and the value of the lattice constant. A sample consisting of a periodic crystal with interplanar spacing d, peaks of relatively high intensity being detected only at the angles θ would satisfy Braggs law[[44], p. 74]:

$$2d \sin\theta = n\lambda \tag{4.3}$$

where an integer number n of wavelengths of the X-rays λ, constitutes the path length difference between the incoming and diffracted X-ray that gives constructive interference. The d-spacing could further be related to the size of the unit cell of the sample, however, this relation varies for different crystal structures. With a, b and c being the length of the three axis forming the unit cell, this relation for a hexagonal unit cell is given by

$$\frac{1}{d^2} = \frac{4}{3}(\frac{h^2 + hk + k^2}{a^2}) + \frac{l}{c^2} \tag{4.4}$$

where h, k and l are the Miller indices of the crystal plane where the scattering of the X-ray beam occurs [[44], p. 75]. For the cubic structure $a = b = c$ and the equation simplifies to

$$\frac{1}{d^2} = \frac{h^2 + k^2 + l^2}{a^2}. \tag{4.5}$$

Based on the full-width half-maximum (FWHM) β of a peak occuring at the angle θ in the XRD spectrum, the average grain size τ in the material can be calculated by the Scherrer equation

$$\tau = \frac{0.9\lambda}{\beta \cos\theta}, \tag{4.6}$$

where λ is the X-ray wavelength, being $1.54\mathring{A}$ for a typical Cu K_α source [[44], p. 125].

In this project the XRD measurements were performed to examine the crystal structure of the films to see whether crystalline Fe:ZnS, if any, acts as wurtzite or Zincblende. In addition, XRD was used to study how the incorporation of iron affected the lattice structure, and to give an estimate of grain sizes.

The measurements were done by grazing incident X-ray diffraction (GIXRD), which involves a fixed small incident angle φ of the X-ray beam so that only a thin surface layer is exposed to X-rays [[45], p. 199]. A sketch of the path of the X-ray path is shown in figure 4.2. By using this method the contribution from the substrate is at a minimum, in order to detect the spectrum from the thin film only. The detector moves in the vertical plane perpendicular to the sample surface at an angle 2θ, as it detects the diffraction from the sample. The scans were performed in a 2θ range of 20°-70° with $\phi_{=}1°$ for 60 min.

The XRD measurements were performed with a D8 Advance DaVinci from Bruker at the Institute of Materials Science at NTNU. The software *diffrac.suite EVA* was used in the work of analysing the XRD spectra.

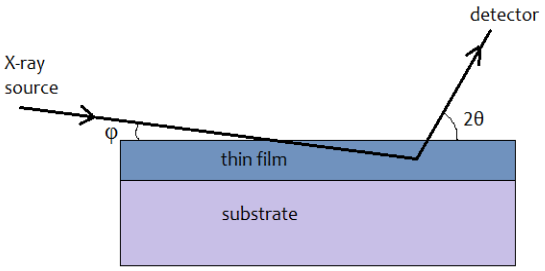

FIGURE 4.2: In a GIXRD scan the X-ray beam leaves the X-ray source and hist the sample at an small, fixed angle ϕ_i, so that only the thin film is exposed to the beam. The diffracted X-rays further hit a detector which moves in the vertical plane and records the X-rays at position 2θ.

4.2.2 Energy dispersive X-ray spectroscopy, EDS

In EDS an electron beam is sent towards the sample, with the purpose of exciting electrons to an outer shell. In the relaxation process where the excited electron jumps back to the inner shell from which it was emitted, a characteristic X-ray is released. The energy of the X-ray corresponds to the energy difference of the two shells, which gives rise to an X-ray line in an EDS spectrum. The EDS spectrum consists of several lines corresponding to different transitions. Since the energy difference between the two shells depends on the characteristic atomic structure of the element, the elemental composition of the sample can be measured [46].

EDS measurements were performed for all samples in a Hitachi TM3000 Tabletop microscope at NTNU nanolab.

4.2.3 Profilometer

A profilometer is used to measure the surface roughness, this could be done in a non-contact method with an optical profiler or a contact method where a stylus is used to mechanically contact the surface. The stylus profilometer is the relevant profiler for this project, and measurements are done by letting the stylus swipe across the surface. The stylus is in contact with the surface at all times and measures the height variations. These measurements are then converted into electrical signals, which are amplified and digitized. The result is a profile of the surface, that can be used for determination of the thickness of a thin film.

The profile given by the stylus profilometer is a convolution between the true surface

profile and the radius of the stylus. For this reason the lateral resolution of the surface is dependent on both the slopes of the profiled surface and the stylus radius, which means that in order to obtain a more accurate profile a small stylus radius must be used. Obviously, the surfaces to be profiled must be free of dust and particles using this contact method in order to obtain an acceptable profile.

The profiler used in this project was an alpha-step 100 profilometer with a stylus radius of 12 μm, and the measurements were performed in Prof. Ursula Gibsons lab at NTNU.

4.2.4 Spectrophotometry

The transmission and reflectance from a material can be measured by a spectrophotometer. A light beam which consists of wavelengths in the typical range from 200 nm to 800 nm is sent from a source towards the sample, and the intensity of the light being transmitted by the sample is recorded by a detector. In this way a transmission spectrum is given, and it shows the wavelength dependency of the intensity of the transmitted light. The relation between the intensity of the incident light from the source I_0 and the intensity of the transmitted light I at a depth x is given by

$$I(x) = I_0 e^{-\alpha x} \tag{4.7}$$

where α is the absorption coefficient [[10], p.88]. By letting d being the film thickness and using the definition of the transmission $T = \frac{I}{I_0}$, the absorption coefficient of the film can be calculated directly from equation 4.7:

$$\alpha = \frac{1}{d} \ln \frac{1}{T}. \tag{4.8}$$

By studying the absorption of the material the energy band gap of the sample can be determined in a Tauc plot [37].

Since the light has only three options when hitting the sample: it is either transmitted, absorbed or reflected, the reflection R of the film can be calculated, by using the relation

$$R + T + A = 1 \tag{4.9}$$

where the absorption A is given by the absorption coefficient and the film thickness, $A = \alpha \cdot d$ [[15], p.422].

The transmission measurements were performed by an Olis 14 UV/VIS/NIR spectrophotometer with an xenon lamp covering the ultra violet (UV) range from 185nm to 350nm,

and a tungsten halogen lamp being used for the visible (VIS) and near infrared (NIR) 350nm-2600nm region. All the samples with transparent substrates were measured in the 200nm -2600nm wavelength range. Additionally, the transmission and reflection of selected samples were measured with a fibre spectrophotometer consisting of an ocean optics ISS light source in the region 200nm-1100nm and detector AvaSpec 2048-USB2-UA from Avantes with range 200nm-1100nm. The software AvaSoft 8.0 from Avantes processed the data from the detector and formed the transmission spectra. Both instruments belong to Professor Ursula Gibson's lab at NTNU.

4.2.5 Fourier transform infrared spectroscopy FTIR

FTIR spectroscopy is a technique that can be used for studying the absorption of a material in the IR part of the spectrum, by measuring the transmittance of a material within the 2μm-20μm wavelength range. As the FTIR spectrum represents the molecular absorption and transmission, creating a molecular fingerprint of the sample, the technique can be used to identify unknown elements and compounds. Therefore, the FTIR spectroscopy is commonly used in the investigation of impurities or defects in materials [53],[54].

The measurements are performed by letting an IR-beam hit the sample, where the part of the radiation that is not being absorbed by the material reaches a detector. The detector records the intensities of the transmitted radiation at the different wavelengths in the IR, resulting in a spectrum. What distinguishes the FTIR spectroscopy from dispersive spectroscopy, is that all the frequencies in the selected range are measured simultaneously, making the FTIR measurements extremely fast. This gives the technique a huge advantage compared to the more time consuming dispersive spectroscopy where the frequencies are measured individually [55].

In order to measure all the frequencies simultaneously, the infrared beam hits a beamsplitter, letting 50% of the beam reflecting off of a mirror being at a fixed position, while the other 50% is reflected by a mirror which can be moved a short distance away from the beamsplitter. The beams then recombine at the beamsplitter after being reflected by their respective mirrors, creating an interference signal/pattern, in accordance with the basics of a Michelson interferometer. Due to the difference in path length of the two beams, the interference signal is dependent on the mirror position, and the resulting diagram showing this dependency is known as an interferogram. Every datapoint in the interferogram contains information about all frequencies from the source, and as the

name of the technique implies, the mathematical method called the Fourier transformation is applied in order to convert the interferogram to a spectrum showing intensitiy versus wavelength.

Since there needs to be a relative scale for the transmitted intensity of the film, a background spectrum from a bare substrate needs to be recorded before starting measuring the samples. Measurements of samples deposited on IR quartz substrate were performed in the 2.5μm-25μm range, by a Tensor 27 FTIR spectrophotometer, in professor Ursula Gibsons lab at NTNU.

4.2.6 X-ray Photoelectron Spectroscopy, XPS

In XPS a compositional analysis of the surface can be performed. A beam of X-rays, typically being Al K_α or Mg K_α X-rays with energy hv, is sent towards the sample and interacts with the atoms in the surface region by the photoelectric effect. This interaction causes an electron with binding energy E_b to be emitted, having a kinetic energy $E_k = hv - E_b - \phi_S$, with ϕ_S being the spectrometer work function. In addition to the photoelectrons, Auger electrons are also emitted due to the relaxation of the energetic ions after photoemission. The Auger electron is a secondary emitted electron, kicked out of its orbital by the energy that is released when an outer electron falls into an inner orbital vacancy, and it possesses a kinetic energy equal to the difference between the initial ion and the doubly-charged final ion. The kinetic energy of both the Auger electron and the photoelectron are recorded by a detector [48]. In order to limit the errors in the energy measurements, it is also important that the XPS is performed in ultra high vacuum so that the electrons avoid collisions with other molecules [[47], chapt. 3.2].

An XPS spectrum is generated from the detected data, and it shows the number of detected electrons plotted with respect to the binding energy of the respective electrons. This spectrum is characteristic for each compound, as the peaks reveal the compound's electron configuration. The number of counts at the characteristic peaks is directly related to the amount of the compound in the irradiated area, and in this way the element composition of the sample can be determined.

The X-rays irradiating the sample are typically Al K_α or Mg K_α X-rays with energy hv of 1486.6 eV and 1253.6 eV, respectively. These energies correspond to soft X-rays which have a relatively large penetration depth in the order of microns. The penetration depth

of the X-rays is however not the only limiting factor when it comes to the determination of the surface sensitivity. Because, even though the X-rays are being absorbed by an electron at a certain depth, only electrons that originates within tens of Angstroms below the surface can leave the surface without energy loss. These electrons appear as peaks in the XPS spectrum and are most useful, while electron that is emitted form a greater depth into the material undergo loss processes in their way towards the surface, and hence, they form the background in the spectrum [48].

Axis ultra DLD from Kratos was used to determine the composition of a selection of the deposited films. The measurements were performed at Institute of Electronics and Telecommunications at NTNU by the PhD candidate Mohammadreza Nematollahi.

4.2.7 Transmission electron microscopy, TEM

Transmission electron microscopy (TEM) is a micropscopy technique that is widely used to investigate the structure of different types of material. Due to the small de Broglie wavelengths of the electrons high resolution of 0.5Å can be obtained with an acceleration voltage of 200kV, which makes it possible to image the atom structure. It is however important that the thickness of specimen is sufficiently small, typically less than 80-100nm, for the electrons to be transmitted. In order to fulfill this requirement, a particular sample preparation is often necessary [[57] p.124].

The technique is based on focusing an electron beam produced by high acceleration voltage onto a thin sample by means of electromagnetic lenses [[57] p.124]. The electrons interact strongly with the sample, leading to creation of diffracted beams of electrons, energy-loss electrons, X-rays, back-scattered electrons as well as secondary electrons (STEM mode) [[56] p.60]. By adjusting the lens system, a certain electron type that is transmitted by the sample can be selected to reach a detector at the bottom of the microscope. In this way various imaging modes are obtained, extracting different information about the sample.

In the diffraction mode, the back focal plane of the object lense being placed right after the sample, is imaged. This back focal plane contains groupings of rays that have left the sample at the same angle, and it hence constitutes the diffraction pattern of the sample [[56] p.65]. From the diffraction pattern information about the crystallinity, crystal structure and size of the unit cell can be obtained.

By using an aperture, rays that give rise to a certain diffraction spot in a crystalline

sample can be selected. A bright field (BF) image is formed when the aperature is positioned such that only the transmitted (un-diffracted) electrons pass. This leads to bright areas in the image where the electrons pass nearly unimpeded by the sample, while the dark areas in the image represent the parts of the sample where only a small amount of the electrons are transmitted as they are scattered by the sample. The resulting BF image is comparable to everyday pictures of light passing through objects.

When the aperture is positioned to pass diffracted electrons only, on the other hand, a dark field (DF) image is obtained. Since the directly transmitted beam is blocked in this mode, the image appears black if there is no sample to scatter the electrons. By passing a diffraction spot corresponding to one particular *hkl*-value only, grains with this orientation are highlighted in the image, which could be a great advantage in the analysis of the specimen.

In addition to diffraction and spatial imaging, chemical information from electronic excitations can be obtained from the "analytical TEM modes" EDS, described in section 4.2.2 and electron energy-loss spectrometry (EELS). As the name implies, the latter technique involves measurements of the energy losses of the electrons after the high-energy electrons have traversed the sample. In the resulting EELS spectrum, the information on local chemistry and structure is obtained from features caused by core electron excitation in addition to plasmon excitations.

In this review, TEM measurements were performed on three samples of Fe:ZnS deposited directly on TEM grids. The purpose of the TEM measurements was to reveal the crystal structure and grain size in addition to studying uniformity and possible phase segregation of iron. The measurements were performed by Sintef researchers Per Eric Vullum and Ruben Bjørge using a JEM-ARM200F Atomic Resolution analytical Microscope at the Norwegian Centre for Transmission Electron Microscopy (NORTEM) facility at NTNU.

4.2.8 Ellipsometry

Ellipsometry is a non-destructive optical measurement technique enabling investigation of material properties of thin films. By measuring the change in the polarization of light being transmitted or reflected by the sample, optical constants like the dielectric functions and hence the complex refractive index can be determined, in addition to the band gap and the thickness of the film [[50] p. 1, [51], p.155].

In figure 4.3 a sketch of a general ellipsometer is shown. A collimated monochromatic

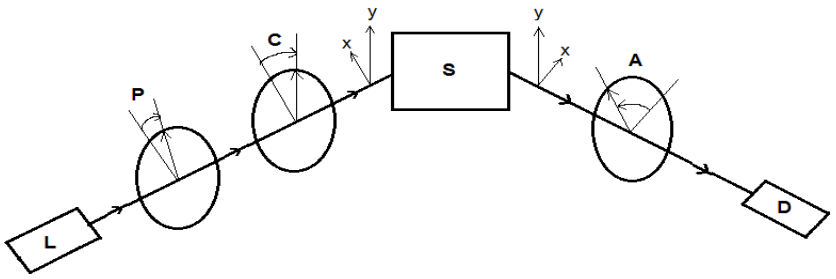

FIGURE 4.3: A PCSA ellipsometer arrangement with a polarizing section consisting of a linear polarizer P and a compensator (linear retarded) C, in addition to an analyzing section consisting of a linear analyser A. L and D represent the light source and photodetector, respectively. The figure is based on figure 3.3 in [51].

beam from a lightsource passes through a variable polarizer of known polarization before it hits the sample. As the light interacts with the film, its polarization is modified, and this modified polarization state is measured by a variable polarization analyzer before it reaches a photodetector [[51] p.154]. The change in polarization is the result of one or a combination of the processes reflection or refraction, transmission and scattering.

In this work, reflection ellipsometry is performed. The technique involves measurements of the amplitude component Ψ and the phase difference Δ between the incident and reflected light such that the complex reflection ratio ρ could be determined using the expression

$$\rho = \frac{r_p}{r_s} = \tan(\Psi)e^{i\Delta}, \tag{4.10}$$

where r_p and r_s are the Fresnel reflection coefficients of the p-polarized and the s-polarized light, respectively [[51] p. 274].

In order to determine the optical constants of the sample, a model analysis must be performed. A typical approach for extracting the complex dielectric function of a thin film material is based on the least-squares regression method, where the first step is to guess the values of the optical parameters as well as the film thickness. Second, the (Ψ, Δ) spectra corresponding to the initial guesses are calculated and compared with the experimental results. By using the least-squares regression algorithm, the first-guess parameter values are corrected such that the modeled parameter values are in closer agreement with the experimental values. This iteration is completed when the mean-square error function between the calculated and the measured (Ψ, Δ) spectra is minimized, and the optical parameters of the sample are assigned the values that corresponds to this modeled spectrum [[52], p. 96-97]. A more detailed description of

the modeling procedure is presented in section 5.3.2.4.

The measurements are performed using the commercial Spectroscopic Mueller Matrix Ellipsometer (S-MME) from the JA Woolam company (RC2). The samples were measured with a collimated beam in reflection, with incidence angle of 60°. A completeEase software provided by the producer of the ellipsometer was used in the modeling of the measurements. Measurements and modeling work was performed by the Postdoctoral candidate Zahra Ghadyani at the Department of Physics.

4.3 Experimental method

4.3.1 Substrates

The substrates used in the depositions consisted of 1cm × 1 cm fused silica transparent in the 190nm-2000nm wavelength region, 1cm × 1 cm <100>Si, in addition to circular IR quartz substrates of 1 cm diameter being transparent at wavelengths from 300nm to 3600nm. For the samples investigated with TEM, the films were deposited directly on a 300 mesh copper grid with Carbon Type A support film covered with a formvare film. By depositing directly on the grid, comprehensive sample preparation for TEM analysis was avoided.

The argument of choosing Si substrates, is that it is a readily available material with a smooth surface in addition of being conductive, which is preferred in a characterisation technique like XPS. The usage of the non-transparent Si substrate would also be convenient in reflectivity measurements. The transparency of fused silica and IR quartz makes the films deposited on substrates of these materials suitable for transmission measurements. The IR quartz enables absorption measurements in the IR region, which in turn could reveal information about the atomic structure of the films. In addition, the choice of using substrates of fused silica could also be supported by its flat and robust surface, which is an important quality in order to obtain a uniform film and to get reliable thickness measurements.

The cleaning of the substrates was done in three steps. These steps involved sonication in acetone in 15 minutes, followed by 15 minutes of sonication in isopropanol before it was dryed with N_2 gas and placed in the substrate holder inside the deposition chamber.

4.3.1.1 Substrate holders

As a part of the preparations for this project, a new substrate holder of aluminum was made. An image of the holder is shown in figure 4.4. In order to obtain a gradient in the Fe content of the films, enabling samples of different compositions to be made in one deposition, the substrate holder consists of six substrate positions next to each other in a line parallel to the source separation. The long shape of the holes allows to place substrates of different material in parallel. This ensures that an approximately equal film composition would be obtained for the samples in the same position, as the distance from the two sources would be nearly the same along the opening. In this way different characterization techniques that require different substrates could be related to a single film composition, and hence a more complete picure of the properties of the films can be achieved.

Flipping the substrate holders to the side, the edges of the holder become apparent,

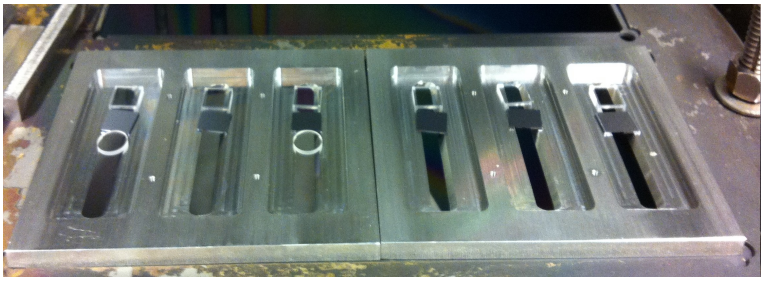

FIGURE 4.4: An image of the substrate holder used in the film depositions.

as sketched in figure 4.5. These edges are designed to be oblique, causing a smooth film edge along on one side of the surface, and a sharp film edge on the other side. Sharp film edges are very convenient considering the thickness determination, as it would be easier to read off a steep profile resulting from the alpha-step measurements.

4.3.2 Deposition

A CMK III vacuum deposition system was used for deposition of thin film samples, and the source material was evaporated by resistive heating. The base pressure after pumpdown varied from $2.8{\cdot}10^{-6}$ to $4.5{\cdot}10^{-6}$ torr, and this vacuum was achieved by using a mechanical pump and a diffusion pump, which was cooled with liquid N_2. During the depositions the pressured rised, and varied from $2.6{\cdot}10^{-5}$ to $5.1{\cdot}10^{-5}$ torr. A

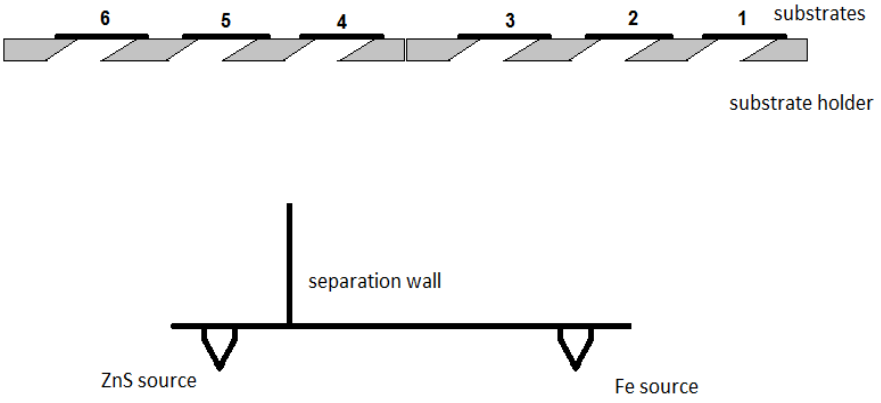

FIGURE 4.5: A sketch illustrating the edges of the substrate holders, and how the substrates are positioned relative to the material sources inside the deposition chamber. The sample positions being referred to in following chapters are labeled from 1 to 6.

sketch of the chamber used for deposition is shown in figure 4.6. A ZnS source of purity

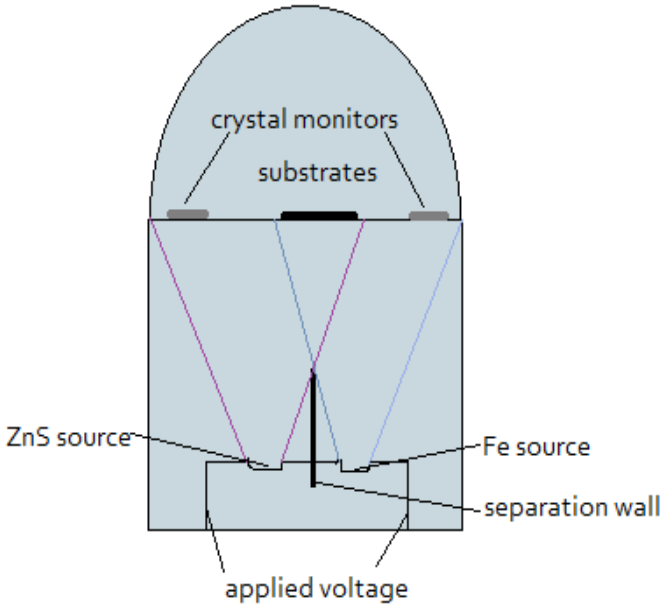

FIGURE 4.6: A schematic sketch of the setup in the deposition chamber shows the positions of the substrates and the crystal monitors on top and the two sources at the bottom of the chamber, separated by a partition wall. During deposition a voltage is applied to the source holders, and the evaporated material follows a path similar to the one indicated by the blue and purple lines.

99.99% and an iron source consisting of elemental Fe of purity 99.98% or the compound FeS of 99.9%purity were used for the depositions. ZnS was placed in a molybdenum

boat S8A:005TA while the iron source was put in an alumina coated tungsten basket, WBAO-1. The two sources were positioned at a distance 30 cm below the substrates, and separated by a thin molybdenum wall. One of the purposes of using a wall separating the two sources was to obtain a graded composition of the films with the substrates lined up parallell to the source separation, such that films of varying concentration of iron could be achieved in one deposition. A detailed description of the substrate holder and the samples' positions relative to the sources is found in section 4.3.1.1. The other reason for installing the partition wall, was to facilitate that the two crystal monitors only recorded the deposited material from one source each, which would make it easier to control the two deposition rates and thereby the composition of the samples.

The crystal monitors were placed at a fixed position for all depositions, at a level being approximately equidistant to the respective sources and the substrate holder. The level of which the crystal monitors were positioned, was below the shutter, enabling monitoring the evaporation from the moment the voltage was applied to the boat/basket such that stable rates could be obtained before opening the shutter and starting the deposition. The instantaneous deposition rates were observed carefully in a graphical presentation in Windaq© [58], and this monitoring was also useful in order to check if the crystal monitors were contaminated by the opposite source. By changing the deposition rate of one of the materials, one could see of it influenced the recorded deposition rate of the other material.

The rate of the ZnS was varying in the range 2.5Å/s to 8.5Å/s in different depositions, depending on the desired composition of the films. As an example, a voltage of approximately 43 volts was applied to achieve a 3.9Å/s rate, and overall the voltage needed to be increased continuously by small amounts in order to maintain the desired rate. The rate was decreasing as a result of increasing base pressure due to the chamber being heated. The rate of the iron source varied from 0.3Å/s to 1.3Å/s, and was in general chosen to be smaller compared to the rate of the ZnS source in accordance with the desired film composition. Applying a voltage of 68 V to the iron source resulted in a rate of 0.5Å/s.

In addition to the Fe:ZnS films, also films of pure ZnS, FeS and Fe were deposited. These were made for the preliminary measurements involving calculation of the expected film compositions as described in section 4.4, and in order to have a basis of comparison when performing the characterization measurements.

4.3.3 Transmission and reflection measurements

In order to perform transmission measurements, an Olis spectrophotometer was used to measure all transparent samples. Additionally, the transmission and reflection of selected samples were measured with a fibre spectrophotometer. These instruments are described in section 4.2.4.

In the measurements with Olis, the transmittance of the film was measured wavelength by wavelength. The source beam was alternating between passing through the sample in a sample chamber and an empty sample holder in a reference chamber for each wavelength. In this way, the reference intensity I_0 which corresponds to the intensity transmitted in air, was recorded almost simultaneously with the intensity transmitted by the sample. Before starting the actual measurements a baseline was recorded, by keeping the sample holders in both chambers empty. By consecutivly dividing the recorded transmitted intensity by the baseline, the transmission of the sample was calculated.

By using the fibre spectrophotometer, intensities at all wavelengths were measured simultaneously. In order to measure the transmission and reflection of the films with this spectrophotometer, a dark spectrum and a reference spectrum were recorded separately before starting data collection of the samples. During the dark spectrum measurements the light source was switched off and the sample holder was empty; this allowed removal of spurious values due to dark noise in the detector array. The light source was turned on when the reference spectrum was recorded. For the transmission measurements an empty sample holder was used as reference, while an aluminum mirror was used as reference for the reflection measurements. Subtracting the dark spectrum from the total intensity, and dividing by the reference spectrum gives the 100% line, and on this basis the transmission T is given by the expression

$$T = 100 \cdot \frac{sample_T - dark}{reference - dark}, \tag{4.11}$$

where $sample_T$ is the recorded intensity of the transmitted light through the sample. In similar way the expression of the reflectance R is calculated by the formula

$$R = 100 \cdot \frac{sample_R - dark}{reference - dark}, \tag{4.12}$$

here $sample_R$ is the recorded intensity of the light reflected by the sample.

The reflection given by equation (4.12), is in turn divided by the reflectivity spectrum of aluminum, given in figure 4.7 since an aluminum mirror was used as reference in the reflectivity measurements [49].

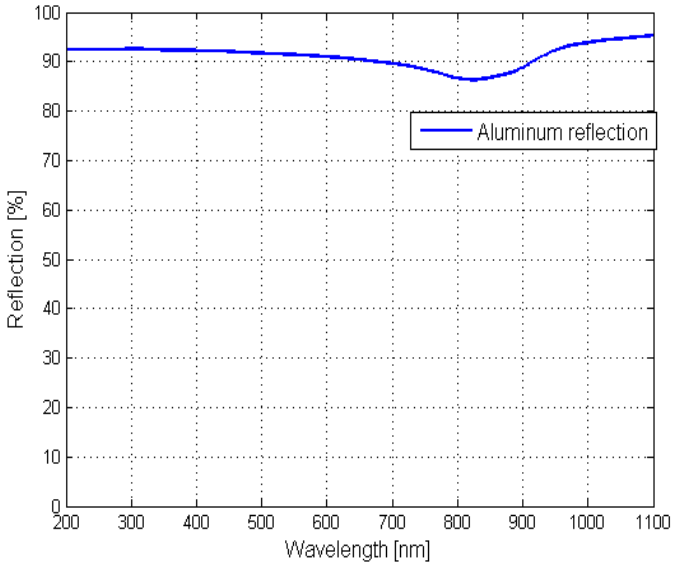

FIGURE 4.7: The reflectivity spectrum of aluminum, which was used as a reference in the reflection measurements of the films [49].

4.4 Preliminary measurements

In order to control the thickness and composition of the films during deposition, preliminary measurements were performed before starting the co-deposition runs of ZnS and Fe. In this process, the thicknesses recorded by the crystal monitor were compared against the actual film thicknesses, such that an expected Fe concentration could be calculated for the samples placed at the six different substrate positions inside the deposition chamber.

Two deposition runs were performed. Films of pure ZnS were deposited in the first run, while films of pure Fe was deposited in run number two. In both runs six films on silicon substrates were made, placing one substrate in each the six different positions in the substrate holder, as seen in figure 4.5 and 4.4 in section 4.3.1.1. The mean rate of the ZnS evaporation recorded by the respective crystal monitor was 5.5 Å/s while that of the Fe evaporation was 2.3 Å/s. After the deposition, the thicknesses of the films were measured with the alphastep profilometer and compared to the thickness recorded by the crystal monitor.

By dividing the measured film thicknesses of the samples with the thickness recorded by the crystal monitor, thickness correction factors were determined. These are presented in figure 4.4. As seen by the figure, the iron source seems to be closest to substrate position

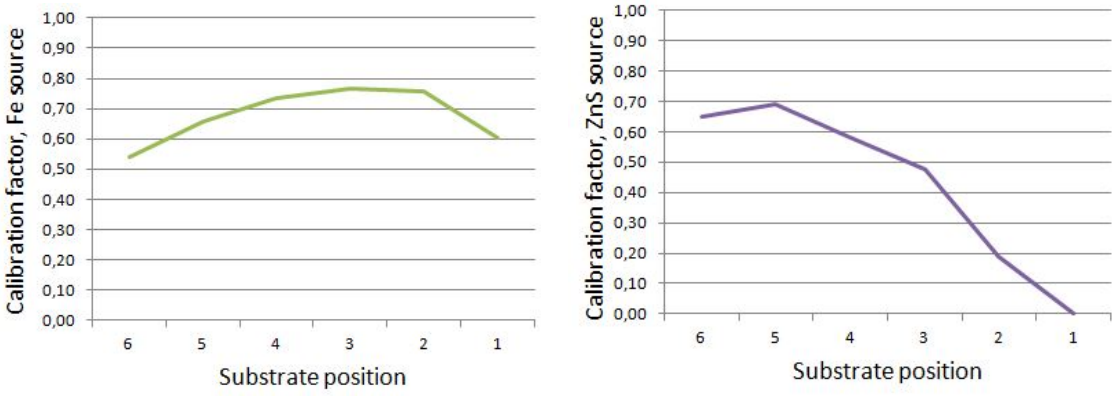

FIGURE 4.8: The thickness correction factors of the Fe source to the left and the ZnS source to the left. The factors corresponding to the two sources are obtained in two separate depositions where only one of the sources was used, by dividing the measured film thicknesses by the thickness recorded by the crystal monitor.

2 while the ZnS source seems to be closest to position 5, as the films at these positions had the largest thicknesses. This was confirmed by measuring the source-substrate distances inside the chamber. By studying the graphs one would get an estimate of how the evaporated material from each of the two sources would distribute on the different substrate positions. In addition, information about the actual sample thicknesses could be obtained, given the thickness recorded by the crystal monitor.

By using the thickness correction factors, the expected Fe concentrations of the films

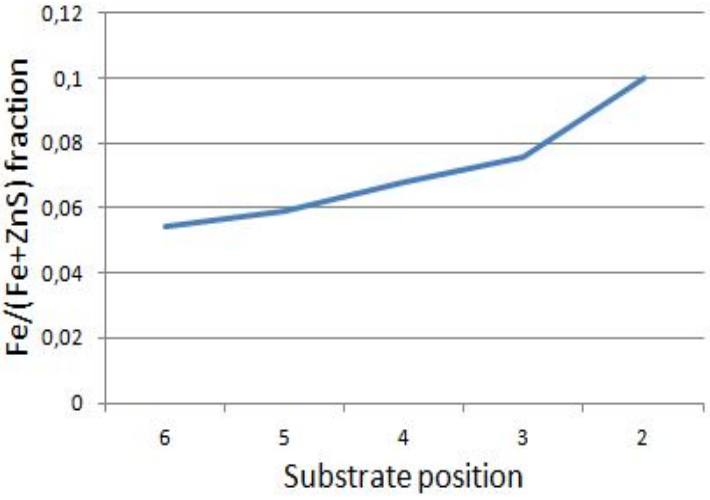

FIGURE 4.9: A graph showing the expected Fe concentration of the film distributed on the different substrate positions, with a maximum Fe/(Fe + ZnS) fraction of 0.1 based on the thickness of the pure films. In the deposition of ZnS, no material was reaching substrate position 1, and therefore data from this position is not included in the graph.

correponding to the different substrate positions were calculated. According to literature, Fe_x:$Zn_{1-x}S$ films with x in the 0.05-0.1 range would be interesting to investigate [6]. Inspired by this, the distribution of the Fe content of the films was calculated with a maximum Fe concentration of 10% based on the film thickness. The result from these calculations is presented i figure 4.9. As seen by the graph, in a deposition with a maximum Fe concentration of 10% at position 2, a graded film composition covering Fe concentrations in the desired 5-10% range would be expected. In the deposition of ZnS, no material was reaching substrate position 1, hence, estimated Fe content at this position is not included in figure 4.9.

Based on the calculations of expected film compositions with the given rates, the iron content in the films could be controlled during deposition. The experiences of the distribution of the Fe material were utilized in the depositions with the FeS iron source, which was seen to have a similar thickness distribution to that of the elemental Fe source.

Chapter 5

Results and discussion

5.1 Deposition rate and film thicknesses

An overview of the deposition rates and base pressure of the depositions are presented in table 5.1, while the film thicknesses and composition of the films are shown in table 5.2. A copy of theses tables is given in appendix A, and it might be convenient to remove this appendix and to have a look at it while reading through the results.

TABLE 5.1: The deposition rates of the Fe/FeS source and ZnS source, in addition to the base pressure before- and during the different deposition runs.

Deposition run	Base pressure after pump down [torr]	Base pressure during deposition [torr]	ZnS rate [Å/s]	Fe rate [Å/s]	FeS rate [Å/s]
A	3.3e-6	3.1e-5	8.5	0.4	-
B	2.8e-6	2.6e-5	8.2	1.3	-
C	3.6e-6	2.6e-5	4.1	0.5	-
D	3.9e-6	2.6e-5	7.9	-	-
E	4.1e-6	2.7e-5	3.9	-	0.5
F	4.5e-6	2.5e-5	-	-	0.5
G	4.2e-6	2.8e-5	5.6	-	0.6
H	3.3e-6	5.1e-5	2.5	-	0.6
I	4.0e-6	2.8e-5	4.4	-	0.3

The samples are labeled such that information about the composition and deposition conditions are provided in the name. The deposition run is denoted by the letters A-I, while the iron source used in the deposition are represented by the letters F, FA or FES,

TABLE 5.2: The thickness and composition of the films. *The concentration is considered to be questionable due to a S/(Fe+Zn) ratio deviating more than 0,3 from unity.

Sample	Substrate	Thicknesses (+/- 50) [Å]	Fe/(Fe+Zn+S) [%]	S/(Fe+Zn) [%]
AF1Si22.1	Silicon	697	22,1*	0,46*
AF2Si4.2	Silicon	1613	4,2	0,75
AF2Quv4.3	Fused silica uv	1784	4,3	0,95
AFA2Quv4.3	Fused silica uv	1784	4,3*	0,67*
AF3Si3.0	Silicon	2381	3,0	0,75
AF3Quv3.1	Fused silica uv	2555	3,1	0,90
AFA3Quv3.1	Fused silica uv	2555	3,1*	0,67*
AF4Si2.3	Silicon	2873	2,3	0,78
AF4Quv2.4	Fused silica uv	3063	2,4	0,99
AFA4Quv2.4	Fused silica uv	3063	2,4*	0,67*
AF5Si1.9	Silicon	3156	1,9	0,77
AF5Quv1.8	Fused silica uv	3375	1,8	1,01
AFA5Quv1.8	Fused silica uv	3375	1,8*	0,68*
AF6Si1.5	Silicon	3188	1,5	0,78
AF6Quv1.5	Fused silica uv	3387	1,5	0,95
AFA6Quv1.5	Fused silica uv	3387	1,5*	0,68*
AF6Qir1.4	Quartz ir	3117	1,4	1,19
BF1Si17.4	Silicon	623	17,4	0,50
BF1Quv11.8	Fused silica uv	605	11,8	1,02
BFA1Quv11.8	Fused silica uv	605	11,8	0,95
BF2Si13.5	Silicon	1167	13,5	0,73
BF2Quv12.0	Fused silica uv	1258	12,0	1,09
BFA2Quv12.0	Fused silica uv	1258	12,0	1,07
BF3Si11.0	Silicon	1557	11,0	0,73
BF3Quv11.1	Fused silica uv	1667	11,1*	1,42*
BFA3Quv11.1	Fused silica uv	1667	11,1	0,77
BF4Si8.3	Silicon	2017	8,3	0,72
BF4Quv8.2	Fused silica uv	2169	8,2*	1,45*
BFA4Quv8.2	Fused silica uv	2169	8,2	0,73
BF4Qir8.4	Quartz ir	1552	8,4	0,96
BF5Si6.5	Silicon	1828	6,5	0,74
BF5Quv6.8	Fused silica uv	2133	6,8	1,08
BFA5Quv6.8	Fused silica uv	2133	6,8	0,70
BF6Si4.7	Silicon	2145	4,7	0,75
BF6Quv5.0	Fused silica uv	2156	5,0	0,98
BFA6Quv5.0	Fused silica uv	2156	5,0	0,71
BF6Qir4.8	Quartz ir	2484	4,8*	1,59*
CF3Grid12.2	TEM grid	440	12,2*	0,63*
CF5Grid6.5	TEM grid	733	6,5	0,73
DZnS5Si	Silicon	1736	0,0	0,78
DZnS5Quv	Fused silica uv	1956	0,0	1,05
DZnS6Si	Silicon	1731	0,0	0,78

Sample	Substrate	Thicknesses (+/- 50) [Å]	Fe/(Fe+Zn+S) [%]	S/(Fe+Zn) [%]
DZnS6Quv	Fused silica uv	1996	0,0	1,30
DZnS6Qir	Quartz ir	1717	0,0	1,69*
EFES1Si8.3	Silicon	1601	8,3	0,97
EFES1Quv7.7	Fused silica uv	1809	7,7	0,82
EFES2Si7.2	Silicon	2139	7,2	0,91
EFES2Quv7.4	Fused silica uv	2320	7,4	0,84
EFES2Qir7.0	Quartz ir	1988	7,0	0,70
EFES3Si1.9	Silicon	2316	1,9	0,79
EFES3Quv1.8	Fused silica uv	2297	1,8*	0,62*
EFES3Qir1.8	Quartz ir	2031	1,8*	0,61*
FPFES2Si	Silicon	308	-	-
FPFES2Quv	Fused silica uv	367	-	-
FPFES3Si	Silicon	367	-	-
FPFES3Quv	Fused silica uv	385	-	-
GFES1Si3.5	Silicon	1650	3,5	1,05
GFES1Quv3.3	Fused silica uv	1643	3,3	0,84
GFES2Si1.5	Silicon	2164	1,5	0,85
GFES2Quv1.5	Fused silica uv	2222	1,5	0,76
GFES3Si1.0	Silicon	2553	1,0	0,82
GFES3Quv1.1	Fused silica uv	2672	1,1	0,76
HFES2Quv5.1	Fused silica uv	1816	5,1*	1,57*
IFES3Grid3.0	TEM grid	200	3,0	1,22
EKMBESi1.7	Silicon	23750	1,7	0,85
EKMBESi1.9	Silicon	24500	1,9	0,84
EKMBE$CaF_2$1.7	CaF_2	25050	1,7	0,85
EKMBE$Al_2O_3$1.6	Sapphire	22250	1,6	0,85
EKMBE$Al_2O_3$7.1	Sapphire	4867	7,1	0,72
EKMBESi2.1	Silicon	4900	7,5	0,74
EKMBEQuv7.8	Fused silica uv	4850	7,8	0,73
EKMBEQir7.0	Quartz ir	5075	7,0	0,74
EKMBE$CaF_2$2.1	CaF_2	34750	2,1*	1,31*
EKMBE$Al_2O_3$1.9	Sapphire	36625	1,9*	2,29*
EKMBEPZnSAl_2O_3	Sapphire	1400	0,0	-
EKMBE$CaF_2$4.0	CaF_2	4400	4,0	-

where F denotes pure Fe, FA indicates that a film doped with Fe from the elemental Fe source is annealed, and FES indicates that FeS is used as the Fe source. The subsequent number corresponds to the substrate position in the deposition chamber, where a smaller number indicates a shorter distance to the Fe source. A detailed description of the substrate holder and the geometry of the deposition chamber is given in section 4.3.1.1. Next to the number of the substrate position, information about the substrate is given, where Quv denotes fused silica (being transparent for wavelengths up to 2400 nm), Qir refers to IR quartz (being transparent for wavelengths up to 5000 nm), Si is used for a silicon substrate, while "Grid" indicates the substrate consists of a TEM grid.

Finally, the last digits of the name represent the Fe concentration of the film. As an example, sample BF5Quv6.8 is made in deposition run B where the elemental Fe source is applied, the film is deposited on fused silica transparent in the UV region, it is placed at position 5 in the substrate holder, and it contains 6.8 %Fe. Sample BFA5Quv6.8 is the same sample, but this film has additionally been exposed for annealing.

Films consisting of pure ZnS and pure FeS are given names of the form DZnS6Quv and FPFES2Quv, respectively, while the samples made by Eric Karhu in molecular beam deposition are labeled EKMBE followed by the substrate and Fe concentration.

5.1.1 Deposition rates

During the deposition, the deposition rates of the material from the two sources were recorded by two crystal monitors and could be watched graphically on a PC screen. This made it easier to adjust the voltage supply such that stable rates could be obtained.

The deposition rates of ZnS and Fe in deposition run A are given in figure 5.1. The rates

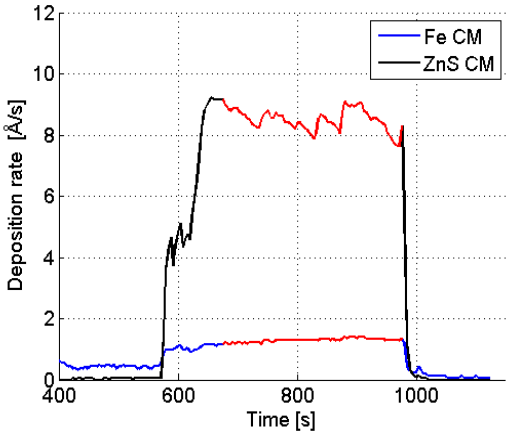

FIGURE 5.1: The deposition rates of the Fe source and the ZnS source during deposition run A, shown with blue and black colour, respectively. An increase in the rate of Fe is observed when the evaporation of ZnS starts at x= 572s. This indicates that the crystal monitoring the Fe evaporation also detects some of the deposited ZnS material. The actual deposition took place in the x-range from 680s to 980s, and the rates in this interval are marked with red colour.

are recorded before, during and after the actual deposition, which took place in the time range 680s-980s. As seen from the figure, the signal at the Fe crystal monitor increases when the ZnS starts to evaporate indicating that the Fe crystal monitor is cross contaminated with ZnS from the opposite source. This overspray is not unexpected as ZnS is notorious for re-evaporation and non line of sight deposition. Based on the recorded

rates in deposition run A, calculations show that 11% of the evaporated ZnS is reaching the Fe crystal monitor. Similar cross contaminations of ZnS also occured in the other deposition runs, and in the resulting values of rates given in table 5.1 correction factors are included.

The Fe/FeS source on the other hand, is observed to have a more directional deposition, since this material gives no signal on the ZnS monitor. This line of sight deposition of Fe/FeS is confirmed looking at the EDS concentration measurements, revealing a significant difference in Fe composition among the films placed at the different sample positions in the deposition chamber. A more detailed discussion of the EDS measurements is found in section 5.2.3.

The rates applied for the depositions, given in figure 5.1, were chosen in accordance with the results of the preliminary measurements given in section 4.4.

5.1.2 Thickness measurements

5.1.2.1 Alphastep profilometer

An overview of the film thicknesses resulting from the measurements performed by the alphastep profilometer are shown in table 5.2. The measurements show a significant variation in thickness of the samples made during the same deposition run. This speaks to a variation in composition of the films as well, just as desired with the chosen set-up in the deposition chamber. The thickness variations within a single sample on the other hand, are very small, typically around 1-2%. In the samples where larger variations of 5-11% are present, the thickness variation becomes evident in terms of colour variation, observed by looking at the samples with the naked eye.

The thickness profile of sample BF5Quv6.8 is shown in figure 5.2, and it reveals a sharp

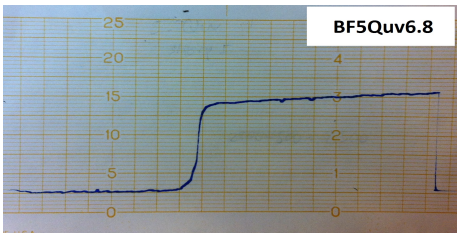

FIGURE 5.2: The profile of sample BF5Quv6.8 revealing a thickness of 2130 Å after applying a correction factor.

film edge of thickness 2130 Å after applying a correction factor of the profilometer. A sharp film edge was achieved for all the samples, and this was shown to be convenient in order to obtain a thickness value with an accuracy of a few percent. The instrument itself has an accuracy of ± 50Å.

5.2 Structural and compositional characterisation

In the following section the results following from the structural characterization of the films involving XRD and TEM are presented, in addition to information about the film composition resulting from EDS and XPS measurements. By studying the structure and concentrations of the films, a more complete picture of the optical features of the films discussed in section 5.3 is obtained.

5.2.1 X-ray Diffraction, XRD

The XRD spectra of sample EKMBESi1.9, DZnS6Quv, BF5Quv6.8, EFES2Quv7.4, BF2Quv12.0 and FPFES2Quv resulting from GIDXRD scans are shown in figure 5.3. Additionally, the spectrum of the FeS powder used as iron source obtained from conventional XRD is presented in the same figure. The rather broad peaks, whose values of the full-width half maximum are 0.3-1 degree for the ZnS and the Fe:ZnS films, indicate that the films consist of small grains. Estimations based on the Scherrer equation 4.6 found in section 4.2.1 suggest grain sizes of 30nm, 9nm, 21nm, 20nm, 21nm in sample EKMBESi1.9, DZnS6Quv, BF5Quv6.8, EFES2Quv7.4, BF2Quv12.0, respectively. These values are larger than the grain sizes of 5-10nm resulting from TEM measurements shown in section 5.2.2, and this could be explained by the fact that the grain sizes usually increase during deposition of thin films.

The most prominent peak of sample DZnS6Quv consisting of pure ZnS at 28.64° coincides with both the [111] reflection from cubic sphalerite and the [002] reflection from the hexagonal wurtzite structure. Small, additional peaks appearing at approximately 47° and 56° are also indexing both the cubic and hexagonal forms of ZnS, making it difficult to give a conclusive answer of the film structure. However, a hexagonal phase could be concluded after investigating films with TEM, as seen in section 5.2.2.

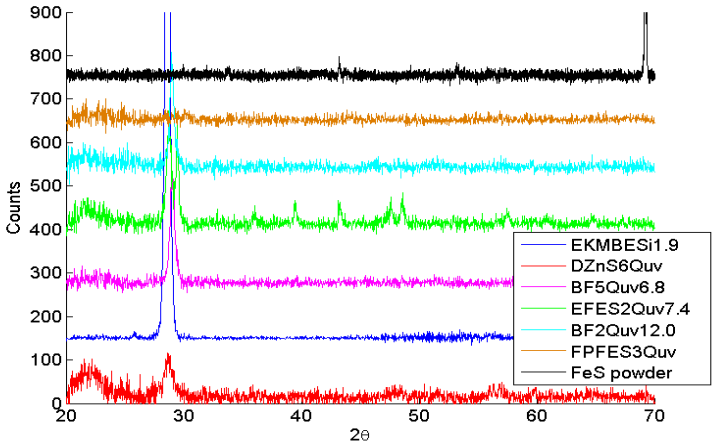

FIGURE 5.3: The XRD spectra of Fe:ZnS with different doping levels, in addition to the spectra of the pure ZnS and FeS. The most prominent peak of pure ZnS at 28.6° coincides with both the [111] cubic and the [002] hexagonal reflections, and is shifted to 29° for sample BF5Quv6.8 and BF2Quv12.0. The spectrum of sample EFES2Quv7.4 contains narrower and more numerous peaks. Characteristic lines of the cubic and hexagonal phase are observed for this sample, as well a peak corresponding to the [102] reflection of FeS occuring at 43.19°. The spectra have different scaling.

5.2.1.1 Films deposited with Fe as the iron source

For the BF5Quv6.8 and the BF2Quv12.0 films doped with 6.8% and 12.0% Fe from the elemental Fe source, respectively, the main peak is observed to be shifted to the higher angle of 29°, compared to 28.64° for the pure ZnS sample. A shift in the XRD spectrum for higher Fe doping levels in ZnS was also observed by Feng et al [8], but in the opposite direction. However, their films were crystalline, growing on Al_2O_3 at high temperatures, and may suffer from some substrate-induced strain.

5.2.1.2 Films deposited with FeS as the iron source

The XRD spectrum of the mixed film of FeS and ZnS in sample EFES2Quv7.4 stand out from the other spectra in figure 5.3 deposited from Fe and ZnS, as it contains narrower and more numerous peaks. This could be an indication of some phase separation or clusters of Fe, however, TEM measurements could neither confirm or disprove this possible appearance. The peak at 43.19° corresponds to the [102] reflection of FeS, and a similar peak is also observed in the XRD spectrum of the FeS powder. At 28.73°, 47.60° and 56.54° peaks indexing both the cubic and the hexagonal phase of ZnS appear. For a hexagonal phase the peaks would correspond to the [002], [110] and [112] reflections, respectively, and the same peaks also coincide with the [111], [220] and [311]

lines characteristic for the cubic ZnS structure. However, the peaks at 39.47° and 57.50°, corresponding to the [102] and [201] planes of wurtzite respectively, do not coincide with any reflections from the cubic phase, giving evidence for a hexagonal wurtzite structure. Common for all the peaks that appear to coincide with the cubic and hexagonal phase of ZnS, is a 0.04°-0.23° shift towards higher angles, than that of the pure ZnS. This behaviour of the mixed FeS and ZnS films is similar to that of the films deposited from the elemental Fe source and implies a small decrease in the lattice constant when Fe is introduced to the ZnS film, which could indicate Fe binding to S by substituting Zn.

The pure FeS film in sample FPFES3Quv is not seen to contain any significant peaks, except a weak [100] reflection at 30.14°, indicating the film is mostly amorphous. In the spectum of FeS in powder form, used as source material in several film depositions including that of sample EFES2Quv7.4, the peaks appearing at 29.99°, 33.67°, 43.19°, 53.14° and 56.15° correspond to the [100], [101], [102], [110] and [103] reflections of hexagonal FeS. The strong peak at 69.22° is from the silicon substrate.

As a summary of the results from the XRD measurements, a dependency on the iron source can not be seen regarding the grain sizes and the shift towards higher angles observed for the iron doped films. Studying the XRD spectra of the pure ZnS film and films deposited from ZnS and elemental Fe, could not give any conclusive answer of the film structure. The spectrum of the mixed FeS and ZnS film, on the other hand, containing more numerous peaks, gives evidence for a hexagonal structure.

5.2.2 Transmission electron microscopy, TEM

TEM measurements confirm the results from XRD, showing that the films are comprised of small grains, seen in figure 5.4 and 5.5. While XRD could not give an conclusive answer on the crystal structure of the Fe:ZnS films, TEM investigation of sample CF3Grid12.2, CF5Grid6.5 and IFES3Grid3.0 revealed the presence of a hexagonal structure. These samples were special made for TEM measurements, depositied directly on TEM-grids, with thicknesses of approximately 40nm, 70nm, and 20nm, respectively, and respective Fe concentrations of 12.2%, 6.5% and 3.0%. Sample CF5Grid6.5 and CF3Grid12.2 are made from Fe and ZnS sources, while sample IFES3Grid3.0 is deposited with FeS and ZnS sources. Since TEM grids are used, the electrons hit the surface of the as-deposited film with a traveling path being parallell to the growth direction, such that information about the growth process would be difficult to obtain. For studies of the growth process of the films a cross-sectional sample would be preferred. The TEM results presented in the following sections reveal a difference in grain size between the films deposited with

different iron sources. This could reflect differences in the results of the optical analysis of the films made of Fe and FeS as the iron source, seen in section 5.3.1 and 5.3.3.

5.2.2.1 Films deposited with Fe as the iron source

The TEM results show that sample CF5Grid6.5 and CF3Grid12.2 made of Fe and ZnS seem to be quite uniform with regard to the iron distribution, with no phase segregation or iron clusters observed. This is in agreement with the results from the imaging in the EDS measurements performed with the table top SEM. The variation in thickness is low. However, energy electron loss spectroscopy (EELS) revealed some porosity which seems to be associated with oxygen in certain areas of the film. The high resolution TEM images reveal small crystal grains in the samples, the grain size is typically 8-10 nm. From the bright field image of sample CF5Grid6.5 given in figure 5.4, grains of these typical sizes are observed, with the grain indicated in the image having a diameter of approximately 11 nm. As grain sizes usually increase during deposition of thin films, the average grain size on the grid was smaller than that observed by XRD.

The presence of nanocrystalline grains in the samples is confirmed by looking at the

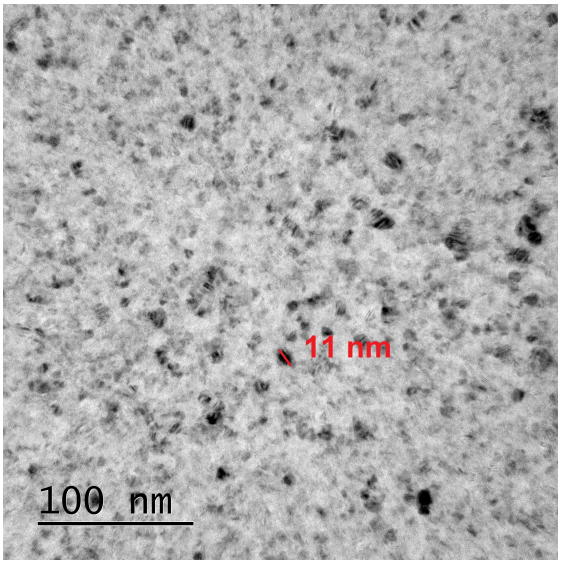

FIGURE 5.4: A bright field image of sample CF5Grid6.5 seems to reveal a uniform film, with overall crystal grain sizes of 10 nm. The grain indicated in the image, has a diameter of approximately 11 nm.

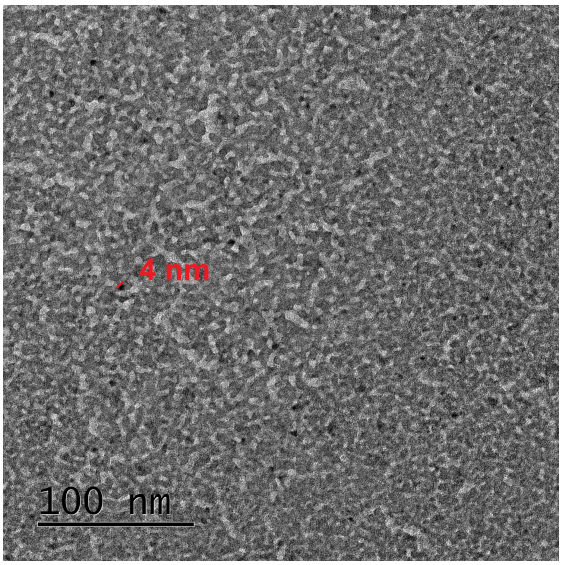

FIGURE 5.5: A bright field image of sample IFES3Grid3.0, deposited from FeS and ZnS sources reveals a film of nonuniform thickness, and with overall grain sizes of 5 nm. The grain indicated in the image, has a diameter of approximately 4 nm.

diffraction images of the films. The diffraction image of sample CF3Grid12.2, which is observed to be similar to that of sample CF5Grid6.5, is presented in figure 5.6. The circular diffraction pattern observed in the image arises from electrons being scattered by crystal grains with many orientations, indicating a polycrystalline film.

Each ring is assigned to a lattice plane in the sample, determined by the radius of

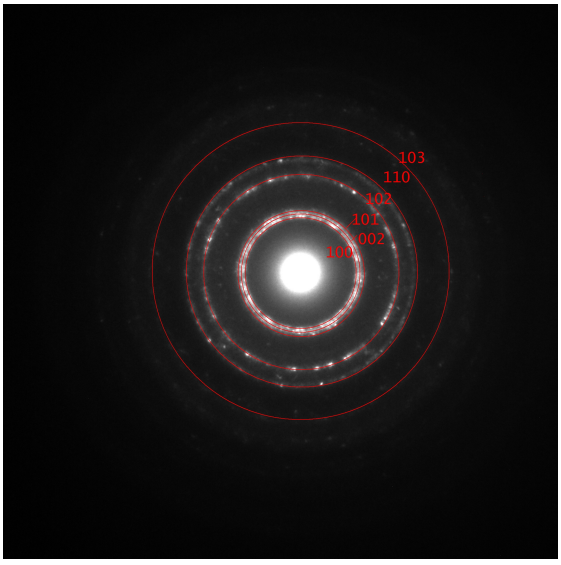

FIGURE 5.6: A diffraction image of sample CF3Grid12.2. The six inner rings with increasing radius correspond to the lattice planes [100], [002], [101], [102], [110] and [103] of wurtzite, respectively.

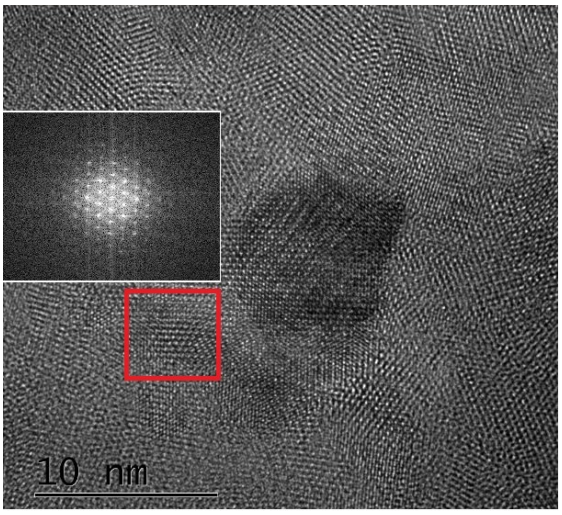

FIGURE 5.7: The figure shows a bright field image of sample CF3Grid12.2. The fast fourier transform of the grain enclosed by the red square, to the left in the figure, shows a hexagonal pattern, revealing the wurtzite structure of the single crystal grain.

the circle. Hence, by looking at the radius of the diffraction rings, the crystalline structure of the film could be determined from the diffraction image of sample CF3Grid12.2 in figure 5.6. It is observed that the diameters of the three inner rings are almost the same, corresponding to the three lattice planes [100], [002] and [101] of the wurtzite structure, respectively. With increasing radius, rings corresponding to the [102], [110], [103] and [200] planes are observed. These are all planes in the wurtzite structure. Based on the fact that all the rings observed can be assigned to lattice planes of the wurtzite structure, it can be concluded that the CF5Grid6.5 and CF3Grid12.2 films contain this hexagonal structure.

The hexagonal structure is also observed in a single crystal grain by taking the fast fourier transform (FFT) of the image of the grain. A bright field image of sample CF3Grid12.2 in addition to the FFT of a particular grain in this image are presented in figure 5.7. The FFT of the image contains similar information as a diffraction image,

and the dotted pattern in a hexagonal formation is evident. Whether the hexagonal structure is maintained throughout the film thickness cannot be stated unequivocally, but the TEM grid is about 25% of the thickness of a typical sample and is likely to be representative of the full thickness.

5.2.2.2 Films deposited with FeS as the iron source

As opposed to the samples made of Fe and ZnS, the TEM images of sample IFES3Grid3.0 deposited with the FeS iron source reveal a nonuniformity in the film thickness. Additionally, this sample is observed to consist of smaller crystal grains compared to the grain sizes in sample CF5Grid6.5 and CF3Grid12.2. Similar to the CF5Grid6.5 and CF3Grid12.2 films, no phase segregation or clusters of Fe are seen to occur in sample IFES3Grid3.0, and diffraction images reveal the same hexagonal structure in the IFES3Grid3.0 film.

Differences between the films deposited with Fe and FeS as iron source become ap-

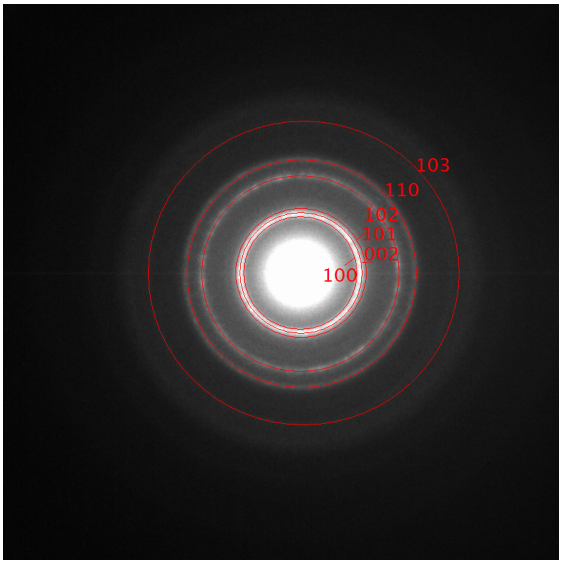

FIGURE 5.8: A diffraction image of sample IFESGrid3.0. The six inner rings with increasing radius correspond to the lattice planes [100], [002], [101], [102], [110] and [103] of wurtzite, respectively. Similar reflections are seen in the diffraction images of sample CF5Grid6.5 and CF3Grid12.2

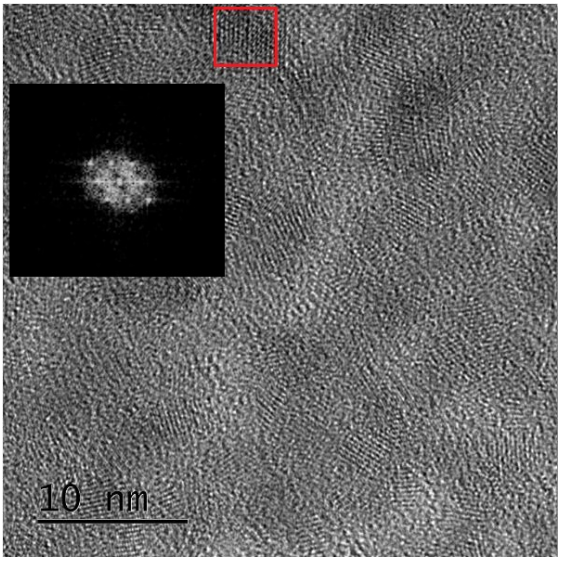

FIGURE 5.9: The figure shows a bright field image of sample IFES-Grid3.0. The fast fourier transform of the grain enclosed by the red square shows a hexagonal pattern, revealing the wurtzite structure in the single crystal grain.

parent by looking at the bright field images of sample CF5Grid6.5 and IFES3Grid3.0 given by figure 5.4 and 5.5, respectively, where smaller grains are observed in sample IFES3Grid3.0, compared to sample CF5Grid6.5. Overall grain sizes in sample

IFES3Grid3.0 are observed to be 3-5 nm, and the grain indicated in bright field image of this sample in figure 5.5 has a diameter of approximately 4 nm. In sample CF5Grid6.5 the typical grain size is 8-10 nm.

The strong contrast seen in the bright field image of sample IFES3Grid3.0 in figure 5.5 is caused by a thickness variation of the film and becomes especially evident due to the small film thickness of 20 nm. In addition of showing a nonuniformity in the thickness, the bright field image of sample IFES3Grid3.0 in figure 5.5 does not seem to reveal any phase segregation nor Fe clusters in the film. This was confirmed by EDS measurements performed in scanning transmission electron microscopy (STEM) mode.

The diffraction image of sample IFES3Grid3.0 in figure 5.8 is observed to contain the same circular pattern as the diffraction images of sample CF5Grid6.5 and CF3Grid12.2. The fact that the diameters of the rings are observed to be equal for all three samples investigated by TEM, implies that the films have the same hexagonal structure independent of the iron source. Similar to sample CF5Grid6.5 and CF3Grid12.2, the hexagonal structure of sample IFES3Grid3.0 is confirmed by taking the FFT on a single grain, showing a hexagonal pattern, found in figure 5.9.

The large amount of amorphous material that is observed surrounding the grains correlates with the XRD results showing films of low crystallinity.

5.2.3 Energy Dispersive X-ray Spectroscopy, EDS

EDS measurements were performed on all samples in order to determine the elemental composition of the films, and the resulting concentrations in the samples are given in the overview in table 5.2. The measurements reveal an Fe distribution similar to what was expected, according to the preliminary measurements in section 4.4, confirming the case of a desired gradient composition of the films made in one single deposition.

Peaks from the expected elements Zn, S, Fe, Si, C and O are observed in the EDS spectra of all the Fe:ZnS films on silicon, fused silica and quartz substrates, including sample AF5Quv1.8, whose EDS spectrum is shown in figure 5.10. A prominent Si peak reflects a significant signal from the substrate. A large contribution from the substrate is observed for all samples as a consequence of the small film thicknesses. The only exception is four films deposited under UHV conditions having a thickness 10 times larger than the other samples.

As well as oxygen present in the IR quartz and fused silica substrates, O and C signals are likely to come from the deposition chamber. This raises the possibility that some oxygen has been substituting sulfur forming Fe:ZnS_xO_{1-x}, rather than the desired Fe:ZnS. This could explain the overall films being lower of S than (Zn+Fe). A presence of oxygen was also shown in films investigated by TEM, found in section 5.2.2.

In figure 5.11 a SEM image of sample BF5Quv6.8 is presented, and it shows a cluster

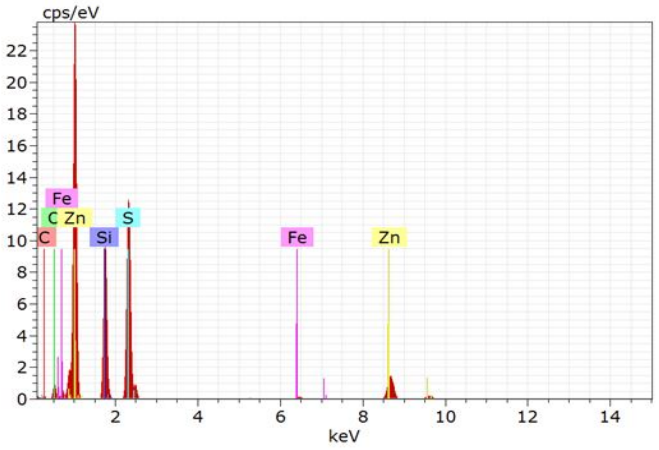

FIGURE 5.10: The EDS spectrum of sample sample AF5Quv1.8 is observed to contain peaks of the expected elements Zn, S, Fe, Si, C and O. A quantification of the peaks reveals an Fe concentration of 1.8%, based on the atomic fraction Fe/(Fe+Zn+S).

of sulfur lying at the film surface. Clusters consisting of S, O and C are also observed in SEM images of most of the other samples, indicating a slight variation in the film composition.

For some of the films on fused silica substrates, unreasonably large values of sulfur have been detected, although no clusters were observed in the region of the samples used for element quantification. From table 5.2 it is seen that overall, the films deposited on fused silica have a S/(Zn + Fe) ratio of approximately 0.95. The films on silicon, on the other hand, are seen to be low on sulfur having a S/(Zn + Fe) ratio of approximately 0.75. These differences are seen for neighbouring samples of similar thickness, and raises the suggestion of the sulfur signals being disturbed by signals from the substrate elements. XPS measurements support this suggestion, as the results reveal films with comparable metal and sulfur concentrations, independent of the substrate. Additionally, the compositions of sample EFES2Si7.2, BF5Si6.5, BF2Si13.5, BF1Quv11.8 and EFES3Si1.9 were confirmed by Rutherford backscattering spectrometry (RBS) results obtained by Prof. Ursula Gibson.

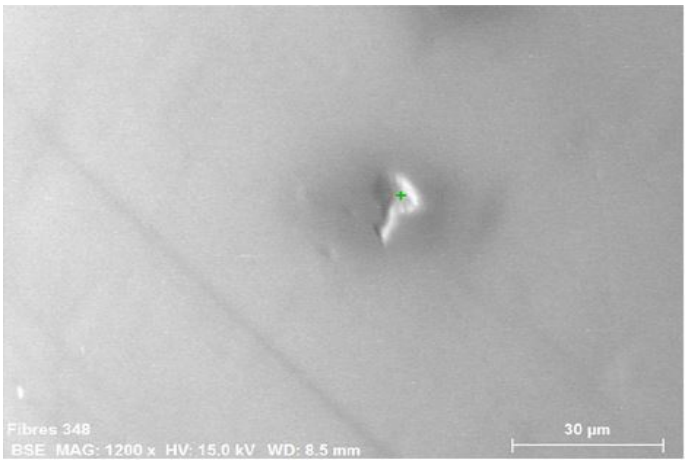

FIGURE 5.11: A SEM image of a sulfur cluster on the surface of sample BF5Quv6.8.

Based on the EDS measurements indicating the films being sulfur deficient, some films were annealed in a sulfur atmosphere, and the elemental Fe source was replaced with FeS in the film depositions. However, as seen in section 5.3.1.3 and 5.3.3 the result of the respective attempts lead to films of lower optical, structural and compositional quality than that of the original films.

5.2.4 X-ray Photoelectron Spectroscopy, XPS

XPS measurements were performed on sample BF5Quv6.8, BFA5Quv6.8, EFES2Quv7.4 and FPFES3Quv by the PhD candidate Mohammadreza Nematollahi. Due to some water cooling issues with the instrument only survey scans could be obtained, using an aluminum X-ray source. All spectra were scaled relative to the intensity of the characteristic carbon peak.

The XPS spectra of sample BF5Quv6.8 and EFES2Quv7.4 are presented in figure 5.12. Peaks corresponding to the expected elements Zn, S, Fe, Si, C and O are observed in both spectra in addition to peaks indicating the presence of ZnS and FeS compounds. With the characteristic carbon peak being calibrated to a binding energy of 284.8 eV, the peaks which seem to confirm the presence of ZnS are found at approximately 1021eV and 1044eV, while that of FeS is observed at 161eV. The fact that the sulfur binding energy is consistent with an Fe-S bond in the BF5Quv6.8 film indicates that iron from the elemental Fe source has successfully substituted an Zn atom, which was the goal of the doping. The Fe-S peak appearing in sample EFES2Quv7.4 is more obvious as FeS was used as iron source in the deposition of this sample. By comparing the spectra of sample BF5Quv6.8 and EFES2Quv7.4, it is clear that the same peaks appear for both

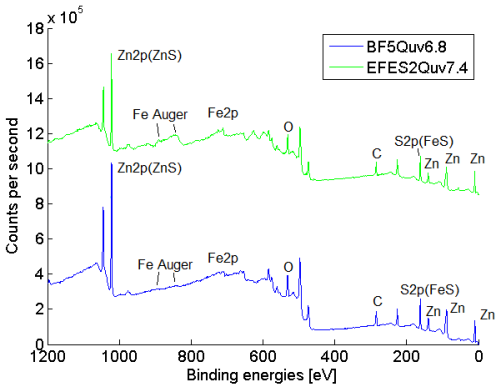

FIGURE 5.12: The XPS spectra of sample BF5Quv6.8 and EFES2Quv7.4 deposited from elemental Fe and FeS as the iron source, respectively, represented by respective blue and green curves. An offset has been added to the spectrum of sample EFES2Quv7.4.

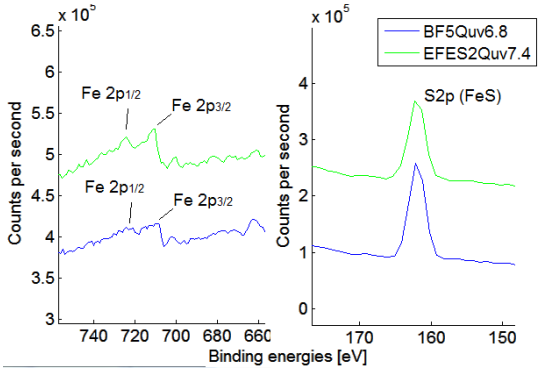

FIGURE 5.13: The XPS spectra of sample BF5Quv6.8 and EFES2Quv7.4 showing the regions where signals of iron would appear. The characteristic peaks corresponding to Fe2p are presented in the left panel while the peak of S2p which seems to be bonded to Fe forming FeS is shown in the panel to the right.

films.

A formation of FeS in sample BF5Quv6.8 seems to be confirmed by comparing the

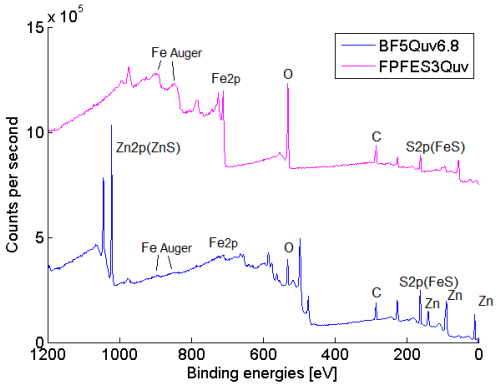

FIGURE 5.14: The XPS spectra of sample BF5Quv6.8 deposited from Fe and ZnS in addition to the pure FeS film in sample FPFES3Quv, represented by blue and pink curves, respectively. An offset has been added to the spectrum of sample FPFES3Quv.

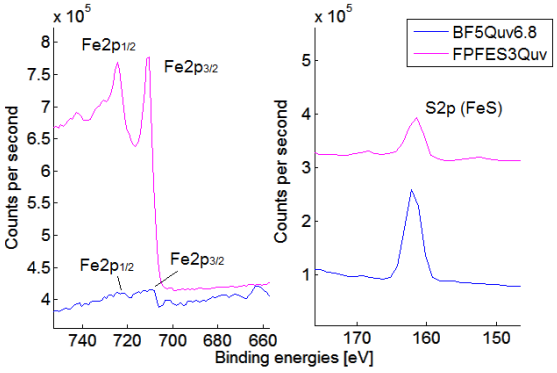

FIGURE 5.15: The XPS spectra of sample BF5Quv6.8 and FPFES3Quv showing the regions where signals of iron would appear. The characteristic peaks corresponding to Fe2p are presented in the left panel while the peak of S2p which seems to be bonded to Fe forming FeS is shown in the panel to the right.

spectra of this sample with that of the pure FeS in sample FPFES3Quv given in figure 5.14. From the figure it is seen that the prominent peaks in the spectrum of the pure FeS film also appear in the spectrum of sample BF5Quv6.8.

The XPS spectra of sample BF5Quv6.8 and BFA5Quv6.8 before- and after being ex-

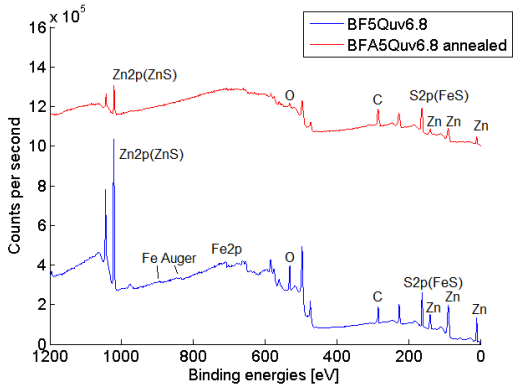

FIGURE 5.16: The XPS spectra of sample BF5Quv6.8 before and after annealing, represented by blue and red curve, respectively. An offset has been added to the spectrum of the annealed sample BFA5Quv6.8.

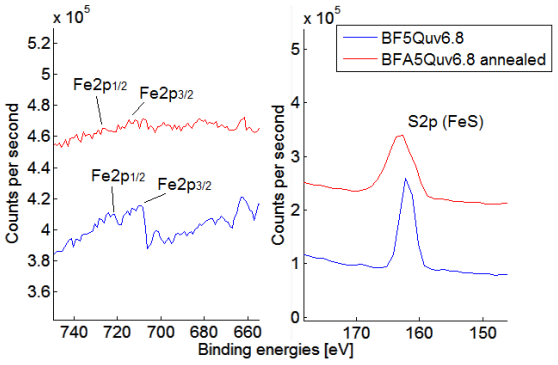

FIGURE 5.17: The XPS spectra of sample BF5Quv6.8 and BFA5Quv6.8 showing the regions where signals of iron would appear. The characteristic peaks corresponding to Fe2p are presented in the left panel while the peak of S2p which seems to be bonded to Fe forming FeS is shown in the panel to the right.

posed to annealing, respectively, are seen in figure 5.16. Peaks corresponding to Zn, ZnS and FeS in addition to the characteristic O and C peaks are observed in both spectra, while those corresponding to Fe2p are hardly evident in the spectrum of the annealed sample. The weak signal of Fe2p could have several explanations: There might be more C present in the annealed sample, suppressing the Fe2p signal, which should be visible independent of the bonding. Another possibility is migration of Fe away from the surface. A third explanation involves a peak broadening of Fe2p due to oxygen incorporation.

In figure 5.13, 5.15 and 5.17 the regions of the spectra where signals from iron would appear, are presented, comparing the iron peaks of sample BF5Quv6.8 with the iron peaks observed for sample EFES2Quv7.4, FPFES3Quv and BFA5Quv6.8, respectively. In figure 5.17 a shift of the $Fe2p_{2/3}$ peak towards higher binding energies is observed for the annealed sample BFA5Quv6.8. This is suggesting oxidation, even though the annealing was performed in an evacuated sulfur atmosphere. Comparing the peak position of S2p which is suggested to correspond to FeS before- and after annealing, a broadening towards higher energies is observed for the annealed film. By studying the similar peaks of the other samples no significant shifts are seen, indicating that no difference of the Fe bonds in the films deposited from elemental Fe or FeS used as the iron source could be revealed by the preliminary survey scans.

5.2.5 Summary of the structural and compositional characterization

To summarize the structural and compositional characterization of the samples, XRD and TEM revealed films consisting of small grains, where the grains in the mixed films of FeS and ZnS were observed to be half the size of the grains in the films doped with iron from the elemental Fe source. From TEM images the iron was seen to be uniformly distributed and the structure of the films was concluded to be hexagonal. EDS measurements showed that Fe doping levels up to 12% were obtained, and from XPS results it was seen that Fe^{2+} had successfully been incorporated in the ZnS lattice by substituting Zn^{2+} atoms.

With the results from the structural and compositional characterization in mind, the optical properties of the films will be presented in the following sections.

5.3 Optical characterization - VIS and UV

This section includes an overview of the data and a determination of the optical constants by analysing the data in the VIS and UV region.

5.3.1 Raw data

In the following section the films are divided into four categories dependent on how they are made: "Fe + ZnS", "FeS + ZnS", "Fe + ZnS in UHV" and "Fe + ZnS annealed". Raw data of each of the four categories will be presented, in addition to a parameterization of the data, that gives a quick overview of all the samples.

5.3.1.1 Transmission measurements

Transmission measurements were performed on the films deposited on transparent substrates and a selection of the resulting spectra from each of the four film categories are presented in the sections below. In Appendix B the transmission spectra of all measured samples can be found.

5.3.1.2 Films deposited with ZnS and Fe source

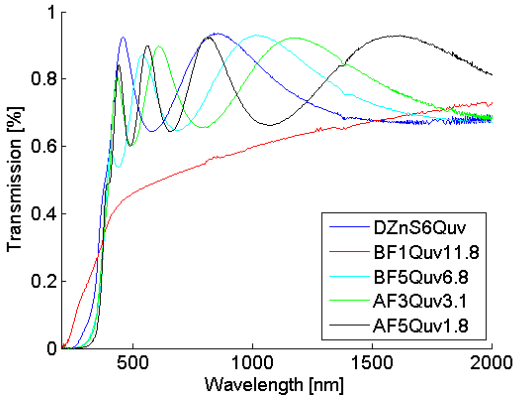

FIGURE 5.18: The transmission of a selection of films made from Fe and ZnS with respect to wavelength, compared to the transmission spectrum of a pure ZnS film.

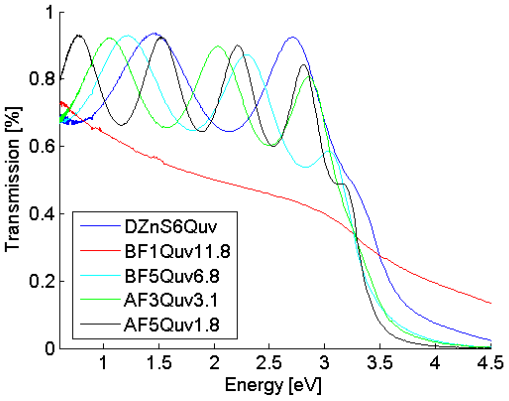

FIGURE 5.19: The transmission of a selection of films made from Fe and ZnS with respect to energy, compared to the transmission spectrum of a pure ZnS film.

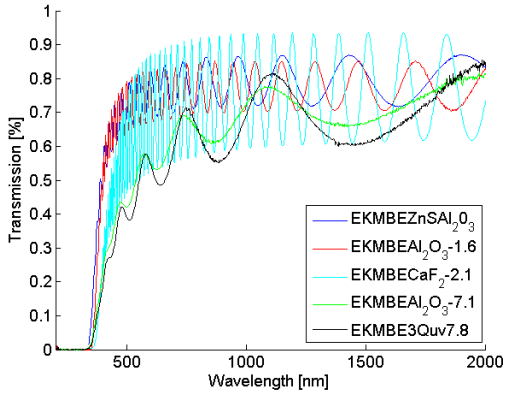

FIGURE 5.20: The transmission of a selection of samples made from Fe and ZnS in UHV plotted with respect to wavelength. The difference in fringe height among the samples are due to different substrates while the density of fringe peaks is dependent on the film thickness.

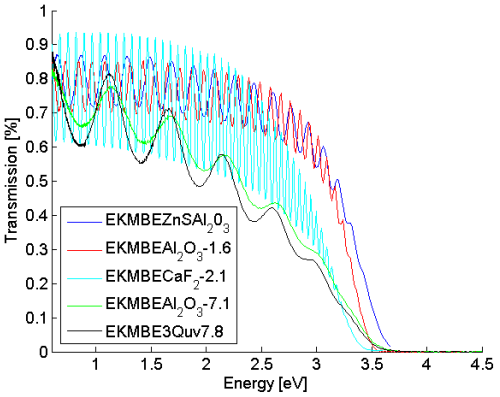

FIGURE 5.21: The transmission of a selection of samples made from Fe and ZnS in UHV plotted with respect to energy. The difference in fringe height among the samples are due to different substrates while the density of fringe peaks is dependent on the film thickness.

The transmission spectra of selected films made from Fe and ZnS by PVD are presented in figure 5.18 and 5.19, plotted with respect to wavelength and energy, respectively, while figure 5.20 and 5.21 show the transmission of selected films made under UHV conditions in molecular beam deposition.

From figure 5.18 and 5.19, it is observed that the PVD films with Fe content less than

10% have transmission coefficients similar to that of the pure ZnS film, whose fringes have a maximum intensity of approximately 93% corresponding to the transparency of the fused silica substrate that is applied. This indicates that the films are completely transparent at these wavelengths.

The transmission of sample BF1Quv11.8 which has a high Fe concentration of 11.8%, shown in figure 5.18 and 5.19, is observed to have a lower intensity than the other films in the selection. This is confirmed by looking at the samples with the naked eye, as the film is observed to have a darker colour compared to the low Fe concentration samples. It is hence obvious that a higher Fe concentration leads to an increase in the absorption. The fact that the transmission spectrum of this sample contains no fringes could be an indication of a spatial non-uniformity in the refractive index or film thickness. It could also imply that the film is conductive. Based on this discussion, it was decided that comparing sample BF1Quv11.8 to the other samples would not be relevant, and will be excluded in the raw data parameterization given in section 5.3.1.5.

The films made in UHV are deposited on CaF_2 and Al_2O_3 substrates in addition to substrates of fused silica and IR quartz. Since these substrates have different values of the refractive index, a variation of fringe height among the different samples occur, as seen by the transmission spectra provided by figure 5.18 and 5.19. The difference in peak density is due to a variation in the film thicknesses. The rolloff in transmission for the films deposited under UHV conditions arises partly because of the large thickness, but there are additional scattering losses due to the development of large crystallites in these films.

From figure 5.19 it might look like the thickness is not only causing a rolloff in the transmission, but also affecting the position of the absorption edge. Studying the behaviour of sample EKMBE$CaF_2$2.1, having a significantly larger film thickness than the other samples presented in the figure, the drop in transmission of this sample appears at significantly smaller energies than sample EKMBE$Al_2O_3$1.6. The evident shift in the transmission drop occurs despite the similar composition of the two samples, with sample EKMBE$Al_2O_3$1.6 containing 1.6% Fe, 0.5% less compared to the Fe concentration of 2.1% in sample EKMBE$CaF_2$2.1.

However, by assigning the complex refractive index a fixed value and varying the film thickness, calculations show that the position of the transmission drop is independent on the thickness, and it is hence believed that a shift in the absorption edge could be due to other parameters like the Fe doping level.

5.3.1.3 Annealed films

As the EDS results initially showed a sulfur deficiency in the films belonging to the "Fe + ZnS" category, it was decided to expose these films for annealing in sulfur atmosphere at 400° for 20 hours in order to increase the sulfur content and hence increase the possibility of incorporating more Fe to the ZnS film. It was later found that the EDS results were influenced by the substrate as discussed in section 5.2.3, XPS measurements show that the films were actually high on sulfur before the annealing, and it is suggested that Fe has reacted with excess sulfur forming FeS_2 or Fe=S rather than being substituted into the ZnS lattice. A presence of FeS_2 and $Fe_{1-x}S$ in Fe:ZnS films exposed to annealing at various temperatures has been reported by Kashyout *et al.* [6]. These films were prepared by an electrodeposition method, and had Zn/Fe ratios of 0.25 and 4.

Additionally, a shift towards higher binding energies of the $Fe2p_{3/2}$ peak was observed, described in section 5.2.4, suggesting an oxidation in the annealed films, although the annealing was performed in an evacuated tube loaded with sulfur.

Hence, the result of the annealing was not as expected. Furthermore, the transmission measurements, of which a selection is shown in figure 5.22 and 5.23, revealed a nonuniformity in the refractive index, which might be an indication of a phase segregation. On this basis, the annealed films are considered not to be a satisfying basis of comparison to the other film categories, and the results of the analysis of these films are therefore presented separately in appendix C.

5.3.1.4 Films deposited with ZnS and FeS source

The transmission spectra of a selection of samples to represent the films deposited from ZnS and FeS source are plotted with respect to wavelength and energy in figure 5.24 and 5.25, respectively. Compared to the samples where an elemental Fe source was used rather than FeS, the samples resulting from the latter source are observed to have a lower transmitted intensity through the entire visible range. In addition, the mixed FeS and ZnS films have a slightly increased short wavelength transmission and extensive smearing of the band edge states. This is confirmed in the raw data parameterization in section 5.3.1.5 below.

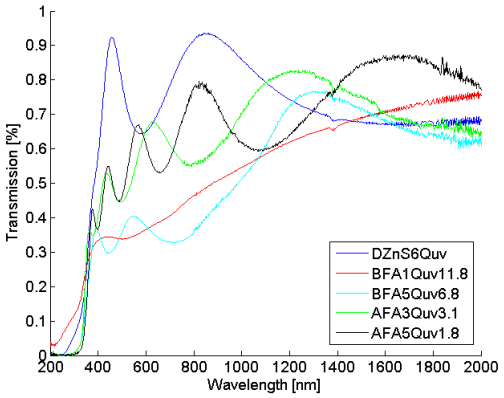

FIGURE 5.22: The transmission of a selection of films made from Fe and ZnS after annealing, compared to the transmission spectrum of a pure ZnS film which has not been exposed to annealing. The spectra are plotted with respect to wavelength.

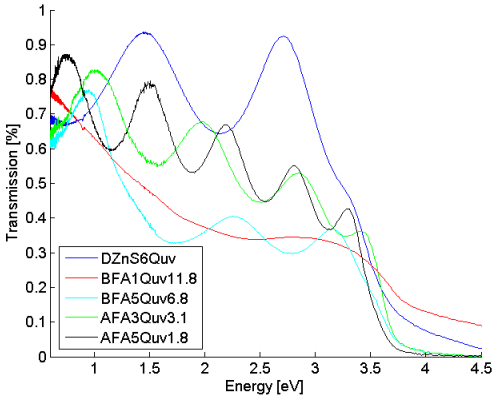

FIGURE 5.23: The transmission of a selection of films made from Fe and ZnS after annealing, compared to the transmission spectrum of a pure ZnS film which has not been exposed to annealing. The spectra are plotted with respect to energy.

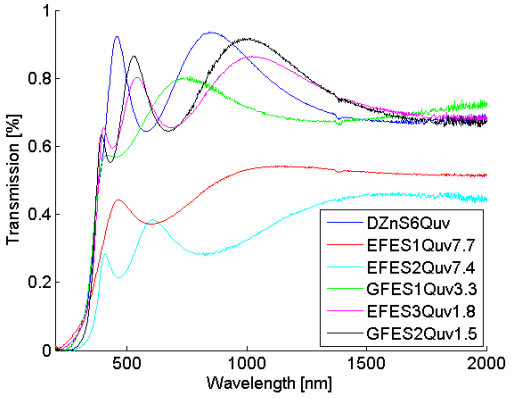

FIGURE 5.24: The transmission of a selection of films made from FeS and ZnS plotted with respect to wavelength, compared to the transmission spectrum of a pure ZnS film.

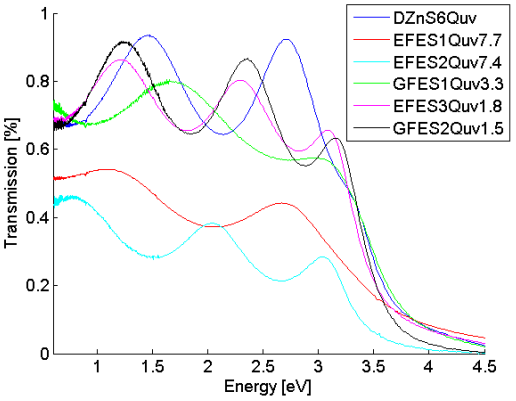

FIGURE 5.25: The transmission of a selection of films made from FeS and ZnS plotted with respect to energy, compared to the transmission spectrum of a pure ZnS film.

5.3.1.5 Raw data parameterization

As can be seen from table 5.2, many samples were made and measured. In order to get a quick overview, a simple parameterization scheme was used to summarize the results.

From the previous sections, it is seen that common for all samples is the sudden drop in the transmission when the absorption edge is reached at lower wavelengths. This region is emphasized when the transmission is plotted with respect to energy, as observed

in the transmission plots of selected samples in the four categories seen in figure 5.19, 5.21, 5.23 and 5.25. From the figures, it is evident that the absorption edge is tilted and shifted among the various samples. In order to compare this behaviour for all the samples, it could be convenient to parameterize this feature as an "absorption knee", whose position is determined according to the illustrating example of the AF5Quv1.8 film in figure 5.26: An almost horizontal line representing the maximum transmission is drawn in addition to a second line being an extension of the slope of the intensity drop. The absorption knee parameter is then found in the intersection of the two lines, in units of energy.

The resulting absorption knees of all of the samples (except sample BF1Quv11.8 be-

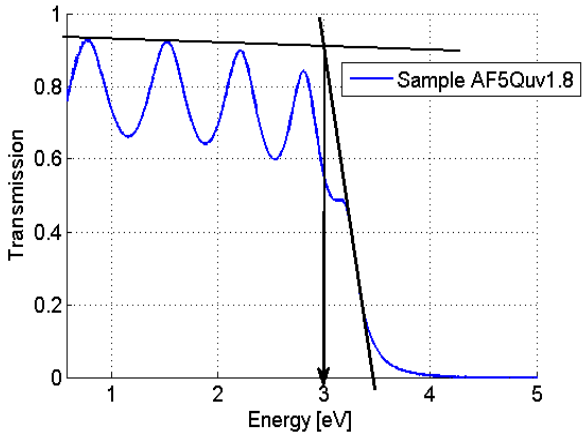

FIGURE 5.26: An illustration of how the absorption knee parameter is determined by the intersection of two lines representing the maximum transmission and an extension of the slope of the intensity drop. In this illustration, the absorption knee of sample AF5Quv1.8 was found to be 3 eV.

ing excluded for the reasons given in section 5.3.1.2) are found in the overview in figure 5.27. From the overview the position of the absorption knee is observed to be shifted towards lower energies with increasing Fe concentration. This trend could be an indication of a decrease in the band gap in the films when more Fe is added. However, as discussed in detail in section 5.3.3, the slightly increased high energy transmission and extensive smearing of the band edge states for higher doping levels are seen to be the broadening of an Urbach tail. The dependence of the absoption knee position with increasing Fe content, given by the slope of the trend lines, is seen to vary in the four categories, and the films made under UHV conditions appear to have the largest effect of the doping, concerning the absorption knee parameter. However, the apparent position of the knee is affected by the thickness, and most of these films were thicker than those deposited by the PVD method.

By studying the absorption coefficients of the films in the wavelength range 1000-2000nm,

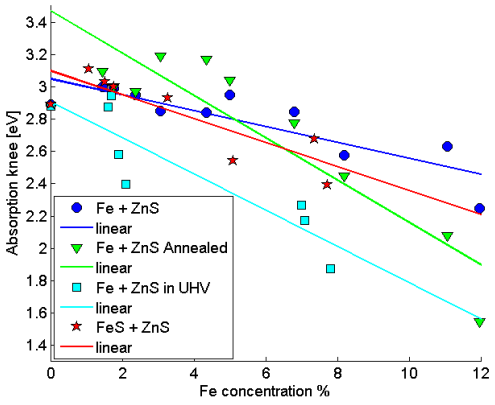

FIGURE 5.27: The figure shows a summary of the absorption knee positions of the samples with respect to the Fe concentration in the films. In addition, a trend line is drawn for each of the four film categories "Fe + ZnS", "Fe+ ZnS annealed", "Fe + ZnS in UHV" and "FeS + ZnS", given in dark blue, green, light blue and red curve, respectively. The positions of the absorption knees are given in units of eV.

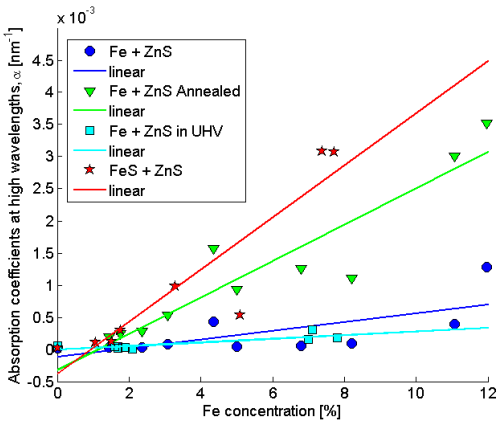

FIGURE 5.28: A summary plot of the absorption coefficients in the wavelength range 1000-2000nm with respect to the Fe content of the films. Trend lines to represent the four different film categories "Fe + ZnS", "Annealed Fe + ZnS", "FeS + ZnS" and "Fe + ZnS in UHV", are represented with dark blue, green, light blue and red colour, respectively.

presented in figure 5.28, the effect of Fe doping is observed to be greatest in the films made in the depositions where the FeS source is used, followed by the annealed samples. The vacuum level during deposition does not seem to affect the doping effect in terms of the absorption of the samples. The increase in the absorption is most likely caused by defects being introduced in the films by the doping.

5.3.2 Data reduction

Although examination of the transmission versus energy gives a first impression of the trends, the intrinsic properties of the material are described by the optical constants n and κ in the refractive index. Different ways of determining the complex refractive index, $\tilde{n} = n + i\kappa$, were therefore investigated. These techniques involve modeling by using the Swanepoel method [68], the Puma software [69] and ellipsometry measurements. An additional method of calculating the absorption A based on transmission T and reflection R measurements and the relation $1 = T + R + A$ are also performed. In the following sections the different data reduction techniques are presented, including their strengths and weaknesses, in addition to a description of the Urbach tail.

5.3.2.1 Urbach tail

At the absorption edge, the absorption coefficient tails off in a simple exponential manner as $\alpha(E) = \alpha_0 e^{-n}$. When the absorption follows such a curve with $n = 1$, the film is shown to have an Urbach tail into the band gap, which in turn is caused by dislocations and impurities close to the band gap edge [71]. Therefore a linear curve in the plot of $\ln(\alpha)$ versus energy hv, also known as an Urbach plot, would confirm a presence of the Urbach tail. The Urbach energy E_U is expressed by the inverse slope of this linear region, $E_U = (\frac{\mathrm{d}(\ln \alpha)}{\mathrm{d}hv})^{-1}$, referring to the width of the exponential absorption edge.

Urbach plots based on the absorption coefficient calculated directly from the transmission as well as the absorption coefficient retrieved from the Swanepoel model are drawn for selected samples. As seen in section 5.3.3.1 and 5.3.3.5 Urbach tails were observed in all of the investigated samples, and the Urbach energies based on the raw transmission are in agreement with the those calculated from the Swanepoel model.

5.3.2.2 The Puma model

The first modeling technique involves a free software available online, called Puma. Based on repeated calls to minimization algorithm, the Puma software returns estimations of the optical constants n and κ in addition to the film thickness, with the measured transmission spectrum of the thin film serving as the main input to the model. Other user defined parameters are maximum number of iterations, real refractive index of the substrate, upper and lower limits for the constants to be estimated: the film thickness and n and κ in refractive index. It also asks for an estimate of the absorption edge, and appears to use a model constrained to a two segment linear fit for κ.

The modeling procedure is performed in three steps/runs. The first run serves as a "survey scan" as it consists of few iterations and the limits constitute a large range of possible values of the constants to be determined. The second run is based on the outcome of the first run, but has a narrower acceptable error between the back calculated transmission and the film measurement. This step is repeated in the third and final run, where the maximum number of iterations is assigned a very large value, and the intervals are significantly narrowed compared to step 2. The estimated values that give the least quadratic error are returned.

As implied by the description above, the Puma modeling is a straight forward process, and has a convenient input method. The model has shown to give the best results for the films whose transmission spectra have several and well defined fringes, like the

film in sample AF5Quv1.8 shown in figure 5.29. The good fit between the measurements and the model observed in the figure implies that the estimations of the optical properties of this film, given by n and κ in figure 5.30, are reliable.

The Puma model has been shown to be inadequate for the films whose transmission spectra have lower intensity and contain fringes that are less well defined. These include annealed films and mixed films of FeS and ZnS. The result of modeling such a film, with the mixed FeS and ZnS film EFES2Quv7.4 being the example, is shown in figure 5.31. As seen by the figure, the model seems to have negelected the transmission peak at the lowest wavelength, resulting in a large deviation of the experimental and calculated film thickness, which reads 232nm and 72 nm, respectively. Based on the unsuccessfull fit, the estimation of the complex refractive index, presented in figure 5.32 is considered to be unreliable.

Another weakness in the Puma model is the fact that it uses two line segments to characterize κ, meaning it assumes that the film contains only one absorption feature, which would refer to the absorption edge of the films in this project. When the absorption edge is reached at lower wavelengths, a decreasing value of κ stabilizes at a value that remains constant for all higher wavelengths. In other words, if the film contains another absorption feature at higher wavelengths which could contain information about the atomic structure of the film, this absorption will be neglected by the Puma software, and relevant features of the sample could be withholded.

Although that the Puma model has some great advantages, it is seen by the discussion above that it also has its limitations. Since the software has shown to have problems modeling both the annealed films as well as the films deposited with FeS and ZnS source, constituting half of the data foundation in this review, the Puma model is considered not to be an appropriate method in the data reduction process in this project. On this basis, the Puma results will only be presented in the overview figures in the optical modeling results found in section 5.3.3, as a comparison to the other modeling techniques.

5.3.2.3 Transmission

A simple way of estimating the absorption of the films, without fully determining κ in the expression of the refractive index, is to calculate the absorption coefficient α directly from the transmission measurements using the inverse logaritmic relation between the

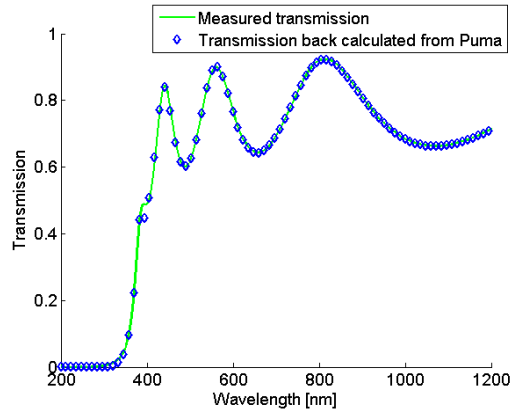

FIGURE 5.29: The figure shows a plot of the measured transmission of sample AF5Quv1.8 in addition to the transmission calculated reversely with the estimated values of n and κ returned by Puma, indicated with green and blue colour, respectively.

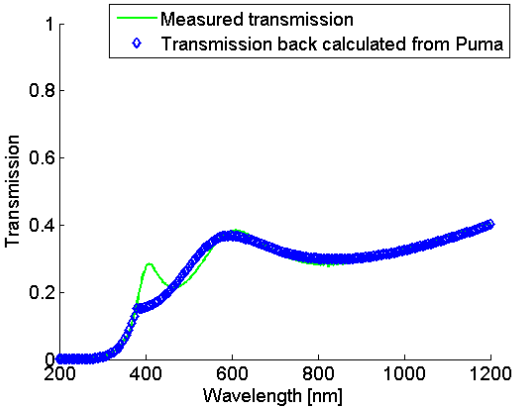

FIGURE 5.31: The figure shows a plot of the measured transmission of sample EFES2Quv7.4 in addition to the transmission calculated reversely with the estimated values of n and κ returned by Puma, indicated with green and blue colour, respectively.

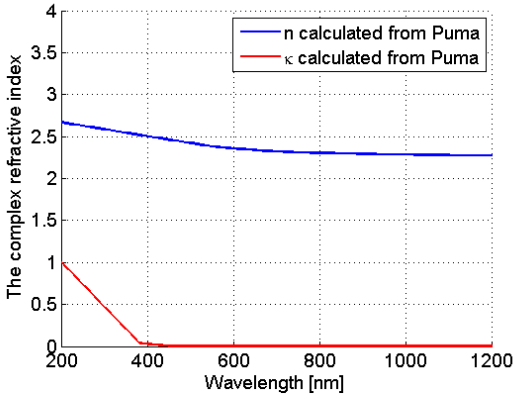

FIGURE 5.30: The figure shows the real- and imaginary part of the refractive index of sample AF5Quv1.8 calculated by the Puma software, given by curves of n and κ in blue and red colour, respectively.

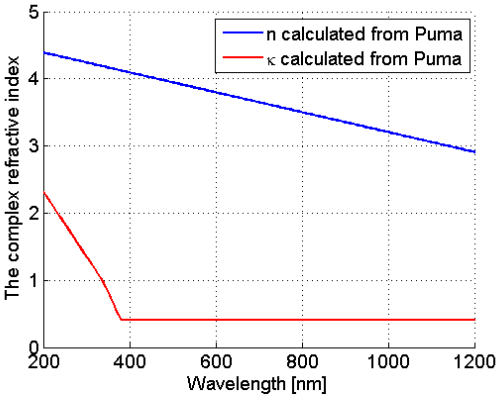

FIGURE 5.32: The figure shows the real- and imaginary part of the refractive index of sample EFES2Quv7.4 calculated by the Puma software, given by curves of n and κ in blue and red colour, respectively.

transmission T and the absorption derived in section 4.2.4 yielding $\alpha = \frac{1}{d}\ln\left(\frac{1}{T}\right)$, where d is the film thickness. This is not strictly correct for thin films, but it is a good approximation in the low wavelength region where no interference fringes remain. By using the expression which is ignoring the reflection of the film, a typical error is calculated to be on the order of 10-15% in α when the transmission is 10%, which is the case at a wavelength of approximately 350nm. The error gets smaller at lower wavelengths, e.g. the error in α shrinks to 5% when the transmission is 2%. A discussion of how disregarding the film reflection affects the results of the optical analysis is found in section 5.3.3.5 where the differences between the Swanepoel method and the data reduction based on

the raw transmission are described.

The absorption coefficient could be applied in an Urbach plot and in Tauc plots to get information about dislocations in the film and to determine the optical band gap of the film, respectively. In literature, it is seen that several authors have included the indirect band transition in Fe:ZnS thin films in their reviews [5], [8]. For this reason, the determination of the indirect band gap of the films are included in the results presented in section 5.3.3 in addition to the direct band gaps. However, it follows from the discussion in section 5.3.3.1, where Urbach plots are involved, that the residual curvature observed in the absorption coefficients, is likely to be caused by defects near the band edges, rather than being an indication of an indirect band gap.

5.3.2.4 Ellipsometry

Similar to the Puma method, the model dependent ellipsometry results are based on a optimization technique, where estimated values of the optical constants that give the least mean square error are returned. As described in section 4.2.8, trial values of the optical constants to be determined serve as input parameters. These values are in turn fitted and used in a reverse calculation of the measured constants Ψ and Δ and assigned to the constants n and κ in the refractive index, in addition to the corresponding ϵ_1 and ϵ_2 in the dielectric function, when the mean square error is at an acceptable level.

Although that the principles of the ellipsometry modeling might seem straight forward, the fitting of the parameters is a complex process. In order to assign reasonable values to the constants, the model is built up layer by layer, starting with a substrate layer followed by a layer to represent the film. In addition of involving parameters like thickness, surface roughness, and back reflection, Tauc-Lorentz oscillators and Lorentzian functions could be applied in order to assign physical properties to the film in terms of optical band gap and metallic behaviour, respectively.

For a model where several fitting parameters are involved, there is a possibility of having more than one unique solution. This is important to have in mind in the parameter fitting process, as a low mean square error could be obtained for multiple parameter combinations. For this reason, the modeling has to be done carefully in order to avoid choosing a solution giving an incorrect description of the film.

Another challenge with the ellipsometry technique appeared in the analysis of the thicker films, as the model seemed to have difficulties handling the high fringe density of the

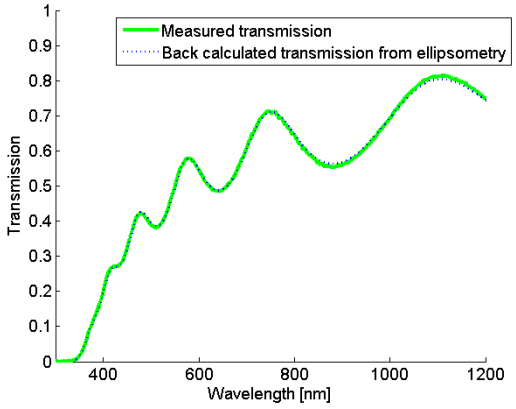

FIGURE 5.33: The figure shows a plot of the measured transmission of sample EKMBEQuv7.8 in addition to the transmission back calculated from the estimated values of n and κ retrieved by the ellipsometry, indicated with a green and blue dotted curve, respectively.

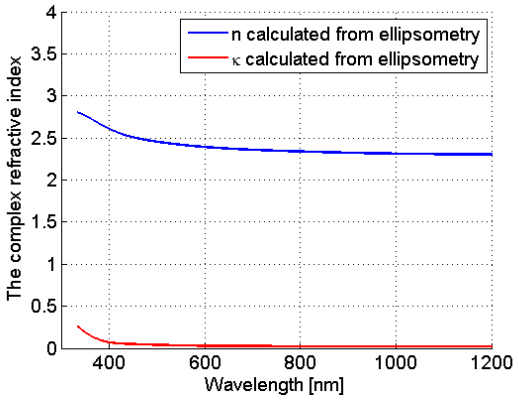

FIGURE 5.34: The figure shows the real and imaginary part of the refractive index of sample EKMBEQuv7.8 resulting from the ellipsometry modeling, given by curves of n and κ in blue and red colour, respectively.

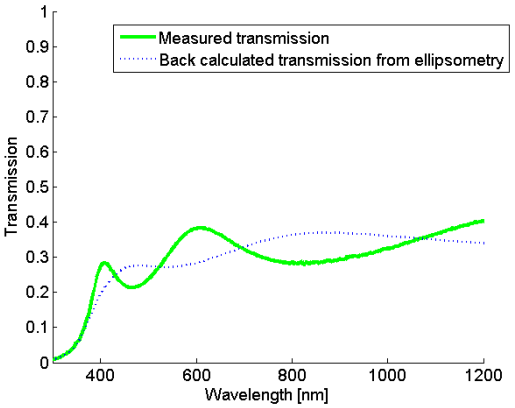

FIGURE 5.35: The figure shows a plot of the measured transmission of sample EFES2Quv7.4 in addition to the transmission back calculated from the estimated values of n and κ retrieved by the ellipsometry, indicated with a green and blue dotted curve, respectively.

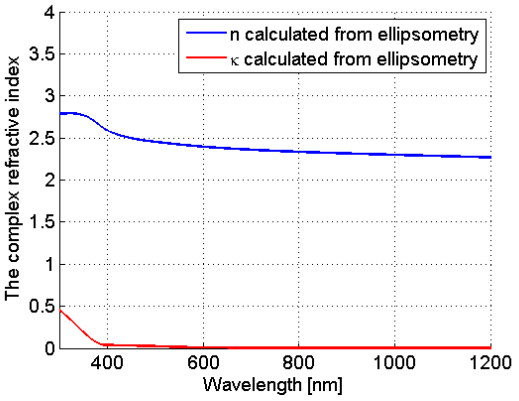

FIGURE 5.36: The figure shows the real and imaginary part of the refractive index of sample EFES2Quv7.4 resulting from the ellipsometry modeling, given by curves of n and κ in blue and red colour, respectively.

reflection spectra of these films. This is actually opposite to the experience with the other modeling methods where a large number of fringes are preferred in order to get a good result. In this way the ellipsometry is seen to be a convenient complementary method to the other modeling techniques.

An example which illustrates a good fit between the ellipsometry modeling and the physical film is shown in figure 5.33, where the plots of the measured transmission of sample EKMBEQuv7.8 and the transmission spectrum back-calculated from the results

from the ellipsometry modeling are seen to overlap perfectly. The complex refractive index values used in the back-calculation are shown in figure 5.34.

In the case of sample EFES2Quv7.4, on the other hand, the measured and modeled transmission presented in figure 5.35 are observed to be inconsistent. Unsatisfying modeling results have been obtained by Swanepoel and Puma as well for the same film, which speaks for a general difficulty in the modeling of a film whose transmission spectrum contains fringes at low transmitted intensity. This film was later found by RBS to consist of two layers, most likely consisting of Fe:ZnS and FeS_2. The retrieved values of n and κ, underlying the back calculated transmission of sample EFES2Quv7.4 are presented in figure 5.36.

Despite the issues that may occur using this model, the ellipsometry has proved to be a powerful method when the modeling is done carefully, and it retrieves more information about the optical properties of the film than compared to the other data reduction techniques presented in these sections. The ellipsometry modeling in this project is performed by the Postdoctoral candidate Zahra Ghadyani.

5.3.2.5 The Swanepoel method

While the other data reduction methods presented in the previous sections are based on a optimization technique, the Swanepoel method is more analytical within the high wavelength range. It is a very flexible modeling technique when it comes to determining the values of n and κ, as the calculation of the refractive index is based on the transmission of the film, with the envelope curves serving as input data. The equations used in the model are well presented in the Swanepoel paper [68], and will not be repeated here. The model was implemented in Matlab© and an example of such a Matlab© script could be found in Appendix E [63]. In the following, the modeling procedure is described step-by-step:

1. Model input: The measured transmission spectrum of the film and the corresponding envelope functions T_M and T_m representing the maximum and minimum values of the intensity of the fringes in the transmission spectrum, respectively, serve as main input to the model. Film thickness and the refractive index of the substrate are additional input parameters that need to be included.

2. Running the model: By running the model an estimated value of n is returned. This real part of the refractive index is further used in the calculation of the imaginary part of the refractive index. As a reality check, the values of n and κ

retrieved by the model are used in a reverse calculation of the transmission and the corresponding envelope curves, giving an indication of the fit between the model and the physical film.

3. Modifications of the model: In the case of most of the films, the real refractive index is indeterminate at low wavelengths, corresponding to the UV region, where T_M and T_m coincide. As a result, a lot of noise appears in n and in the back calculated transmission spectrum at these wavelengths. Having noise in this wavelength region below 400nm is very unfortunate, as this is the range of interest considering the absorption edge of the film. In order to get rid of the noise, which involves obtaining a more physical value of the real refractive index, n is extrapolated at the low wavelengths. The extrapolated values of n is given on the form $ax^b + c$, whose constants are calculated by the curve fitting tool in Matlab©.

4. Running the script with modifications: By running the script a second time, but this time with the modified version of n achieved after the first run as input, rather than T_M and T_m, the model is likely to show a more satisfying match with the physical film. In the cases where the fit seems to have a potential of improvement, the extrapolation of n should be fine tuned. Additionally, an adjustment of the film thickness should be performed.

5. Model results: With an appropriate value of n, which give a satisfying match between the modeled and measured transmission of the film, a reliable value of κ, whose calculation is based on n, could further be used to determine the absorption of the film. The absorption could in turn be used in a Tauc plot for band gap determination, and it could be applied in an Urbach plot, to get information about dislocations and defects in the film.

As for any model, the Swanepoel method has its strengths and weaknesses. The description above indicates that it has a weakness at lower wavelengths since n is showing an unphysical oscillating behaviour and containing a significant amount of noise in this region, which requires a modification of n. In the large wavelength range, on the other hand, the strengths of the model become apparent, as both the transmission and reflection are accounted for. This leads to an absorption spectrum free of fringes, unlike the absorption approximated directly from the transmission measurements, showing an unphysical oscillating behaviour at low energies, as seen in section 5.3.3.5.

The modeling of the films whose transmission spectra have an approximately constant envelope value at high wavelengths before it suddenly drops towards zero at the absorption edge proved to give satisfying results. Applying the Swanepoel method to sample

EKMBEQuv7.8, illustrates how this model behaves at its highest potential. As seen in figure 5.37, the fringes of the reverse calculated and measured transmission, given by the blue and green curve, respectively, are observed to overlap perfectly after applying the modified value of n shown by the green curve in figure 5.38.

However, modeling films whose transmission drops in two steps, like in the case of sample BFA5Quv6.8 shown in figure 5.39, is seen to give an unsatisfying result. The Swanepoel model seems to have problems handling the conflict between a significant change in fringe height and maintaining a constant value of the film thickness, even when extrapolated values of n are applied at low wavelengths, shown in figure 5.40. This leads to a poor match between the interference fringes of the transmission calculated by the model and that of the measured transmission, as seen by figure 5.39.

However, the Swanepoel model is seen to be the most flexible of the models used in this project and is considered to give reliable results for a satisfying number of films. The Swanepoel model was applied to a selection of samples and the results are presented in section 5.3.3.5. In the same section the results provided by the Swanepoel model is compared to that of the other models discussed in this data reduction section.

5.3.2.6 Transmission and reflection measurements (1-T-R)

Another option to get information about the absorption of the film is by utilizing the fact that what is not transmitted nor reflected from the sample must be absorbed. Hence, by measuring the transmittance and reflection and applying the relation $1 = A+T+R$, with A, R and T being the absorption, reflectance and transmittance, respectively, the absorption could be determined. In figure 5.41 and 5.42 A, R and T of sample DZnS6Quv and BF5Quv68 are presented, respectively.

However, by expressing the absorption as $A = 1 - T - R$ a phase shift in R is ignored, and this becomes significant at low wavelengths where κ in the refractive index has a large value. Applying a correction $\alpha = -1/d \cdot \ln(T/1 - R)$, where d is the film thickness, at low wavelengths was however shown to be unsuccessful. The reflection is sensitive to the incident angle and thus the transmission and reflectance values do not correspond exactly. This leads to errors in the absorbtion, as shown in figure 5.41 and 5.42.
Since the values obtained for the absorption using the $A = 1-R-T$ relation are seen to be imprecise, the estimated band gaps based on this absorption are presented separately in Appendix D. The appendix also contains the reflection, transmission and absorption

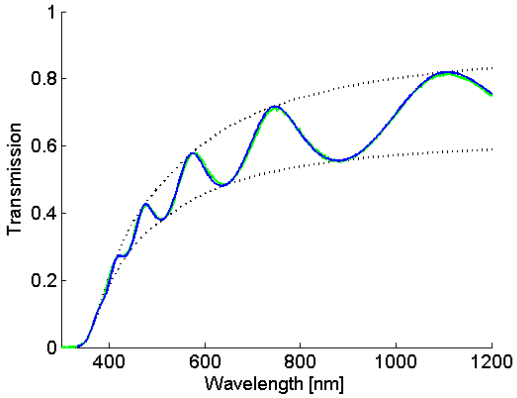

FIGURE 5.37: The figure shows a plot of the measured transmission of sample EKMBEQuv7.8 indicated by the green colour, in addition to the calculated transmission with corresponding envelopes of the same sample given by the blue and black dotted curve, respectively. The calculated transmission is based on the value of the real part of the refractive index, n given by the Swanepoel model.

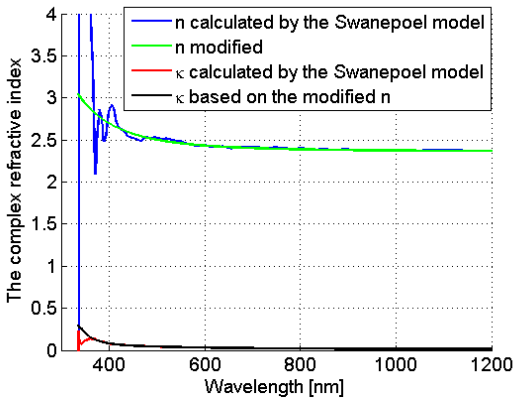

FIGURE 5.38: The figure shows the real and imaginary part of the refractive index of sample EKMBEQuv7.8 calculated by the Swanepoel model, given by curves of n and κ in blue and red colour, respectively. In addition, the modified n-values and the corresponding values of κ resulting from an extrapolation of n at low wavelengths are presented by the green and black curves, respectively.

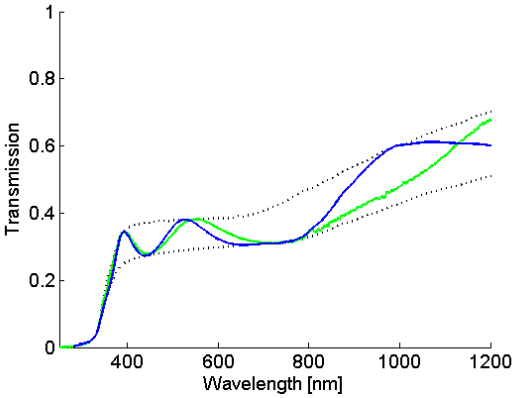

FIGURE 5.39: The figure shows a plot of the measured transmission of sample BFA5Quv6.8 indicated by the green colour, in addition to the calculated transmission with corresponding envelopes of the same sample given by the blue and black dotted curve, respectively. The calculated transmission is based on the value of the real part of the refractive index, n given by the Swanepoel model.

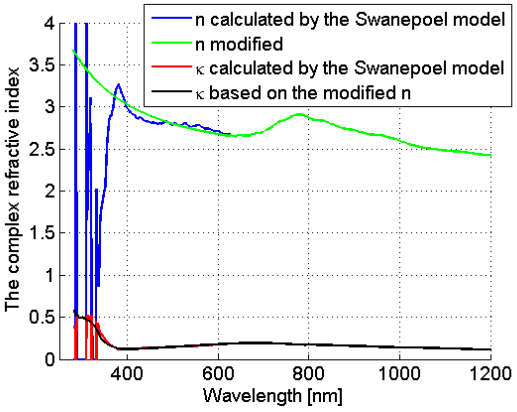

FIGURE 5.40: The figure shows the real and imaginary part of the refractive index of sample BFA5Quv6.8 calculated by the Swanepoel model, given by curves of n and κ in blue and red colour, respectively. In addition, the modified n-values and the corresponding values of κ resulting from an extrapolation of n at low wavelengths are presented by the green and black curves, respectively.

plots of the samples selected for reflection measurements, being similar to the plots in figure 5.41 and 5.42.

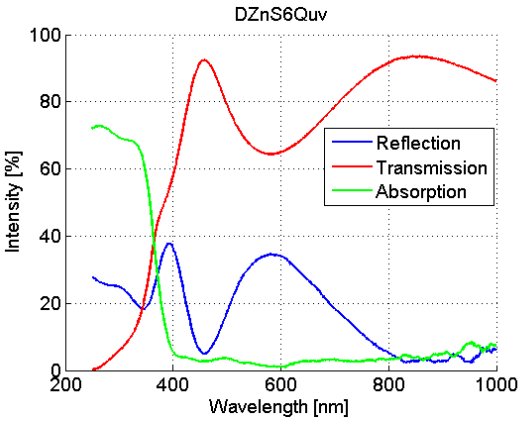

FIGURE 5.41: The measured reflectance- and transmittance spectra of sample DZnS6Quv consisting of pure ZnS, in addition to the calculated absorption.

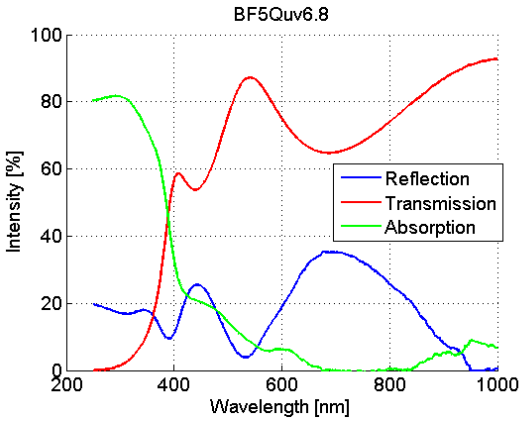

FIGURE 5.42: The measured reflectance- and transmittance spectra of sample BF5Quv6.8 consisting of pure ZnS, in addition to the calculated absorption.

5.3.3 Optical modeling results

A selection of nine samples, where three films of different composition from each of the "Fe + ZnS", "FeS + ZnS" and "Fe + ZnS in UHV" categories are included, forms the basis of the samples being subject for a more comprehensive investigation. The selection consists of the samples EKMBE$Al_2O_3$1.6, AF5Quv1.8, EFES3Quv1.8, EKMBE$CaF_2$2.1, AF3Quv3.1, GFES1Quv3.3, EKMBEQuv7.8, BF5Quv6.8 and EFES2Quv7.4. By applying the different models discussed in section 5.3.2, n and κ were estimated for the selected films. From κ the absorption coefficient α was determined and further used in calculations of the direct- and indirect band gaps of the films in addition of being applied in the estimation of the Urbach energy E_U. In the following section, starting with the simplest method of transmission, the results of the different modeling techniques will be presented and discussed.

5.3.3.1 Transmission

As discussed in section 5.3.2.3, studying the raw transmission spectra is considered to be the simplest way to get an overview of the films. Figure 5.43 and 5.44 illustrate how the absorption coefficient found by utilizing the relation between α and T given by equation 4.8 in section 4.2.4 is applied in the drawing of direct- and indirect Tauc plots, respectively, in order to estimate the direct- and indirect band gap of sample BF5Quv6.8. The band gap values of 3.51 eV and 2.51 eV, respectively, are found in the intersection between the trend line of the Tauc plot and the energy-axis, as indicated by the arrows. Additional trend lines are drawn to illustrate the error of the band gap

determination. The error occuring for ignoring the reflection has shown to have a typical value of 0.004 eV for the direct band gap and 0.25 eV for the indirect band gap, according to a discussion in section 5.3.3.5.

This method of estimating the band gap is applied to a large number of samples, and

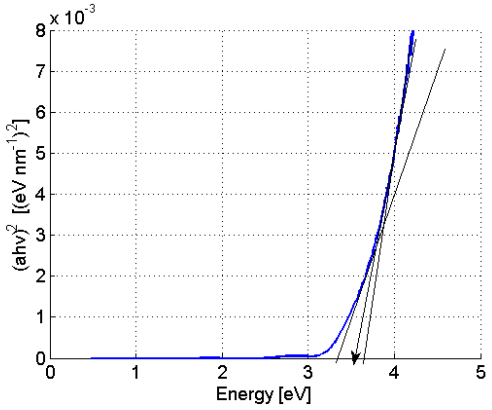

FIGURE 5.43: The figure illustrates how a direct Tauc plot is used to determine the direct band gap of sample BF5Quv6.8. The band gap value of 3.51 eV is found in the intersection of the trend line and the energy-axis, indicated by the arrow. Additional trend lines are drawn to illustrate the error of the band gap determination.

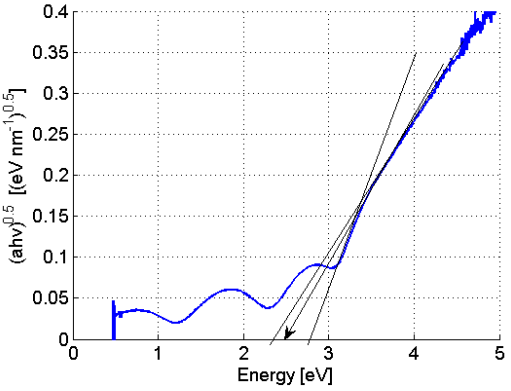

FIGURE 5.44: The figure illustrates how an indirect Tauc plot is used to determine the indirect band gap of sample BF5Quv6.8. The band gap value of 2.50 eV is found in the intersection of the trend line and the energy-axis, indicated by the arrow. Additional trend lines are drawn to illustrate the error of the band gap determination.

the resulting direct- and indirect band gaps with errorbars included, are presented in figure 5.45 and 5.46, respectively. From figure 5.45 it is seen that the direct band gap is quite stabile and a bit lower than the theoretical value of pure ZnS yielding 3.7 eV [61], and it hence seems like the Fe doping concentrations used in this project have little effect on the direct band gap.

Since other authors have modeled the behaviour of Fe:ZnS films using an indirect band gap, the indirect band gap model is applied to the samples although the band structure calculations do not support the development of a strong indirect band gap for the doping levels used in this review [72]. This speaks to a presence of other features in the film, such as defects, leading to the residual curvature observed in the absorption coefficients, which in turn can be perceived as an indication of an indirect band gap.

By studying the result from the indirect band gap model shown in figure 5.46, a decrease of the band gap with respect to Fe concentration is observed. The indirect band gaps of the films made under UHV condition are seen to have overall larger values than

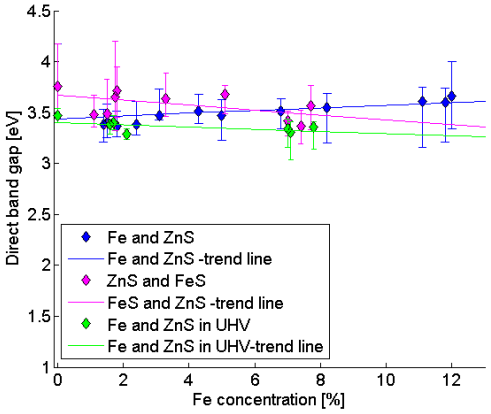

FIGURE 5.45: An overview of the direct band gaps of the films in the series "Fe + ZnS", "FeS + ZnS" and "Fe + ZnS in UHV", with (additional) errorbars and trendlines for the different series. The direct band gaps are estimated by direct Tauc plots based on the raw transmission measurements.

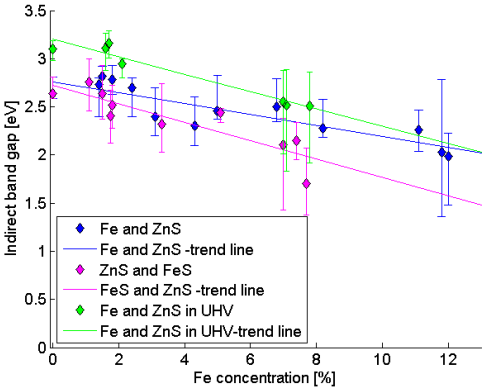

FIGURE 5.46: An overview of the indirect band gaps of the films in the series "Fe + ZnS", "FeS + ZnS" and "Fe + ZnS in UHV", with (additional) errorbars and trendlines for the different series. The indirect band gaps are estimated by indirect Tauc plots based on the raw transmission measurements.

that of the two other series. Such a trend of a decreasing indirect band gap with increasing Fe concentration has also been presented by others for similar materials. However, from the Urbach plots in section 5.3.3.2 it is suggested that dislocations and impurities are present in the films. The amount of these increases and they appear deeper into the forbidden band as the doping level increases. This could explain the decrease in the indirect band gap model when more Fe is added to the films, observed in figure 5.46.

5.3.3.2 Urbach tail

By plotting the logarithm of the absorption coefficient with respect to photon energy hv an Urbach plot is created. As seen by the Urbach plots in figure 5.47, a linear curve in the absorption edge region could be observed for all investigated samples, indicating a presence of the Urbach tail attributed to disorder in the films. The corresponding Urbach energies E_U determined by the inverse slopes of the absorption in the linear Urbach region from figure 5.47, are presented in figure 5.48. From the latter figure a general increase in E_U is observed with increasing Fe content, indicating a broadening of the exponential absorption edge when more Fe is added to the films. This would speak for defects being positioned at an increasing depth into the band gap for films with higher doping level.

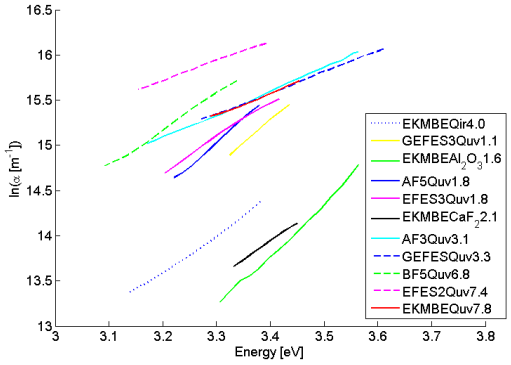

FIGURE 5.47: Urbach plots based on the absorption coefficients determined directly from the transmission spectra of selected samples.

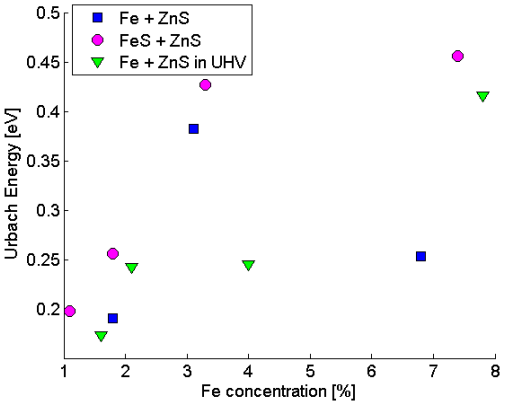

FIGURE 5.48: The figure shows the Urbach energies E_U of selected samples from the three different categories "Fe + ZnS", "FeS + ZnS" and "Fe + ZnS in UHV", corresponding to the inverse slopes of the Urbach plots of the same samples, presented in figure 5.47.

5.3.3.3 The complex refractive index at 1000nm wavelength

Determination of the refractive index $\tilde{n} = n + i\kappa$ is a more sophisticated way of studying the optical properties of the samples. In order to see whether any structural effects could have caused a change in the polarity of the films, it would be convenient to investigate the complex refractive index at high wavelengths. By applying the different modeling techniques discussed in section 5.3.2, estimations of n and κ at 1000nm wavelength were performed for a selection of samples.

In figure 5.49 an overview of the values of n at 1000nm wavelength are presented for films in the "Fe + ZnS", "FeS + ZnS" and "Fe + ZnS in UHV" categories. Overall, little change in n with respect to the Fe concentration was seen, and there is a good agreement between the models. In the "Fe + ZnS" series deposited both by PVD and under UHV conditions, n appears to be stable at approximately 2.3, which is in agreement with the published value of the hexagonal ZnS structure [73]. The molecular beam deposited sample EKMBECaF$_2$2.1 consisting of 2.1% Fe is an exception, with an n-value of 2.5 resulting from the Swanepoel estimations. The fact that this film was deposited on a different substrate compared to the other samples could have lead to the larger value of n, although this was taken into consideration in the modeling process.

The real refractive indices of the films in the "FeS + ZnS" series are observed to deviate from that of the other samples in the two "Fe + ZnS" categories, which could reflect the

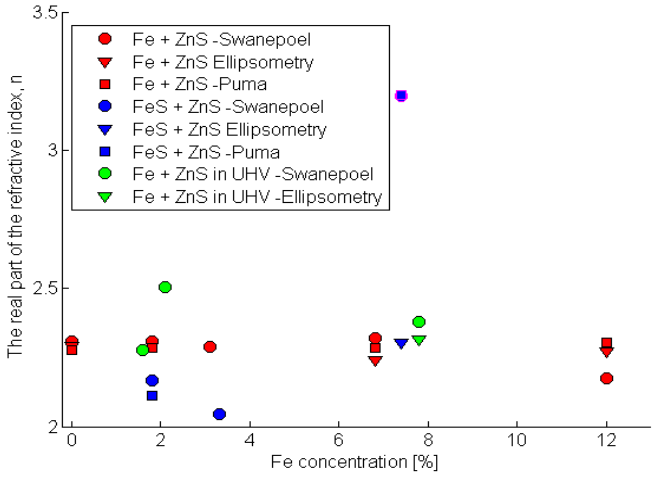

FIGURE 5.49: An overview of the real part of the refractive index n at a wavelength of 1000nm. The values are retrieved by the Swanepoel model, ellipsometry and the Puma model, indicated by a circle, triangle and a square, respectively, for films in the different categories "Fe + ZnS", "FeS + ZnS" and "Fe + ZnS in UHV". Sample EFES2Quv7.4 has shown to be difficult to model with both Puma and Swanepoel, whose n-values appear as two equally large values of 3.2 that stand out from the other results. To indicate the unreliable result, the overlapping square and circle at 7.4% Fe have a pink marker edge.

different structure of the films deposited from FeS and ZnS, revealed by the TEM images. Another possible explanation for the deviation is that Fe from the FeS source may not have been successfully substituted into the ZnS lattice, but remained in the double bond to S, or forming FeS_2. A presence of FeS_2 was suggested in sample EFES2Quv7.4, deposited from FeS and ZnS, looking at RBS results obtained from Prof. Ursula Gibson. This could also explain why this sample is seen to be difficult to model.

The difficulties of modeling Sample EFES2Quv7.4 using Puma and Swanepoel are manifested by two equally large n-values of 3.2 that stand out from the other results. In addition to the suggested presence of FeS_2, the large value could be attributed to a significant amount of impurities in the film, supported by the large Urbach energy of the sample observed in figure 5.48 and 5.62, based on the raw transmission data and the Swanepoel model, respectively.

The difference between the samples made from the two different iron sources becomes even more apparent studying the values of κ. The values of the imaginary part of the refractive index of the samples in the "FeS + ZnS" series are significantly larger, and are hence assigned a separate plot, shown in figure 5.51. An overview of κ at 1000nm wavelength of the films in the "Fe + ZnS" and "Fe + ZnS in UHV" series are given in

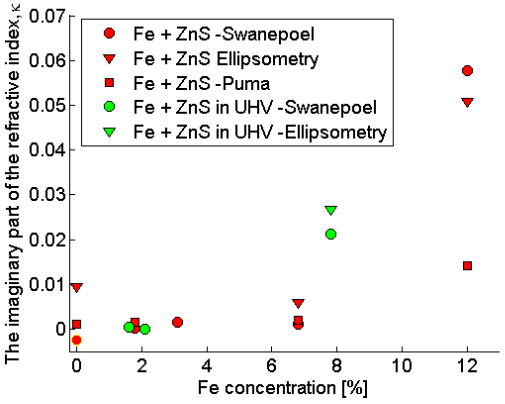

FIGURE 5.50: An overview of the imaginary part of the refractive index κ at a wavelength of 1000nm. The values are retrieved by the Swanepoel model, ellipsometry and the Puma model, labeled with a circle, triangle and square, respectively. The films whose κ-values are presented in this figure are made of Fe and ZnS source, using PVD and molecular beam deposition technique, shown in red and green colour, respectively.

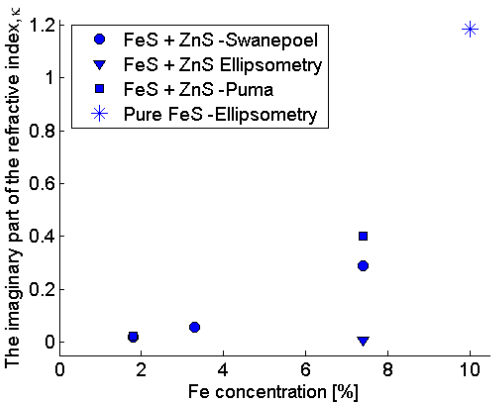

FIGURE 5.51: The imaginary part of the refractive index κ at a 1000nm wavelength of films made of FeS and ZnS. The values are retrieved by the Swanepoel model, ellipsometry and the Puma model, labeled with a circle, triangle and a square, respectively. κ of the pure FeS source determined by ellipsometry is also included, represented by the blue star in the upper right corner. This point is independent of the x-axis.

figure 5.50. Unlike the case of the real part of the refractive index, κ seems to be dependent on the Fe concentration of the films in all series. The observation of a larger value of κ for high Fe concentrated films confirms the resulting absorption coefficients from the transmission measurements given by figure 5.28, where a clear trend of increasing α with respect to Fe concentration is observed. The increase in the absorption could be caused by defects being introduced to the films by the doping, since the absorption increases at all wavelengths, as well as it could be attributed a presence of Fe=S or FeS_2 according to the discussion above.

5.3.3.4 The complex refractive index in the 200nm-800nm wavelength range

In the studies of the optical band gap of the films, the low wavelength range is investingated, as the absorption edge is observed at wavelengths around 350nm, seen in section 5.3.1. A comparison of the refractive indices in the low wavelength region of strong absorption retrieved from the Swanepoel model and ellipsometry of sample DZnS6Quv, BF5Quv6.8 and BF2Quv12 are shown in figure 5.52 and 5.53. In the respective figures, the complex refractive index is presented in terms of n and κ, where the latter is represented by the absoption coefficient α.

The resulting values of κ presented as α in figure 5.53, show that there is a good agreement between the models. The trend of increasing value of α at 1000nm wavelength with respect to Fe concentration is seen to be valid also at low wavelengths.

Considering the n-values, seen in figure 5.52, the estimations retrieved by the two mod-

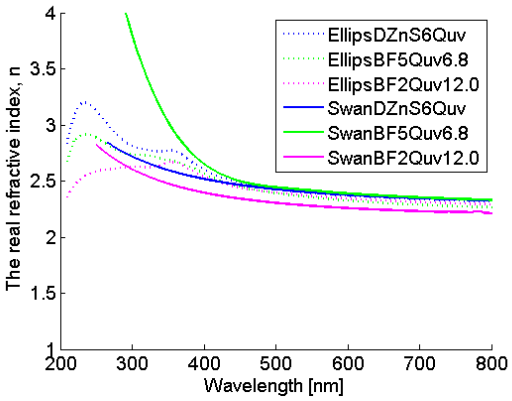

FIGURE 5.52: The real part of the refractive index n determined by ellipsometry and the Swanepoel method for the samples DZnS6Quv, BF5Quv6.8 and BF2Quv12, indicated by blue, green and pink colour, respectively. The n-values retrieved from ellipsometry are presented with dotted lines, while the solid lines represent the n-values obtained by Swanepoel.

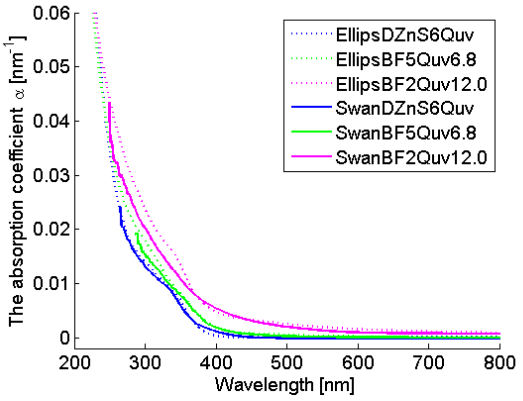

FIGURE 5.53: The absorption coefficient α, representing the imaginary part of the refractive index κ, determined by ellipsometry and the Swanepoel method for the different samples DZnS6Quv, BF5Quv6.8 and BF2Quv12, indicated by blue, green and pink colour, respectively. The α-values retrieved from ellipsometry are presented with dotted lines, while the solid lines represent the α-values obtained by Swanepoel.

els are observed to be in closer agreement at larger wavelengths, and for the pure ZnS film in sample DZnS6Quv, the values of n at wavelengths larger than 450nm estimated by the models are almost identical. At the lower wavelengths, however, the deviation becomes more apparent. The deviation occurs as a consequence of Swanepoel having problems with the estimation of n when the values of the transmission become too small, as discussed in section 5.3.2.5. For this reason, it is hence believed that the ellipsometry model gives the best description of the films at low wavelengths.

As mentioned in the previous paragraph and discussed in detail in section 5.3.2.5, the Swanepoel model shows a weakness at lower wavelengths, in terms of indeterminate values of n. In order to remove the noise occuring in this region, two different techniques were applied to modify n in the modeled samples. The first method involves using the smoothing function in Matlab©, whose value in a given datapoint represents the average

of the original value of the datapoint in addition to the original values of a specified number of neighbouring datapoints. As an illustrative example, the result of applying this smoothing function for sample DZnS6Quv is shown by the blue solid curve in figure 5.54.

The result of the second modification method involving using an extrapolated value of n at low wavelengths is shown in the same figure, indicated by the green curve. The extrapolation is based on the n-values corresponding to wavelengths in the range above 450nm. The back calculated transmission spectra with corresponding envelope curves in which the smoothing- and extrapolated version of n are applied, are presented in figure 5.55 and 5.56, respectively, in addition to the physical measurement of the transmission. According to these figures, n resulting from the smoothing function gives the best model fit. However, as seen in figure 5.54, these smoothing values of n for the pure ZnS sample have an oscillating behaviour at low wavelengths, which is in disagreement with the theoretical real refractive index of this material. The suggestion of the oscillating n being unphysical is strengthened by looking at the ellipsometry results in figure 5.52, where n is steadily increasing at low wavelengths. Based on these observations, the extrapolated version of n is applied for all samples, as this is considered to represent a physical value.

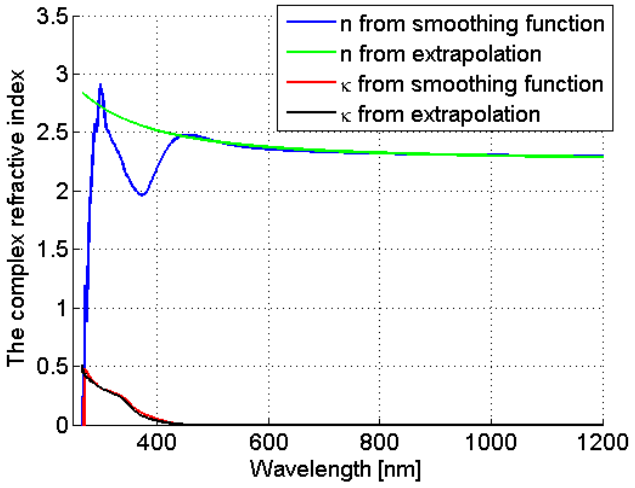

FIGURE 5.54: The real- and imaginary part of the refractive index calculated by the Swanepoel model. n and κ given by the blue and red curve, respectively, represent a smoothed version of the original Swanepoel output. n and κ represented by the green and black curves, respectively, are the results of using an extrapolated value of n and κ at low wavelengths.

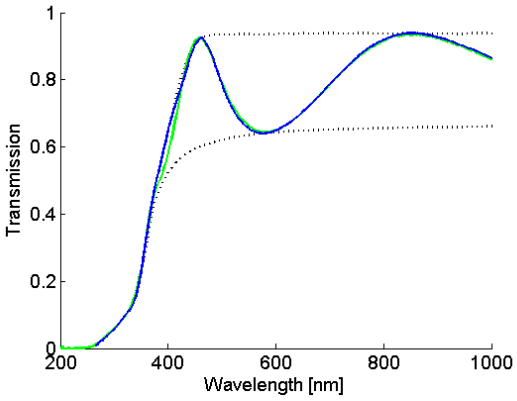

FIGURE 5.55: The figure shows the transmission spectrum with corresponding envelope curves recalculated with a smoothed version of n retrieved by the Swanepoel model, in blue and black colour, respectively. This illustration is based on data from sample DZnS6Quv of pure ZnS, whose measured transmission spectrum is presented by the green curve.

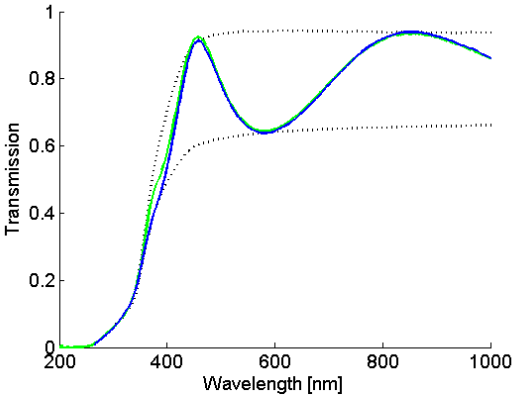

FIGURE 5.56: The figure shows the transmission spectrum with corresponding envelope curves recalculated from n by the Swanepoel model, in blue and black colour, respectively. In the recalculations an extrapolated value of n has been applied at low wavelengths. This illustration is based on data from sample DZnS6Quv of pure ZnS, whose measured transmission spectrum is presented by the green curve.

5.3.3.5 Band gap determination by the models

From the imaginary part of the refractive index κ retrieved from the models, the absorption coefficients are calculated and used in Tauc plots in order to determine the band gaps of the films. Figure 5.57 and 5.58 show the direct- and indirect Tauc plots based on the absorption coefficients obtained from the transmission spectrum of sample EKMBEQuv7.8, respectively, in addition to Tauc plots based on κ estimated by ellipsometry and the Swanepoel model applied to the same sample. Results from Puma are not included as this method is considered to be inconvenient for the data in this project for the reasons followed by the discussion in section 5.3.2.2.

Figure 5.58 in particular, illustrates the differences between the three techniques and how these complement each other. The simplicity of the band gap determination based on the transmission spectrum becomes apparent at low energies. In this energy range, the Tauc plot contains fringes and has higher values than that of the ellipsometry and the Swanepoel metod, occuring as a consequence of α being overestimated by neglecting the reflection. For the indirect band gap the error has a typical value of 0.25eV, while the error is almost neglectible for the direct band gap yielding 0.004 eV. By determining the complex refractive index, both the transmission and the reflection are accounted

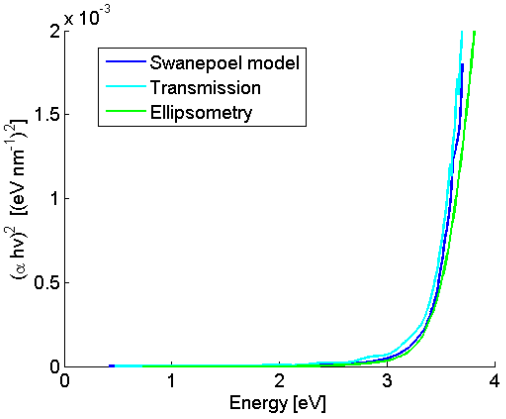

FIGURE 5.57: The figure shows the direct Tauc plots based on the absorption coefficient of sample EKMBEQuv7.8 calculated by the Swanepoel model, the raw transmission measurements and ellipsometry given by a dark blue, light blue and green curve, respectively.

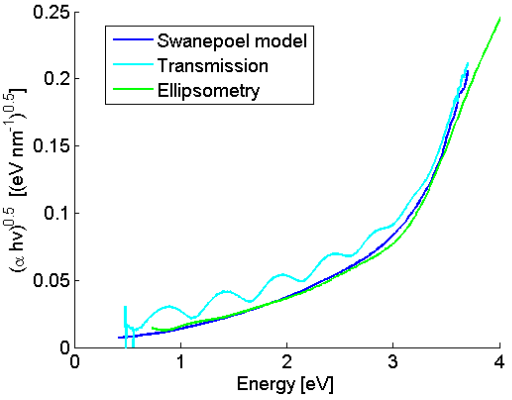

FIGURE 5.58: The figure shows the indirect Tauc plots based on the absorption coefficient of sample EKMBEQuv7.8 calculated by the Swanepoel model, the raw transmission measurements and ellipsometry given by a dark blue, light blue and green curve, respectively

for in ellipsometry and in the Swanepoel model, and these models hence give the best description of the films at low energies where the reflection is significant.

Moving to high energies where no reflection occurs, the relation $I = I_0 e^{-\alpha \cdot d}$ constituting the basis of the Tauc plot from the raw transmission is considered to be valid, as 2% transmission would lead to a small error of 5% in α at wavelengths of approximately 350 nm. In the same high energy range, the Swanepoel model is seen to have difficulties, as an extrapolation of n is required for this region, according to the description of the model in section 5.3.2.5. This favours the ellipsometry and the transmission method in the high energy range. In the mid-range, where the sudden drop in transmitted intensity occurs at the absorption edge, all three methods are considered to be applicable. As seen by comparing the Tauc plots in figure 5.57 and 5.58, the curves obtained by the different techniques coincide in this mid region. This implies that that all three methods would lead to band gaps of similar magnitude, which is the case of most samples as seen in figure 5.59 and 5.60, where an overview of the direct- and indirect band gaps of the nine selected films are presented, respectively.

In these overviews, direct- and indirect band gaps determined based on ellipsometry, Puma and Swanepoel are presented in addition to the band gaps resulting from the raw transmission. Puma is considered not to be an appropriate method as seen in section 5.3.2.2, but the results from this model are included in the overview tables as a comparison to the other techniques. The direct band gaps resulting from the models seen

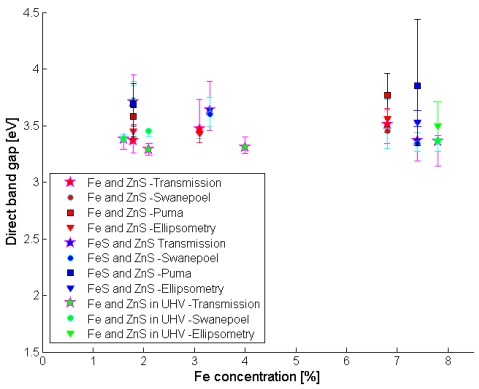

FIGURE 5.59: An overview of the direct band gaps of nine selected films estimated by the transmission, the Swanepoel model, the Puma model and ellipsometry.

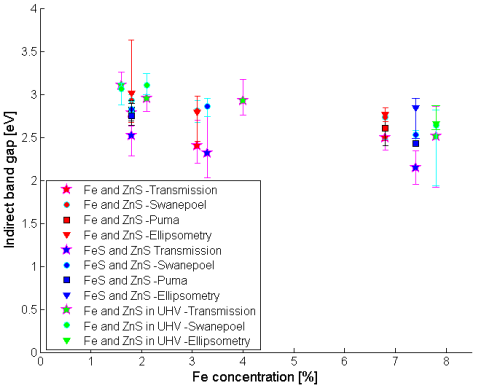

FIGURE 5.60: An overview of the indirect band gaps of nine selected films estimated by the transmission, the Swanepoel model, the Puma model and ellipsometry.

in figure 5.59, are observed to be quite stable within the errorbars with respect to Fe content, in agreement with the trend observed from the transmission results presented in section 5.3.3.1. The Puma result for sample EFES2Quv7.4 indicated by the blue square at Fe concentration of 7.4%, stands out from the other results having a larger direct band gap value. The value is considered to be questionable as the model did not show a good fit for this sample.

From the overview of the indirect band gaps shown in figure 5.60, a trend of increasing values of the indirect band gap with respect to Fe concentration is observed for all four analysing techniques. The indirect band gaps resulting from the transmission, are seen to have overall smaller values than that of the other models, in accordance with the error of approximately 0.25 eV, arising from neglecting the reflection.

Urbach plots based on α resulting from Swanepoel are presented in figure 5.61, and are observed to be in correspondence with the Urbach plots based on the analysis of the transmission, given by figure 5.47.

The good agreement between the Swanepoel- and the transmission method shown by the Urbach plots is transmitted to the corresponding Urbach energies, E_U. From figure 5.62, where E_U-values calculated from the Swanepoel model are presented, a trend of increasing E_U for higher Fe concentrated films is observed, similar to that of the Urbach energies based on the analysis of the raw transmission shown in figure 5.48. Hence, the Swanepoel model confirms the results obtained by the transmission method, which provides a larger width of the Urbach tail with respect to Fe concentration. As discussed

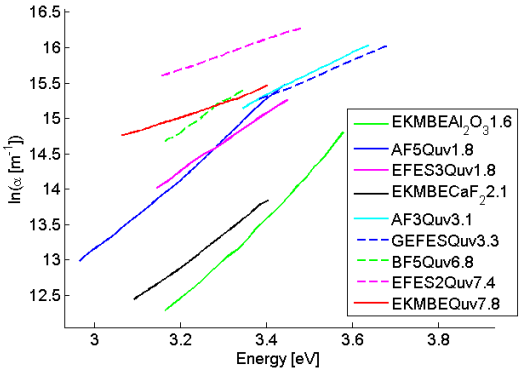

FIGURE 5.61: Urbach plots of the nine selected samples based on the absorption coefficents calculated from κ estimated by the Swanepoel model.

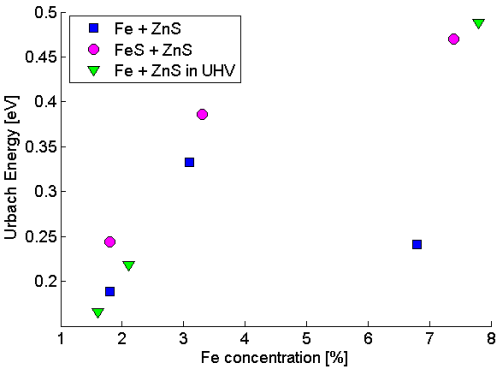

FIGURE 5.62: The Urbach energies E_U of the nine selected samples from the different categories "Fe + ZnS", "FeS + ZnS" and "Fe + ZnS in UHV" based on the Swanepoel model. E_U corresponds to the inverse slopes of the Urbach plots of the same samples, presented in figure 5.61.

in section 5.3.3.1 this would in turn imply defects being positioned deeper into the band gap when the doping level is increased.

5.3.4 Optical characterization - NIR

In this section the results of the absorption study of a selection of films deposited on substrates transparent in the NIR are presented. For the thinner films made by PVD no particular absorption features were seen, while an absorption dip in the NIR was observed for the thicker samples made in molecular beam deposition, corresponding to absorption of Fe^{2+} .

5.3.4.1 FTIR revealing Fe^{2+} absorption

The transmission spectrum of sample EKMBECaF$_2$1.7 obtained from combined FTIR and spectrophotometer measurements shown in figure 5.63, reveals a pronounced absorption in the near infrared, where there is an absorption band at 0.46 eV attributed to Fe^{2+} [24]. This confirms the results from XPS in section 5.2.4, stating that Fe is substituting Zn creating an Fe-S bond. The transmission drop in the near infrared also becomes apparent in the imaginary part of the refractive index κ estimated by the Swanepoel model, presented in section 5.3.2.5, where a prominent peak is observed at similar energies.

The observation of the well isolated Fe^{2+} absorption in the 1.7% Fe film made under UHV conditions, is suggesting that such films may be useful as saturable absorbers or mid-infrared waveguide lasers [24].

Similar absorption was observed for several of the thicker samples made under UHV;

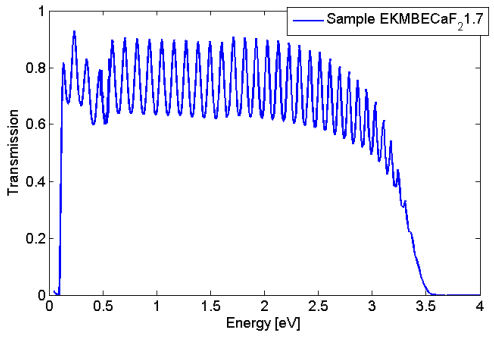

FIGURE 5.63: The transmission spectrum of sample EKMBECaF$_2$1.7, obtained from combined FTIR and spectrophotometer measurements.

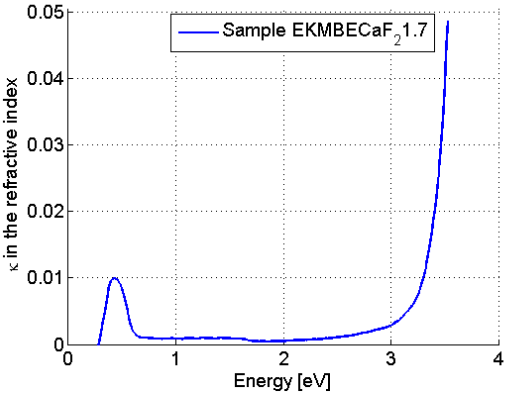

FIGURE 5.64: The imaginary part of the refractive index κ estimated by the Swanepoel model for sample EKMBECaF$_2$1.7 .

EKMBECaF$_2$4.0,EKMBECaF$_2$2.1 and EKMBEAl$_2$O$_3$1.9, but was not seen in the films made with the PVD technique. It is suggested that the small film thickness of the latter films, leading to a low fringe density of the transmission spectrum in the mid infrared region, would make it difficult to observe such an absorption dip.

Chapter 6

Conclusion and future work

6.1 Conclusion

Films of iron doped ZnS were deposited by PVD. Iron sources consisted of either elemental Fe or FeS. Crystal monitors were used for thickness estimations and to control the dopant concentrations throughout the deposition.

As desired, EDS and profilometer measurements confirmed a variation in the composition and thickness of the films, respectively. XPS revealed that Fe^{2+} had successfully substituted Zn^{2+} atoms, incorporating Fe in the ZnS structure. XRD and TEM indicated that the incorporation of Fe stabilizes small grain growth in the films, and for the thicker films made under UHV adding Fe to the ZnS was seen to reduce stress. The latter technique confirmed a hexagonal structure of the films.

The optical properties of the films were derived from transmission measurements using different modeling techniques to retrieve values of the complex refractive index. Backcalculating the transmission from the estimated n and κ values confirmed the model validity for most films, and ellipsometry confirmed the results from the Swanpoel model. An increase in absorption with increasing Fe content was revealed, along with a broadening of the Urbach tail (which seems to have been perceived as an indirect band gap by others). The direct band gap was observed to be unaffected by the doping level, with an estimated value of 3.5eV. This is a bit lower than reported values for bulk ZnS, and is attributed to nano-crystalline grains found in the films. As in the case of the direct band gap, the different Fe concentrations did not seem to cause a significant change in the real part of the refractive index, whose average value of 2.29 at 1000nm wavelength is as expected for a hexagonal ZnS structure.

Annealing Fe:ZnS films in sulfur atmosphere, or codeposition from FeS resulted in films with higher absorption and inhomogeneous indices of refraction. The superior properties of Fe:ZnS films from an elemental source and the absence of absorption in those films from Fe states other than Fe^{2+} suggests that Fe bonds preferentially to S in the ZnS lattice. When films were annealed, or FeS was used as a source, Fe associated with excess sulfur, forming FeS_2 or Fe=S and thus was not substituted successfully into the ZnS lattice.

Since engineering of the band gap could not be obtained for doping levels up to 12% used in this project, it is unlikely that the Fe:ZnS films could be suitable for IBSC. While the films deposited in the PVD system were too thin to observe absorption in the mid-IR conclusively, a well isolated Fe^{2+} absorption at 2.7μm was observed for thick films made under UHV conditions, suggesting Fe:ZnS thin films being a useful material for saturable absorbers or mid-IR waveguide lasers.

6.2 Future work

Refinement in the optical characterization of the Fe:ZnS thin films involves several things. The Swanepoel modeling was shown to be a satisfactory method for retrieving estimated values of optical constants of thin films. To improve the model, the current constant value of the refractive index of the substrate should be replaced with n expressed as a function of wavelength. In this way, a more accurate value of n and κ of the film could be obtained in the low wavelength region where a large increase in n of the substrate appears.

Since the EDS concentration results for the thin films seemed to be affected by the substrate, it would be convenient to investigate the composition of the films with additional techniques to confirm the substrate dependency in the EDS concentrations. Rutherford backscattering spectrometry (RBS) is considered to be a preferrable method for this purpose, as the measurements are quantitative and unaffected by chemical effects.

In addition, XPS studies could be performed to determine the details of the substitutional incorporation of Fe into the ZnS matrix for various concentrations of Fe.

Although testing of lasing and saturable absorbance are not within the scope of the project, non-linear optical characterization of Fe:ZnS thin films holds the promise of having a significant technological impact.

Appendix A

Overview tables

In this appendix a copy of the tables shown in section 5.1 containing information about the deposition rates of the Fe/FeS source and the ZnS source is given by table A.1 while the overview of the thickness and composition of the films is found in table A.2. In addition, a summary of the band gaps estimated by the different methods described in section 5.3.2 are presented in table A.3. These overview tables can be removed, and might be convenient to look at when reading through the results.

TABLE A.1: The deposition rates of the Fe/FeS source and ZnS source, in addition to the base pressure before- and during the different deposition runs.

Deposition run	Base pressure after pump down [torr]	Base pressure during deposition [torr]	ZnS rate [Å/s]	Fe rate [Å/s]	FeS rate [Å/s]
A	3.3e-6	3.1e-5	8.5	0.4	-
B	2.8e-6	2.6e-5	8.2	1.3	-
C	3.6e-6	2.6e-5	4.1	0.5	-
D	3.9e-6	2.6e-5	7.9	-	-
E	4.1e-6	2.7e-5	3.9	-	0.5
F	4.5e-6	2.5e-5	-	-	0.5
G	4.2e-6	2.8e-5	5.6	-	0.6
H	3.3e-6	5.1e-5	2.5	-	0.6
I	4.0e-6	2.8e-5	4.4	-	0.3

TABLE A.2: The thicknesses and composition of all the films. *The concentration is concider to be questionable due to a S/(Fe+Zn) ratio deviating more than 0,3 from unity

Sample	Substrate	Thicknesses (+/- 50) [Å]	Fe/(Fe+Zn+S) [%]	S/(Fe+Zn) [%]
AF1Si22.1	Silicon	697	22,1*	0,46*
AF2Si4.2	Silicon	1613	4,2	0,75
AF2Quv4.3	Fused silica uv	1784	4,3	0,95
AFA2Quv4.3	Fused silica uv	1784	4,3*	0,67*
AF3Si3.0	Silicon	2381	3,0	0,75
AF3Quv3.1	Fused silica uv	2555	3,1	0,90
AFA3Quv3.1	Fused silica uv	2555	3,1*	0,67*
AF4Si2.3	Silicon	2873	2,3	0,78
AF4Quv2.4	Fused silica uv	3063	2,4	0,99
AFA4Quv2.4	Fused silica uv	3063	2,4*	0,67*
AF5Si1.9	Silicon	3156	1,9	0,77
AF5Quv1.8	Fused silica uv	3375	1,8	1,01
AFA5Quv1.8	Fused silica uv	3375	1,8*	0,68*
AF6Si1.5	Silicon	3188	1,5	0,78
AF6Quv1.5	Fused silica uv	3387	1,5	0,95
AFA6Quv1.5	Fused silica uv	3387	1,5*	0,68*
AF6Qir1.4	Quartz ir	3117	1,4	1,19
BF1Si17.4	Silicon	623	17,4	0,50
BF1Quv11.8	Fused silica uv	605	11,8	1,02
BFA1Quv11.8	Fused silica uv	605	11,8	0,95
BF2Si13.5	Silicon	1167	13,5	0,73
BF2Quv12.0	Fused silica uv	1258	12,0	1,09
BFA2Quv12.0	Fused silica uv	1258	12,0	1,07
BF3Si11.0	Silicon	1557	11,0	0,73
BF3Quv11.1	Fused silica uv	1667	11,1*	1,42*
BFA3Quv11.1	Fused silica uv	1667	11,1	0,77
BF4Si8.3	Silicon	2017	8,3	0,72
BF4Quv8.2	Fused silica uv	2169	8,2*	1,45*
BFA4Quv8.2	Fused silica uv	2169	8,2	0,73
BF4Qir8.4	Quartz ir	1552	8,4	0,96
BF5Si6.5	Silicon	1828	6,5	0,74
BF5Quv6.8	Fused silica uv	2133	6,8	1,08

Continued on next page

Table A.2 – continued from previous page

Sample	Substrate	Thicknesses (+/- 50) [Å]	Fe/(Fe+Zn+S) [%]	S/(Fe+Zn) [%]
BFA5Quv6.8	Fused silica uv	2133	6,8	0,70
BF6Si4.7	Silicon	2145	4,7	0,75
BF6Quv5.0	Fused silica uv	2156	5,0	0,98
BFA6Quv5.0	Fused silica uv	2156	5,0	0,71
BF6Qir4.8	Quartz ir	2484	4,8*	1,59*
CF3Grid12.2	TEM grid	440	12,2*	0,63*
CF5Grid6.5	TEM grid	733	6,5	0,73
DZnS5Si	Silicon	1736	0,0	0,78
DZnS5Quv	Fused silica uv	1956	0,0	1,05
DZnS6Si	Silicon	1731	0,0	0,78
DZnS6Quv	Fused silica uv	1996	0,0	1,30
DZnS6Qir	Quartz ir	1717	0,0	1,69*
EFES1Si8.3	Silicon	1601	8,3	0,97
EFES1Quv7.7	Fused silica uv	1809	7,7	0,82
EFES2Si7.2	Silicon	2139	7,2	0,91
EFES2Quv7.4	Fused silica uv	2320	7,4	0,84
EFES2Qir7.0	Quartz ir	1988	7,0	0,70
EFES3Si1.9	Silicon	2316	1,9	0,79
EFES3Quv1.8	Fused silica uv	2297	1,8*	0,62*
EFES3Qir1.8	Quartz ir	2031	1,8*	0,61*
FPFES2Si	Silicon	308	50,0	50,0
FPFES2Quv	Fused silica uv	367	50,0	50,0
FPFES3Si	Silicon	367	50,0	50,0
FPFES3Quv	Fused silica uv	385	50,0	50,0
GFES1Si3.5	Silicon	1650	3,5	1,05
GFES1Quv3.3	Fused silica uv	1643	3,3	0,84
GFES2Si1.5	Silicon	2164	1,5	0,85
GFES2Quv1.5	Fused silica uv	2222	1,5	0,76
GFES3Si1.0	Silicon	2553	1,0	0,82
GFES3Quv1.1	Fused silica uv	2672	1,1	0,76
HFES2Quv5.1	Fused silica uv	1816	5,1*	1,57*
IFES3Grid3.0	TEM grid	200	3,0	1,22
EKMBESi1.7	Silicon	23750	1,7	0,85
EKMBESi1.9	Silicon	24500	1,9	0,84

Continued on next page

Table A.2 – continued from previous page

Sample	Substrate	Thicknesses (+/- 50) [Å]	Fe/(Fe+Zn+S) [%]	S/(Fe+Zn) [%]
EKMBE$CaF_2$1.7	CaF_2	25050	1,7	0,85
EKMBE$Al_2O_3$1.6	Sapphire	22250	1,6	0,85
EKMBE$Al_2O_3$7.1	Sapphire	4867	7,1	0,72
EKMBESi7.5	Silicon	4900	7,5	0,74
EKMBEQuv7.8	Fused silica uv	4850	7,8	0,73
EKMBEQir7.0	Quartz ir	5075	7,0	0,74
EKMBE$CaF_2$2.1	CaF_2	34750	2,1*	1,31*
EKMBE$Al_2O_3$1.9	Sapphire	36625	1,9*	2,29*
EKMBEPZnSAl_2O_3	Sapphire	1 400	0,0	-
EKMBE$CaF_2$4.0	CaF_2	4400	4,0	-

Table A.3: An overview of the direct- and indirect band gaps of the films estimated directly from the transmission and by applying modeling techniques involving the Swanepoel method, ellipsometry and the Puma software. The Fe content of the films are given by the last digits in the sample name, and refers to the atomic fraction Fe/(Fe+Zn+S). *Questionable model results, **Model did not apply.

Sample	Eg transmission (dir,ind)[eV]	Eg Swanepoel (dir,ind)[eV]	Eg Ellipsometry (dir,ind)[eV]	Eg Puma (dir,ind)[eV]
AF1Si22.1				
AF2Si4.2				
AF2Quv4.3	3.51, 2.29			
AFA2Quv4.3	3.58, 2.27		3.52, 2.65	
AF3Si3.0				
AF3Quv3.1	3.47, 2.42	3.39, 2.77		
AFA3Quv3.1	3.55, 2.82			
AF4Si2.3				
AF4Quv2.4	3.38, 2.66			
AFA4Quv2.4	3.52, 2.85			
AF5Si1.9				
AF5Quv1.8	3.37, 2.78	3.72, 2.93		3.56, 2.82
AFA5Quv1.8	3.50, 2.75	3.47, 3.03		3.68, 2.75
AF6Si1.5				

Continued on next page

Table A.3 – continued from previous page

Sample	Eg transmission (dir,ind)[eV]	Eg Swanepoel (dir,ind)[eV]	Eg Ellipsometry (dir,ind)[eV]	Eg Puma (dir,ind)[eV]
AF6Quv1.5	3.40, 2.82			
AFA6Quv1.5	3.50, 2.75			
AF6Qir1.4	3.38, 2.73			
BF1Si17.4				
BF1Quv11.8	3.60, 2.03			
BFA1Quv11.8	3.37, 1.47			
BF2Si13.5				
BF2Quv12.0	3.66, 1.99	3.66, 2.21	3.32, 2.39	3.71, 2.41
BFA2Quv12.0	3.35, 0.53	**	2.73, 1.58	2.21, 0.45*
BF3Si11.0				
BF3Quv11.1	3.61, 2.26			
BFA3Quv11.1	3.44, 1.43			
BF4Si8.3				
BF4Quv8.2	3.55, 2.28			
BFA4Quv8.2	3.46, 2.34			
BF4Qir8.4				
BF5Si6.5				
BF5Quv6.8	3.51, 2.50	3.72, 2.73	3.56, 2.77	3.77, 2.61
BFA5Quv6.8	3.52, 2.27	3.55, 2.91	3.53, 2.87	3.67, 2.77*
BF6Si4.7				
BF6Quv5.0	3.47, 2.46			
BFA6Quv5.0	3.53, 2.41			
BF6Qir4.8				
CF3Grid12.2				
CF5Grid6.5				
DZnS5Si				
DZnS5Quv	3.72, 2.60			
DZnS6Si				
DZnS6Quv	3.76, 2.64	3.73, 2.65	3.70, 2.95	3.81, 2.75
DZnS6Qir	3.71, 2.67			
EFES1Si8.3				
EFES1Quv7.7	3.57, 1.7			
EFES2Si7.2				
EFES2Quv7.4	3.37, 2.15	3.34, 2.53	3.53, 2.84	3.36, 2.66*

Continued on next page

Table A.3 – continued from previous page

Sample	Eg transmission (dir,ind)[eV]	Eg Swanepoel (dir,ind)[eV]	Eg Ellipsometry (dir,ind)[eV]	Eg Puma (dir,ind)[eV]
EFES2Qir7.0	3.42, 2.11			
EFES3Si1.9				
EFES3Quv1.8	3.71, 2.41	3.71, 2.83		3.70, 2.75
EFES3Qir1.8	3.77, 2.52			
FPFES2Si				
FPFES2Quv				
FPFES3Si				
FPFES3Quv				
GFES1Si3.5				
GFES1Quv3.3	3.64, 2.32			
GFES2Si1.5				
GFES2Quv1.5	3.49, 2.64			
GFES3Si1.0				
GFES3Quv1.1	3.48, 2.76			
HFES2Quv5.1	3.68, 2.44			
IFES3Grid3.0				
EKMBESi1.7				
EKMBESi1.9				
EKMBE$CaF_2$1.7	3.40, 3.16			
EKMBE$Al_2O_3$1.6	3.38, 3.11	3.50, 3.20		
EKMBE$Al_2O_3$7.1	3.31, 2.52			
EKMBESi2.1				
EKMBEQuv7.8	3.36, 2.51	3.36, 2.64	3.50, 2.66	
EKMBEQir7.0	3.34, 2.55			
EKMBE$CaF_2$2.1	3.29, 2.95	3.45, 3.11		
EKMBE$Al_2O_3$1.9	3.37, 3.00			
EKMBEPZnSAl_2O_3	3.47, 3.10			
EKMBE$CaF_2$4.0	3.01, 2.93			

Appendix B

Transmission spectra

In this appendix the transmission spectra of all the films deposited on transparent substrates are presented. The spectra are plotted both with respect to wavelength and with respect to energy.

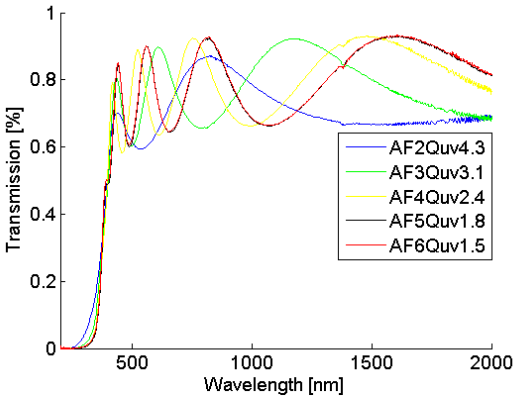

FIGURE B.1: The transmission spectra of the films made from Fe and ZnS in deposition run A, with respect to wavelength.

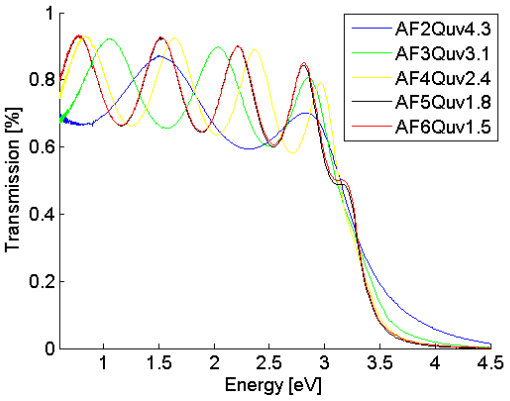

FIGURE B.2: The transmission spectra of the films made from Fe and ZnS in deposition run A, with respect to energy.

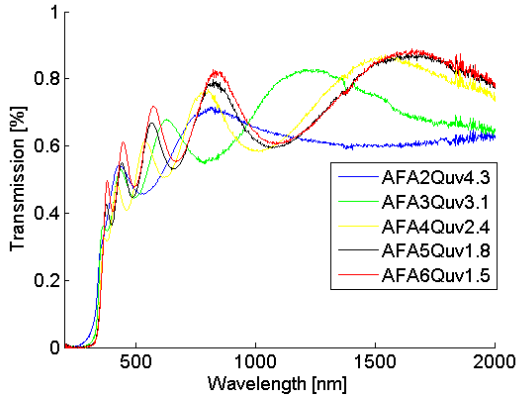

FIGURE B.3: The transmission spectra of the annealed version of the films made from Fe and ZnS in deposition run A, with respect to wavelength.

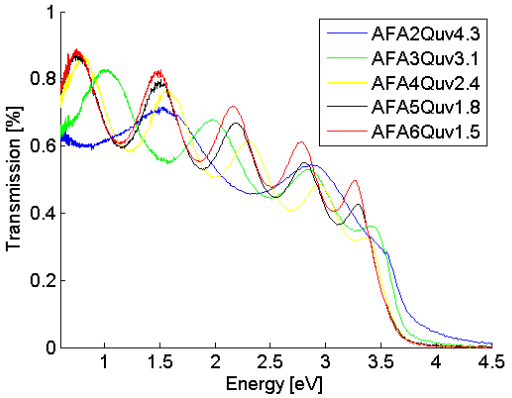

FIGURE B.4: The transmission spectra of the annealed version of the films made from Fe and ZnS in deposition run A, with respect to energy.

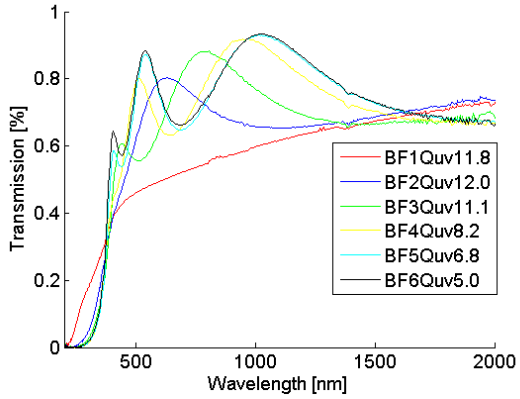

FIGURE B.5: The transmission spectra of the films made from Fe and ZnS in deposition run B, with respect to wavelength.

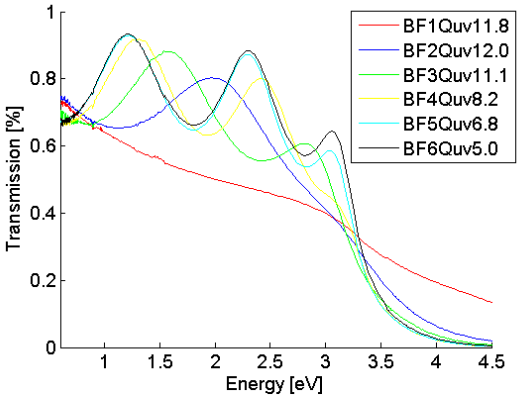

FIGURE B.6: The transmission spectra of the films made from Fe and ZnS in deposition run B, with respect to energy.

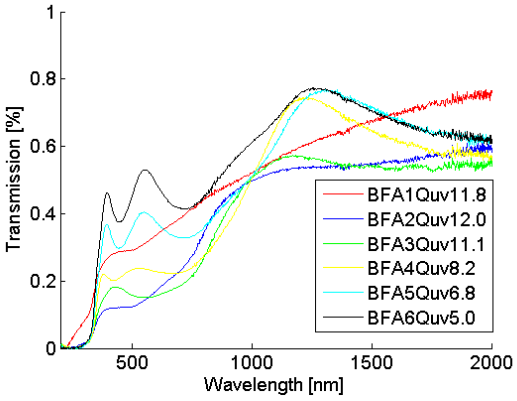

FIGURE B.7: The transmission spectra of the annealed version of the films made from Fe and ZnS in deposition run B, with respect to wavelength.

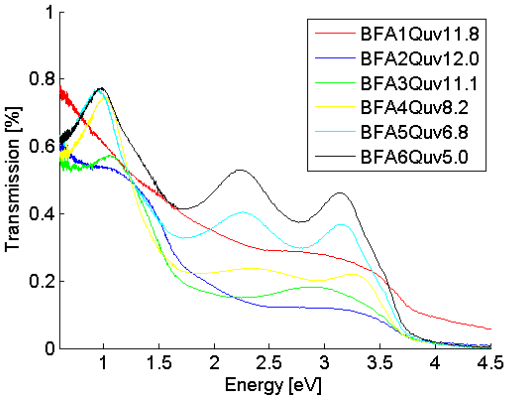

FIGURE B.8: The transmission spectra of the annealed version of the films made from Fe and ZnS in deposition run B, with respect to energy.

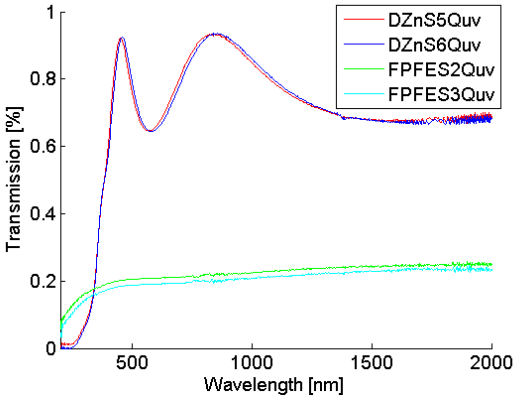

FIGURE B.9: The transmission spectra of pure ZnS films and pure FeS films, with respect to wavelength.

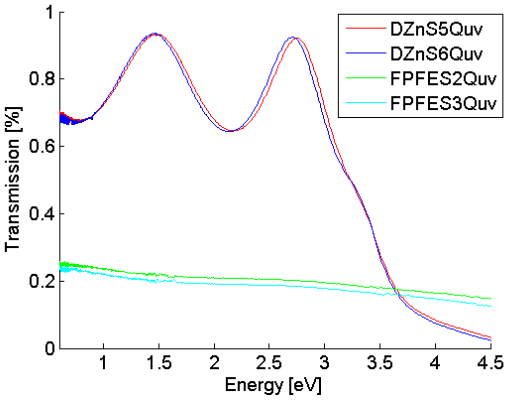

FIGURE B.10: The transmission spectra of pure ZnS films and pure FeS films, with respect to energy.

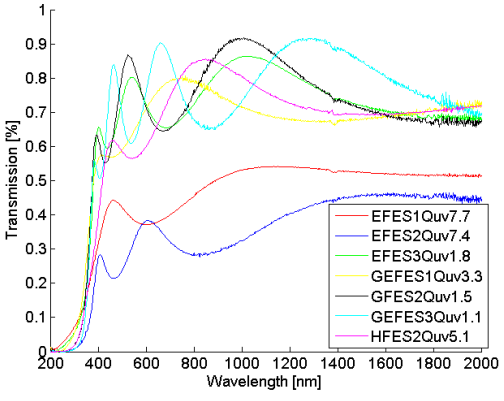

FIGURE B.11: The transmission spectra of the films made from FeS and ZnS, with respect to wavelength.

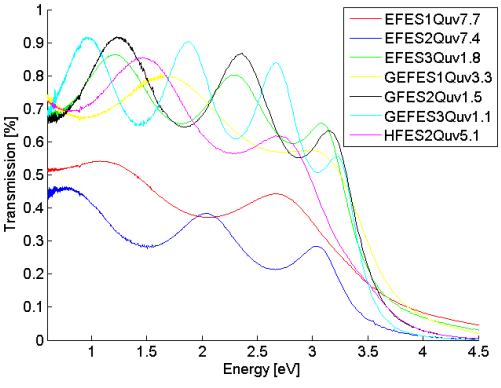

FIGURE B.12: The transmission spectra of the films made from FeS and ZnS, with respect to energy.

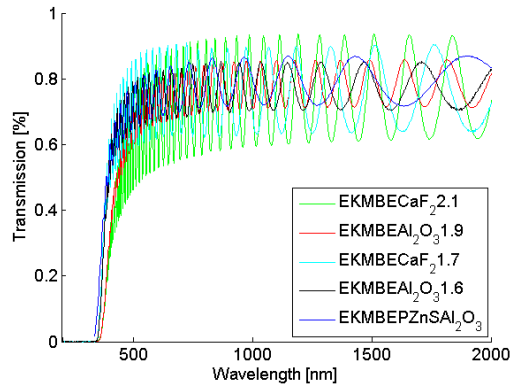

FIGURE B.13: The transmission spectra of films made from Fe and ZnS under UHV conditions, with respect to wavelength.

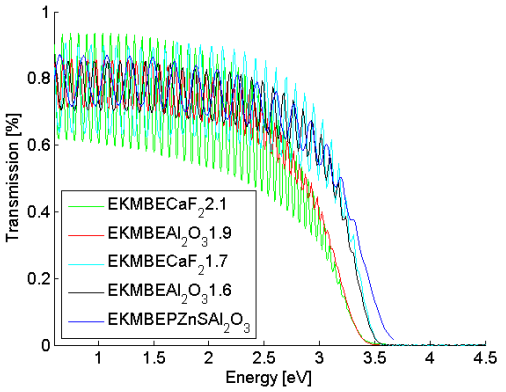

FIGURE B.14: The transmission spectra of films made from Fe and ZnS under UHV conditions, with respect to energy.

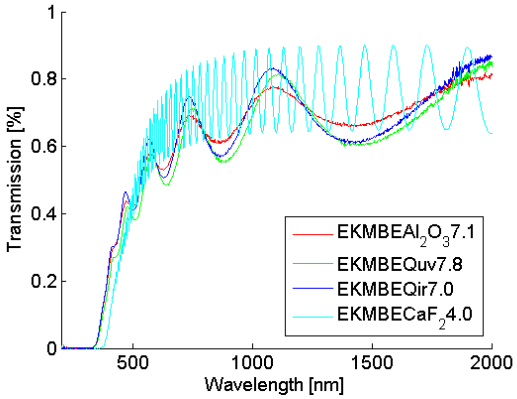

FIGURE B.15: The transmission spectra of films made from Fe and ZnS under UHV conditions, with respect to wavelength.

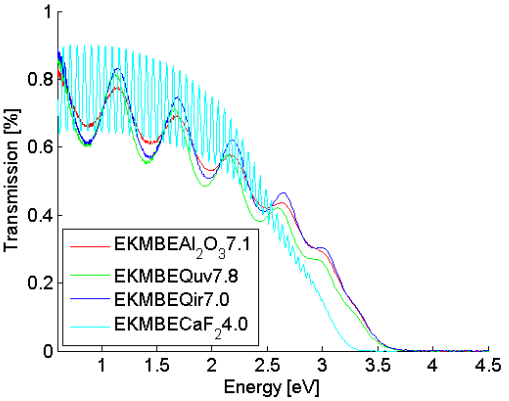

FIGURE B.16: The transmission spectra of films made from Fe and ZnS under UHV conditions, with respect to energy.

Appendix C

Results of the annealed films

Since the behaviour of the annealed films were not as expected, showing more absorption and nonuniform refractive indices, seen in section 5.3.1.3, the results of these samples are presented separately in this appendix.

The direct- and indirect band gaps of the films deposited from Fe and ZnS before and after annealing are presented in figure C.1 and C.2, respectively. Direct- and indirect Tauc plots based on the absorption calculated from raw transmission measurements were used in the estimation. A less abrupt drop in transmitted intensity is observed in the films after annealing compared to the films before the annealing, by studying figure 5.19 and 5.23 in section 5.3.1, showing the transmission spectra of the films before- and after annealing, respectively. The more gradual loss in transmission is suggested to cause significantly larger errorbars in the indirect band gap of the annealed films compared to that of the films not being exposed to annealing.

For the same reasons that cause large error bars in the indirect band gap estimations, the modeling of the annealed films with Fe consentrations larger than 6% has shown to be difficult. An overview of the real part of the refractive index n and the absorption coefficient α, calculated from the imaginary part of the refractive index κ at 1000nm wavelength, are presented in figure C.3 and C.4, respectively. The values of n and α are retrieved from the Swanepoel model, ellipsometry and the Puma software. Figure C.5 and C.6, show the plots of n and α, respectively, for the wavelength range 200nm-800nm, obtained by ellipsometry and the Swanepoel model.

Due to an unsatisfying fit for all three models, the results of the annealed films containing more than 6% Fe are considered to be unreliable. Since the model results are

seen to be questionable, band gaps based on n and α from the models are chosen not been estimated for the annealed samples.

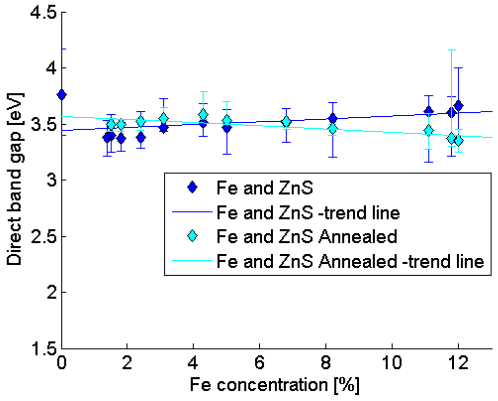

FIGURE C.1: An overview of the direct band gap of the samples deposited from Fe and ZnS, in addition to the direct band gaps of the annealed version of the same films. Direct Tauc plots based on the absorption calculated from the raw transmission measurements are used in the estimations.

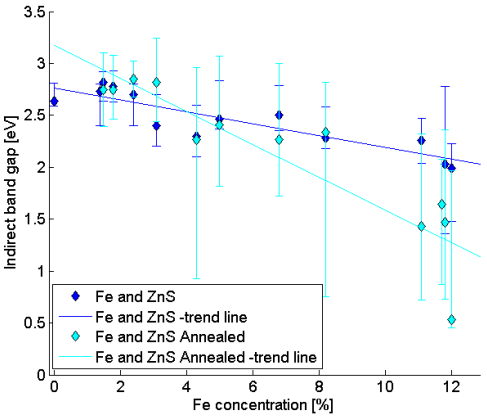

FIGURE C.2: An overview of the indirect band gap of the samples deposited from Fe and ZnS, in addition to the direct band gaps of the annealed version of the same films. Indirect Tauc plots based on the absorption calculated from the raw transmission measurements are used in the estimations.

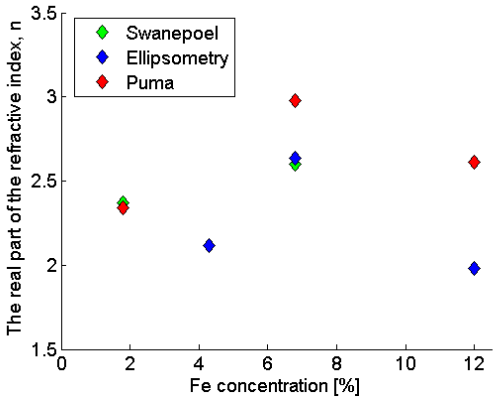

FIGURE C.3: An overview of the real part of the refractive index n of the annealed "Fe+ ZnS" films at a 1000 nm wavelength. The values are retrieved by the Swanepoel model, ellipsometry and the Puma model, indicated with green, blue and red colour, respectively. The samples containing more than 6% Fe have shown to be difficult to model with all three methods, indicating that the n-value of these films are questionable.

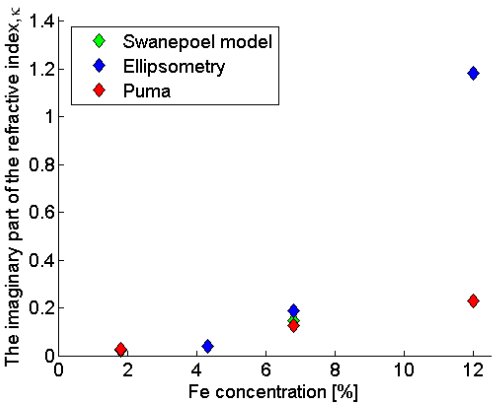

FIGURE C.4: An overview of the imaginary part of the refractive index κ of the annealed "Fe+ ZnS" films at a 1000 nm wavelength. The values are retrieved by the Swanepoel model, ellipsometry and the Puma model, indicated by green, blue and red colour, respectively. The samples containing more than 6% Fe have shown to be difficult to model with all three methods, indicating that the κ-value of these films are questionable.

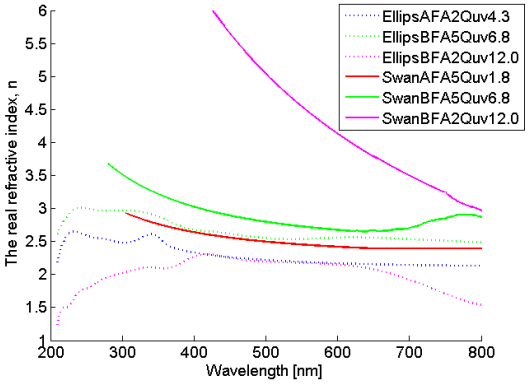

FIGURE C.5: The real part of the refractive index n estimated by ellipsometry and the Swanepoel method for selected samples. The annealed films were challenging to model, and the values of n are hence questionable.

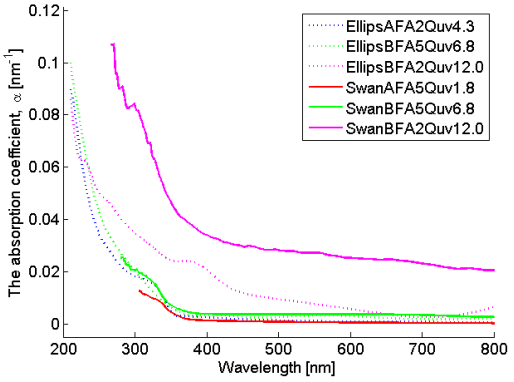

FIGURE C.6: The absorption coefficient α, representing the imaginary part of the refractive index, estimated by ellipsometry and the Swanepoel method for selected samples. The annealed films were challenging to model, and the values of α are hence considered to be questionable.

Appendix D

Reflection results

Due to imprecise values obtained for the absorption using the relation $A = 1 - R - T$, where R, T and A are being the reflection, transmission and absorption, respectively, the results based on this relation are presented in an appendix rather than in the report. As described in section 5.3.2.6, by expressing the absorption as $A = 1 - R - T$, a phase shift in R is ignored. This is unfortunate as the it becomes significant at low wavelengths where the value of κ in the refractive index is large. Applying a correction $\alpha = -1/d \cdot \ln(T/1 - R)$ at low wavelengths was however shown to be unsuccessful, indicating that including the phase shift seems to be a more challenging process. It is based on this discussion, that the band gap estimations resulting from the reflection measurements were chosen to be presented separately.

In figure D.1 - D.4 below, the measured reflectance and transmission spectra of investigated samples in addition to the absorption curve calculated from the relation $1 = R + T + A$ are plotted. The direct- and indirect band gaps of the samples resulting from the reflection measurements, are presented in series of "Fe + ZnS", "Fe + ZnS annealed" and "FeS + ZnS" given by figure D.11 -D.16. Direct- and indirect Tauc plots were used in the band gap estimations.

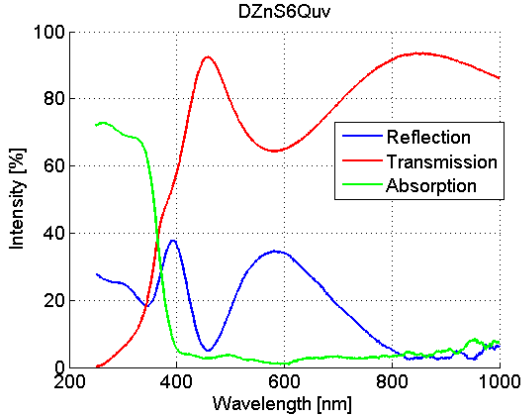

FIGURE D.1: The measured reflection and transmission spectra of sample DZnS6Quv consisting of pure ZnS, in addition to the absorption curve calculated from the relation $1 = R+T+A$.

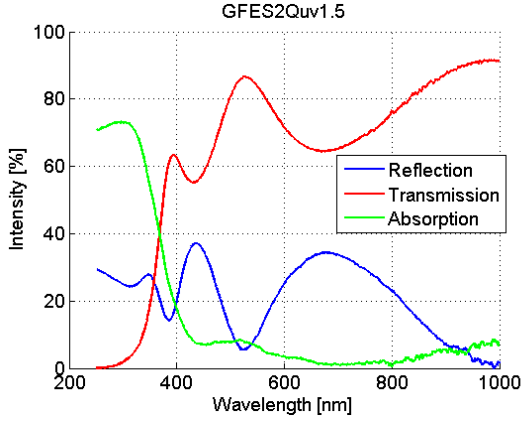

FIGURE D.2: The measured reflection and transmission spectra of sample GFES2Quv1.5, a mixed film of FeS and ZnS, in addition to the absorption curve calculated from the relation $1 = R + T + A$.

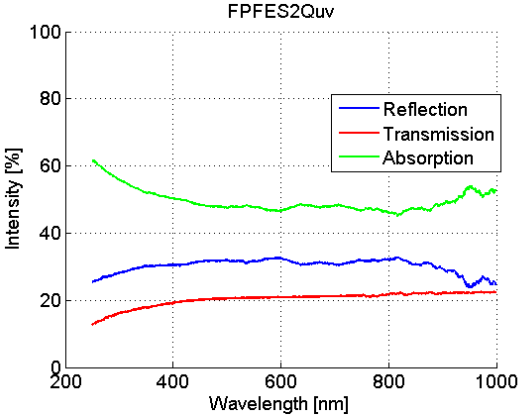

FIGURE D.3: The measured reflection and transmission spectra of sample FPFES2Quv consisting of pure FeS, in addition to the absorption curve calculated from the relation $1 = R + T + A$.

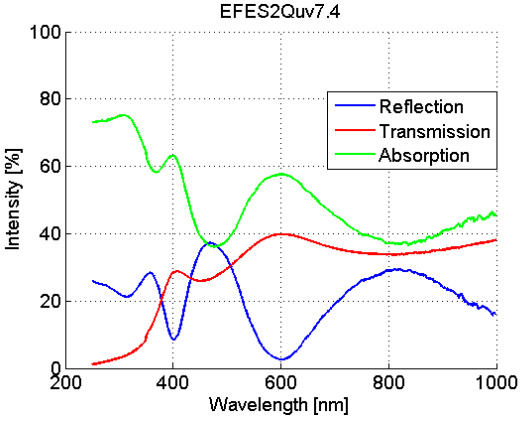

FIGURE D.4: The measured reflection and transmission spectra of sample EFES2Quv7.4, a mixed film of FeS and ZnS, in addition to the absorption curve calculated from the relation $1 = R + T + A$.

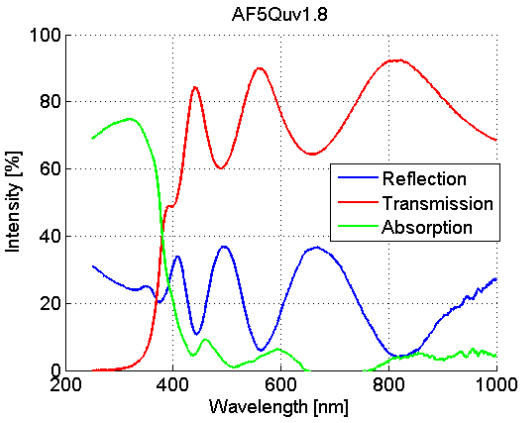

FIGURE D.5: The measured reflection and transmission spectra of sample AF5Quv1.8, deposited from Fe and ZnS, in addition to the absorption curve calculated from the relation $1 = R + T + A$.

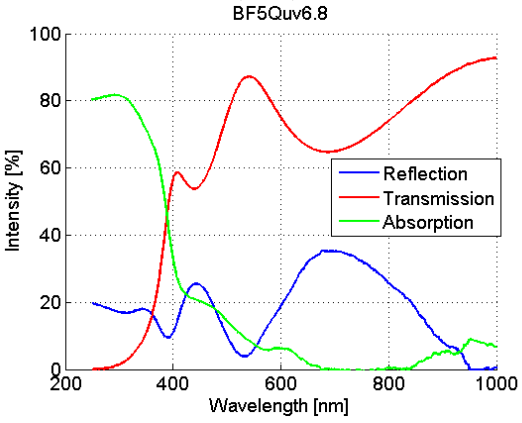

FIGURE D.6: The measured reflection and transmission spectra of sample BF5Quv6.8, deposited from Fe and ZnS, in addition to the absorption curve calculated from the relation $1 = R + T + A$.

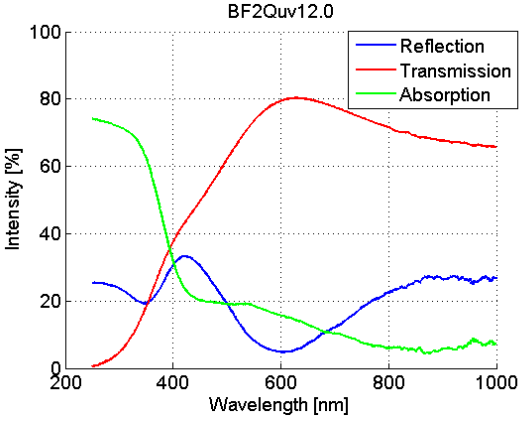

FIGURE D.7: The measured reflection and transmission spectra of sample BF2Quv12.0, deposited from Fe and ZnS, in addition to the absorption curve calculated from the relation $1 = R + T + A$.

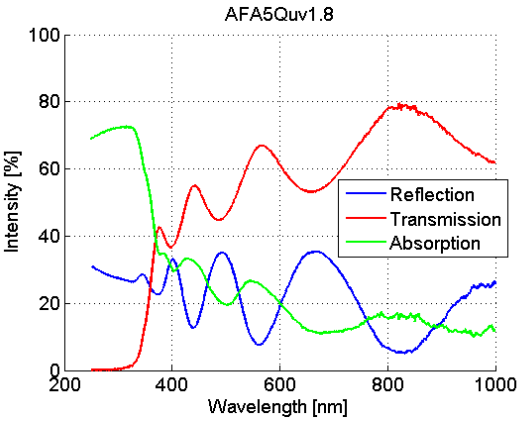

FIGURE D.8: The measured reflection and transmission spectra of sample AFA5Quv1.8, the annealed version of AF5Quv1.8, in addition to the absorption curve calculated from the relation $1 = R + T + A$.

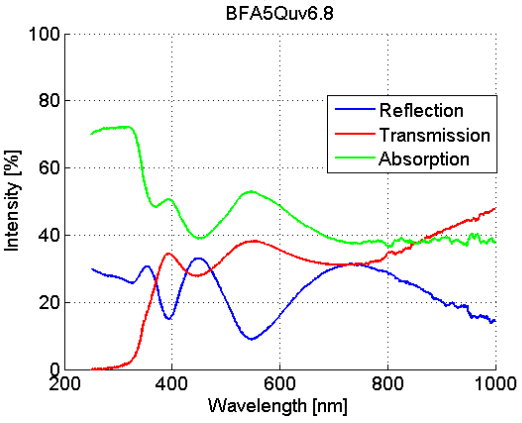

FIGURE D.9: The measured reflection and transmission spectra of sample BFA5Quv6.8, the annealed version of BF5Quv6.8, in addition to the absorption curve calculated from the relation $1 = R + T + A$.

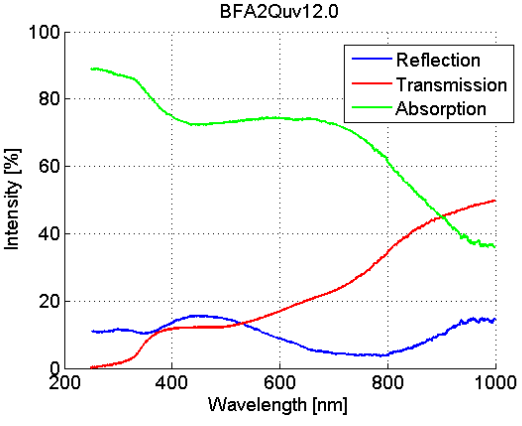

FIGURE D.10: The measured reflection and transmission spectra of sample BFA2Quv12.0, the annealed version of BF2Quv12.0, in addition to the absorption curve calculated from the relation $1 = R + T + A$.

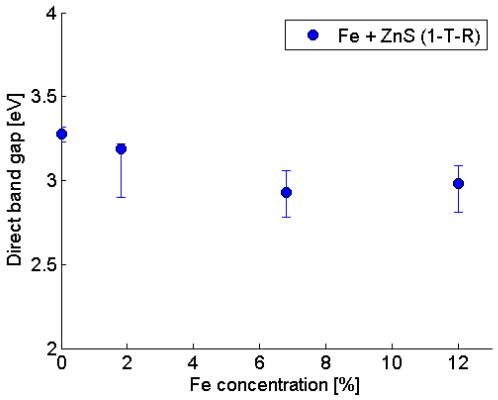

FIGURE D.11: The direct band gap of films deposited from Fe and ZnS. Direct Tauc plots based on the absorption calculated from the relation $1 = R + T + A$ are used in the estimations.

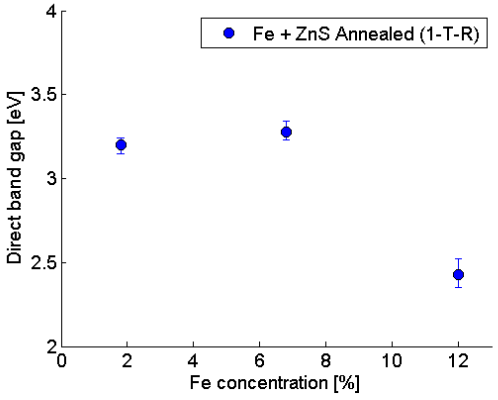

FIGURE D.12: The direct band gap of annealed films made from Fe and ZnS. Direct Tauc plots based on the absorption calculated from the relation $1 = R + T + A$ are used in the estimations.

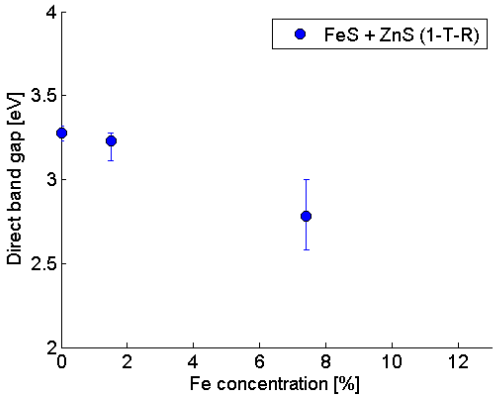

FIGURE D.13: The direct band gap of the mixed films made of FeS and ZnS. Direct Tauc plots based on the absorption calculated from the relation $1 = R + T + A$ are used in the estimations.

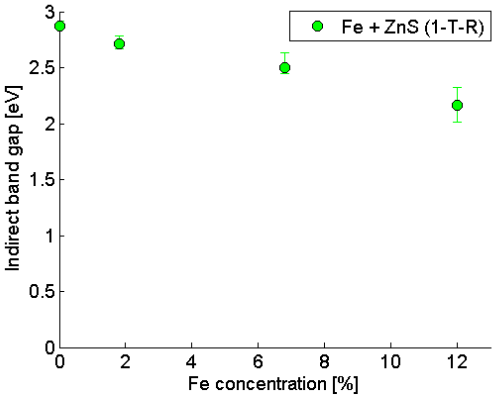

FIGURE D.14: The indirect band gap of films deposited from Fe and ZnS. Indirect Tauc plots based on the absorption calculated from the relation $1 = R + T + A$ are used in the estimations.

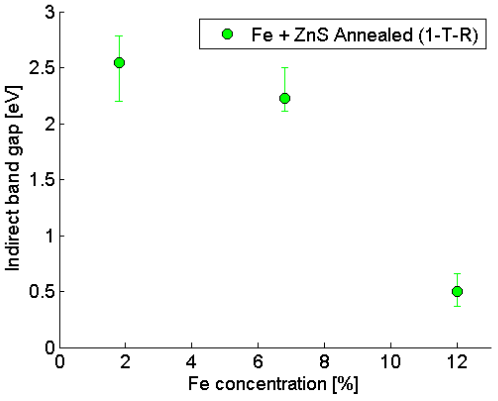

FIGURE D.15: The indirect band gap of annealed films made from Fe and ZnS. Indirect Tauc plots based on the absorption calculated from the relation $1 = R + T + A$ are used in the estimations.

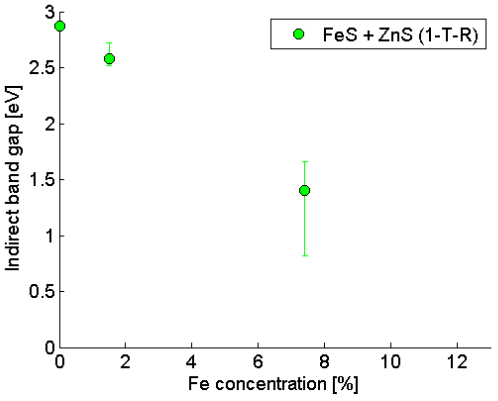

FIGURE D.16: The indirect band gap of the mixed films made of FeS and ZnS. Indirect Tauc plots based on the absorption calculated from the relation $1 = R + T + A$ are used in the estimations.

Appendix E

Matlab script, Swanepoel model

The code below corresponds to the Matlab© script used for the estimations of the complex refractive index by using the Swanepoel model [68]. The script loads the measured transmission and corresponding envelope curves, serving as input data, running the calculations and plots the results, according to the description found in section 5.3.2.5.

```
%%%%%%%%%%%%%%%%%%%%%%%%%%%%%%%%%%%%%%%%%%%%%%%%
%  The Swanepoel script of sample DZnS6Quv  %
%%%%%%%%%%%%%%%%%%%%%%%%%%%%%%%%%%%%%%%%%%%%%%%%

%Loading envelope curves and measured transmission spectrum
dataDZnS6Quv=load('DZnS6QuvTake2toMatlabFromDataThief.txt');
dataDZnS6QuvTransm=load('NA20140219sample6QuvAllWLT.txt');



data=dataDZnS6Quv;
dataTransm=dataDZnS6QuvTransm;

enpks=data(:,1); %energy values of the peaks [eV]
pks=data(:,2);   %transmission values of the peaks
enval=data(:,3); %energy values of the valleys [eV]
mins=data(:,4);  %transmission values of the valleys

lambdaTransm=dataTransm(:,1);%wavelengths in the transmission spectrum [nm]
enTransm=1240./lambdaTransm; %wavelengths converted to energies [eV]
measuredTransm=dataTransm(:,2);  %measured transmission
```

```
dDZnS6Quv=184; %The thickness of the film [nm]
d=dDZnS6Quv;

%Organizing the loaded data into vectors of equal lengths:
energy=linspace(enval(1),enval(length(enval)),800); %energy [eV]
lambda=1240./energy;                                %wavelength [nm]
TM=interp1(enpks,pks,energy);                       %upper envelope curve
Tm=interp1(enval,mins,energy);                      %lower envelope curve
measuredTransmEn=interp1(enTransm, measuredTransm, energy); %measured
                                                      %transmission curve

%Plotting input data; measured transmission and envelope curves:
figure(1);
clf;
hold on
plot(energy,TM,energy,Tm, 'k','linewidt', 2);
plot(enTransm, measuredTransm, 'g','linewidt', 2);
xlabel('Wavelength [nm]', 'fontsize', 14)
ylabel('Transmission', 'fontsize', 14)
title('Model input')
axis ([0 5 0 1]);


%======== Swanpoel determination of n and k ===========
%The Swanepoel method including formulas could be found in the following
%article:
%R. Swanepoel, "Determination of the thickness and optical constants
%of amorphous silicon", Journal of Physics E-Scientific Instruments,
%vol. 16, no. 12, p.1214-1222, 1983.

s=1.46; %Refractive index of quartz substrate
N=2*s*(TM-Tm)./(TM.*Tm) + (s.^2+1)/2;
n=(N+(N.*N-s.^2).^0.5).^0.5;   %The real refractive index estimated by
nOrig=n;                       %the Swanepoel method


%Loading n-values calculated from the first run of the model,
%to be used for the extrapolation of n at low wavelengths:
dataDZnS6QuvextrapN=load('DZnS6QuvExtrapInputTake2may6Lin.txt');
```

```
WLn=dataDZnS6QuvextrapN(:,1);
nExtrapIn=dataDZnS6QuvextrapN(:,2);
%After using the curve fitting tool "cftool" in Matlab on these data an
%extrapolation function of n was obtained:
npow=4.096e4.*lambda.^(-2) + 2.266;

%A modified version of n, n2, is assigned extrapolated values of
%n, npow, at low wavelengths and the original n-values, nOrig, estimated by
%Swanepoel at high wavelengths:
n2=zeros(1,length(lambda));
for i=1:length(lambda)
    if lambda(length(lambda) + 1 - i)<507
        n2(length(lambda) + 1 - i)=npow(length(lambda) + 1 - i);
    else if lambda(length(lambda) +1 - i)>507
        n2(length(lambda) + 1 - i)=nOrig(length(lambda) + 1 - i);
        end
    end
end
n=n2;


%The following expressions are used to calculate k:
Ti=2*(Tm.*TM)./(TM+Tm);
FOrig=8*nOrig.*nOrig*s./Ti;
F=8*n.*n*s./Ti;

%x=exp(-alpha*d) where d is the film thickness
x=(F-(F.*F-((n.*n-1).^3).*(n.*n-s^4)).^0.5)./((n-1).^3.*(n-s^2));
xOrig=(FOrig-(FOrig.*FOrig-((nOrig.*nOrig-1).^3)...
     .*(nOrig.*nOrig-s^4)).^0.5)./((nOrig-1).^3.*(nOrig-s^2));

%Calculating k, using the relation x=exp(-alpha*d):
alfa=-log(x)/d;
alfaOrig=-log(xOrig)/d;
k=(alfa.*lambda)./(4.*pi);
kOrig=(alfaOrig.*lambda)./(4.*pi);

%Values used for direct- and indirect Tauc plots, based on k calculated
%from the modified value of n:
```

```
ind=(alfa.*energy).^(0.5);
dir=(alfa.*energy).^2;

%Values used for direct- and indirect Tauc plots, based on the measured
%transmission data:
alfaT=((1/d).*log(1./measuredTransmEn));
indT=(alfaT.*energy).^(0.5);
dirT=(alfaT.*energy).^2;

%Back calculation of the transmission and the corresponding envelope curves
%based on the modified n-value:
A=16.*n.^2.*s;
B=(n+1).^3.*(n+s.^2);
C=2.*(n.^2-1).*(n.^2-s.^2);
D=(n-1).^3.*(n-s.^2);
phi=(4.*pi.*n.*d)./lambda;

T=(A.*x)./(B - C.*x.*cos(phi) + D.*x.^2);
TM2=(A.*x)./(B - C.*x + D.*x.^2);
Tm2=(A.*x)./(B + C.*x + D.*x.^2);

%Back calculation of the transmission and the corresponding envelope curves
%based on the original n-value:
AOrig=16.*nOrig.^2.*s;
BOrig=(nOrig+1).^3.*(nOrig+s.^2);
COrig=2.*(nOrig.^2-1).*(nOrig.^2-s.^2);
DOrig=(nOrig-1).^3.*(nOrig-s.^2);
phiOrig=(4.*pi.*nOrig.*d)./lambda;

TOrig=(AOrig.*xOrig)./(BOrig - COrig.*xOrig.*cos(phiOrig)+DOrig.*xOrig.^2);
TM2Orig=(AOrig.*xOrig)./(BOrig - COrig.*xOrig + DOrig.*xOrig.^2);
Tm2Orig=(AOrig.*xOrig)./(BOrig + COrig.*xOrig + DOrig.*xOrig.^2);



%Plotting the original n & k values in addition to
%the modified values of n & k:
figure(2)
clf;
hold on
```

```
plot(lambda,nOrig, 'b','linewidt', 2);
plot(lambda,n2, 'g','linewidt', 2);
plot(lambda,kOrig, 'r','linewidt', 2);
plot(lambda,k, 'k','linewidt', 2);
xlabel('Wavelength [nm]', 'fontsize', 14)
ylabel('The complex refractive index', 'fontsize', 14)
legend('nOrig', 'n modified', '\kappa from nOrig','\kappa from modified n')
axis ([250 1200 0 3.5]);
grid on
set(gca, 'fontsize', 14)

%Plotting the direct band gap based on the estimated k-value and the direct
%band gap based on alpha from the raw transmission measurements:
figure(3);
clf;
hold on
plot(energy, dir, 'b','linewidt', 2);
plot(energy, dirT, 'c','linewidt', 2);
title('Direct band gap', 'fontsize', 14);
axis ([0 6 0 0.01]);
xlabel('Energy [eV]', 'fontsize', 14)
ylabel('(\alpha hv)^{2} [eV nm^{-1}]^{2}', 'fontsize', 14)
legend('Swanepoel', 'Transmission');
grid on
set(gca, 'fontsize', 12)


%Plotting the indirect band gap based on the estimated k-value and the
%direct band gap based on alpha from the raw transmission measurements:
figure(4);
clf;
hold on
plot(energy,ind, 'b','linewidt', 2);
plot(energy,indT, 'c','linewidt', 2);
title('Indirect band gap', 'fontsize', 14);
%axis ([200 1200 0 3]);
xlabel('Energy [eV]', 'fontsize', 14)
ylabel('(\alpha hv)^{0.5} [eV nm^{-1}]^{0.5}', 'fontsize', 14)
legend('Swanepoel', 'Transmission');
```

```
grid on
set(gca, 'fontsize', 14)


%Plotting the back calculated transmission with corresponding envelope
%curves with respect to energy, in addition to the measured transmission:
figure(5);
clf;
hold on
plot(energy,Tm2,'k:','linewidt', 2);
plot(energy,TM2,'k:','linewidt', 2);
plot(enTransm, measuredTransm, 'g','linewidt', 2);
plot(energy, T, 'b', 'linewidt', 2);
xlabel('Energy [eV]', 'fontsize', 14)
ylabel('Transmission', 'fontsize', 14)
axis ([0.75 5 0 1]);
set(gca, 'fontsize', 14)


%Plotting the back calculated transmission with corresponding envelope
%curves with respect to wavelength, in addition to the measured
%transmission:
figure(6);
clf;
hold on
plot(lambda,Tm2,'k:','linewidt', 2);
plot(lambda,TM2,'k:','linewidt', 2);
plot(lambdaTransm, measuredTransm, 'g','linewidt', 2);
plot(lambda, T, 'b','linewidt', 2);
xlabel('Wavelength [nm]', 'fontsize', 14)
ylabel('Transmission', 'fontsize', 14)
axis ([200 1000 0 1]);
set(gca, 'fontsize', 14)
```

Appendix F

XRD datasheets

In the next pages the XRD datasheets containing the characteristic lines of wurtzite 2H, sphalerite and hexagonal iron sulfide could be found. The datasheets include 2θ within the approximate range 26 to 150°, in addition to the corresponding intensity, interplanar spacings and hkl-values of the XRD lines.

Pattern: PDF 00-036-1450 Radiation: 1.54060 Quality: Star (*)

Formula Zn S
Name Zinc Sulfide
Name (mineral) Wurtzite-2H, syn
Name (common)

Lattice: Hexagonal
S.G.: P63mc (186)

Mol. weight = 97.44
Volume [CD] = 79.12
Dx =
Dm = 4.09
I/Icor = -1.000

a = 3.82098
b =
c = 6.25730
a/b = 1.00000
c/b = 1.63762

alpha =
beta =
gamma =
Z = 2

Additional Patterns: To replace 00-005-0492 (3) and 00-010-0434 (4). See PDF 01-079-2204
Analysis: Previous spectrographic analysis at NBS, Gaithersburg, Maryland, USA, showed (wt %): 0.01 to 0.1 Cu; 0.001 to 0.01 each B, Fe, Mg, Si and <0.001 each Al and Ca
Color: Colorless
General Comments: Optical data on synthetic material. Other patterns are cited in (3)
Polymorphism/Phase Transition: A cubic form, sphalerite, also exists. ZnS exists in many polytypic forms (1,2)
Sample Source or Locality: Prepared by RCA Labs
Temperature of Data Collection: The mean temperature of data collection was 298.5 K
Unit Cell Data Source: Powder Diffraction

Primary Reference
Publication: Powder Diffr.
Detail: volume 1, page 77 (1986)
Authors: McMurdie, H., Morris, M., Evans, E., Paretzkin, B., Wong-Ng, W., Ettlinger, L., Hubbard, C.

Radiation: CuKα1
Wavelength: 1.54060
SS/FOM: 160.4 (0.0055;34)

Filter: M
d-spacing:

d	2θ	I	h	k	l
3.30992	26.915	100	1	0	0
3.12924	28.501	84	0	0	2
2.92592	30.528	87	1	0	1
2.27342	39.611	28	1	0	2
1.91027	47.562	81	1	1	0
1.76423	51.777	54	1	0	3
1.65434	55.501	11	2	0	0
1.63027	56.393	47	1	1	2
1.59943	57.581	12	2	0	1
1.56411	59.008	2	0	0	4
1.46263	63.559	6	2	0	2
1.41427	66.003	1	1	0	4
1.29605	72.932	15	2	0	3
1.25064	76.038	6	2	1	0
1.22637	77.822	9	2	1	1
1.21032	79.054	2	1	1	4
1.17062	82.299	11	1	0	5
1.16139	83.097	6	2	1	2
1.10309	88.583	9	3	0	0
1.07266	91.799	15	2	1	3
1.04283	95.235	3	0	0	6
1.04028	95.544	10	3	0	2
0.99819	101.013	7	2	0	5
0.99466	101.507	2	1	0	6
0.95527	107.485	5	2	2	0
0.91775	114.139	2	3	1	0
0.91537	114.601	5	1	1	6
0.91354	114.960	6	2	2	2
0.90806	116.052	2	3	1	1
0.90144	117.413	1	3	0	4
0.88465	121.089	8	2	1	5
0.88072	122.001	3	3	1	2

Pattern: PDF 01-071-5975 Radiation: 1.54060 Quality: Star (*)

Formula Zn S
Name Zinc Sulfide
Name (mineral) Sphalerite, syn
Name (common)

Lattice: Cubic
S.G.: F-43m (216)

Mol. weight = 97.44
Volume [CD] = 158.96
Dx = 4.07
Dm =
I/Icor = 8.490

a = 5.41700
b =
c =
a/b = 1.00000
c/b = 1.00000

alpha =
beta =
gamma =
Z = 4

ANX: AX
Delete duplicate: Delete: ICSD 2008/1 version removed this collection code. See PDF 01-077-2100 SK 1/09
ICSD Collection Code: 77089
Calculated Pattern Original Remarks: With anharmonic model R=0.0118 Cell at 423 K: 5.422, U(Zn)=.001630, U(S)=.001290, R=0.0194
Temperature of Data Collection: 295 K
Wyckoff Sequence: c a (F4-3M)

Structure
Publication: Kristallografiya
Detail: volume 42, page 649 (1997)
Authors: Rabadanov, M.Kh., Loshmanov, A.A., Shaldin, Yu.V.
Primary Reference
Publication: Calculated from ICSD using POWD-12++

Radiation: CuKα1
Wavelength: 1.54060
SS/FOM: 999.9 (0.0002;16)

Filter: Not specified
d-spacing:

d	2θ	I	h	k	l
3.12751	28.517	999	1	1	1
2.70850	33.046	87	2	0	0
1.91520	47.432	508	2	2	0
1.63329	56.280	300	3	1	1
1.56375	59.023	17	2	2	2
1.35425	69.333	59	4	0	0
1.24274	76.609	88	3	3	1
1.21128	78.979	13	4	2	0
1.10574	88.316	96	4	2	2
1.04250	95.275	53	5	1	1
0.95760	107.106	28	4	4	0
0.91564	114.549	52	5	3	1
0.90283	117.124	3	4	4	2
0.85650	128.147	42	6	2	0
0.82608	137.647	21	5	3	3
0.81664	141.210	1	6	2	2

Pattern: PDF 01-071-4469 Radiation: 1.54060 Quality: Star (*)

Formula Fe S
Name Iron Sulfide
Name (mineral)
Name (common)

Lattice: Hexagonal
S.G.: P63mc (186)

Mol. weight = 87.91
Volume [CD] = 60.36
Dx = 4.84
Dm =
I/Icor = 4.650

a = 3.44400
b =
c = 5.87600
a/b = 1.00000
c/b = 1.70616

alpha =
beta =
gamma =
Z = 2

ANX: AX
Analysis: Fe1 S1
Formula from original source: Fe S
ICSD Collection Code: 53528
Calculated Pattern Original Remarks: Fex S with x=0.94-1
Wyckoff Sequence: b a(P63MC)
Unit Cell Data Source: Single Crystal

Structure
Publication: Phys. Status Solidi A
Detail: volume 10, page 169 (1972)
Authors: Fasiska, E.J.
Primary Reference
Publication: Calculated from ICSD using POWD-12++

Radiation: CuKα
Wavelength: 1.54060
SS/FOM: 999.9 (0.0001;32)

Filter: Not specified
d-spacing:

d	2θ	I	h	k	l
2.98259	29.934	415	1	0	0
2.93800	30.400	61	0	0	2
2.65959	33.672	407	1	0	1
2.09307	43.188	999	1	0	2
1.72200	53.145	320	1	1	0
1.63720	56.133	62	1	0	3
1.49130	62.199	21	2	0	0
1.48563	62.463	15	1	1	2
1.46900	63.252	62	0	0	4
1.44547	64.404	41	2	0	1
1.32979	70.798	121	2	0	2
1.31783	71.538	44	1	0	4
1.18652	80.964	18	2	0	3
1.12731	86.205	6	2	1	0
1.11759	87.142	94	1	1	4
1.10712	88.177	31	2	1	1
1.09339	89.579	11	1	0	5
1.05250	94.088	71	2	1	2
1.04653	94.792	9	2	0	4
0.99420	101.573	25	3	0	0
0.97933	103.730	2	0	0	6
0.97704	104.072	20	2	1	3
0.94174	109.761	1	3	0	2
0.93046	111.761	33	1	0	6
0.92304	113.133	7	2	0	5
0.89433	118.930	6	2	1	4
0.86100	126.929	16	2	2	0
0.85129	129.609	4	1	1	6
0.82722	137.242	1	3	1	0
0.82625	137.587	2	2	2	2
0.82336	138.638	30	3	0	4
0.81915	140.228	21	3	1	1
0.81860	140.439	23	2	0	6
0.81353	142.474	13	2	1	5
0.80804	144.841	5	1	0	7

Bibliography

[1] T. Bergstresser and M. Cohen, "Electronic Structure and Optical Properties of Hexagonal CdSe, CdS, and ZnS," *Physical Review*, vol. 164, no. 3, p. 1071, 1967.

[2] W.H.Bloss, F.Pfisterer, H.W.Schock, "Advances in Solar Energy",*An Annual Review of Research & Development 4*, p. 275, 1988.

[3] N. Uzar, M. C. Arikan, "Synthesis and Investigation of Optical Properties of ZnS Nanostructures," *Bull. Mater. Sci.*, vol. 34, no. 2, p. 287-292, 2011.

[4] M. Ebrahim-Zadeh, I.T. Sorokina, "Mid-Infrared Coherent Sources and Applications", *Springer*, p. 225-260, 2007.

[5] A.B. Kashyout, A.S. Aric, G. Monforte, F. Crea, V. Antonucci, N. Giordano, "Electrochemical Deposition of ZnFeS Thin Film Semiconductors on Tin Oxide Substrates," *Solar Energy Materials and Solar Cells*, vol. 37, no. 1, p. 43-53, 1995.

[6] A.B. Kashyout, A.S. Aricb, N. Giordano, V. Antonucci, "Influence of Annealing Temperature on the Crystallographic and Optical Properties of Electrodeposited ZnFeS Thin Film Semiconductors," *Materials Chemistry and Physics*, vol. 41, no. 1 p 55-60, 1995.

[7] H.H. Guan, P.D. Han, Y.P. Li, X. Zhang, Q.N. Zhang, L.P. Wang, R.Z. Zhang, "Optimization of High Performance of ZnS/MgF_2 Ultraviolet Light-Emitting Diodes," *Optik - International Journal for Light and Electron Optics*, vol. 124, no. 3, p. 198-203, 2013.

[8] Q.J. Feng, D.Z. Shen, J.Y. Zhang, Y.M. Lu, Y.C. Liu, X.W. Fan, "Influence of Fe content on the Structural and Optical Properties of ZnFeS Thin Films," *Materials Chemistry and Physics*, vol. 96, no. 1, p. 158-162, 2006.

[9] A. Hoffmann, L Podlowski, P.Thurian, R.Heitz, I. Broser, F.Fuchs, P.koidl, "Energy Transfer Between Fe^{2+} Centers in Polymorphic ZnS," *Materials Science Forum*, vols. 143-147, p. 411-416, 1994.

[10] J. Nelson, *The Physics of Solar Cells*, Imperial College Press, 2004.

[11] C. Kittel, *Introduction to Solid State Physics*, Wiley, eighth ed., 2005.

[12] R.H. Misho, W.A. Murad, "Band Gap Measurements in Thin Films of Hematite Fe_20_3, Pyrite FeS_2 and Troilite FeS Prepared by Chemical Spray Pyrolysis",*Solar Energy Materials and Solar Cells*, vol. 27, no. 4, p.335-345, 1992.

[13] B.G streetman, S. Banerjee, *Solid State Electronic Devices*, Prentice Hall, fifth ed., 2000.

[14] K. Takahashi, A. Yoshikawa, A. Sandhu, *Wide Bandgap Semiconductors*, Springer, 2007.

[15] A. Hecht, *Optics*, Addison Wesley, fourth ed., 2002.

[16] V.G. Bessergeneva, E.N. Ivanovaa, Y.A. Kovalevskayaa, S.A. Gromilova, V.N. Kirichenkoa, S.M. Zemskovaa, I.G. Vasilievaa, B.M. Ayupova, N.L. Shwarz, "Optical and Structural Propertes of ZnS and ZnS:Mn Films Prepared by CVD Method", *Materials Research Bulletin*, vol. 30, no. 11, p. 1393-1400, 1995.

[17] M. H. Suhail, "Structural and Optical Properties of ZnS, PbS, $Zn_{1-x}Pb_xS$, $Zn_xPb_{1-x}S$ and $PbZn_xS_{1-x}$ Thin Films," *Indian Journal of Pure & Applied Physics*, vol. 50, p. 380-386, 2012.

[18] P.A.Luque, M.A.Quevedo-Lopez, A.Olivas, "Influence of Deposition Time on ZnS Thin Film Growth over SiO_2 and Glass Substrates", Materials Letters, vol. 106, p. 49-51, 2013.

[19] P. Kumar, A. Kumar, P. N. Dixit, T. P. Sharma, "Optical, Structural and Electrical Properties of Zinc Sulphide Vacuum Evaporated Thin Film", *Indian Journal of Pure & Applied Physics*, vol. 44, no.9, p. 690-693, 2006.

[20] C. Persson, C. Platzer-Björkman, J. Malmström, T. Törndahl, M. Edoff, "Strong Valence-Band Offset Bowing of $ZnO_{1-x}S_x$ Enhances *p*-type Nitrogen Doping of ZnO-like Alloys", *Physical Review Letters*, vol. 97, no. 14, p. 146403, 2006.

[21] R.K. Nkum, A.A. Adimado, H. Totoe, "Band Gap Energies of Semiconducting Sulphides and Selenides", *Materials Science and Engineering: B*, vol. 55, no. 1-2, p.102-108, 1998.

[22] A. Ates, M. A. Yỳldỳrỳm, M. Kundakcỳ, A. Astam, "Annealing and Light Effect on Optical and Electrical Properties of ZnS Thin Films Grown with the SILAR Method", *Materials Science in Semiconductor Processing*, vol. 10, no. 6, p.281-286, 2007.

[23] F. Göde, E. Güneri, A. Kariper, C. Ulutas, F. Kirmizigül, C. Gümüs, "Influence of Annealing Temperature on the Structural, Optical and Electrical Properties of Amorphous Zinc Sulfide Thin Films", *Journal of Physics: Conference Series*, vol. 326, no. 012020, 2011.

[24] S. B. Mirov, V. V. Fedorov, D. V. Martyshkin, I. S. Moskalev, M. S. Mirov, V. P. Gapontsev, "Progress in Mid-IR Cr^{2+} and Fe^{2+} Doped II-VI Materials and Lasers [Invited]", *Optical Materials Express*, vol.1, no. 5, p. 898-910, 2011.

[25] V.I. Kozlovsky, Yu.V. Korostelin, A.I. Landman, V.V. Mislavskii, Yu.P. Podmar'kov, Ya.K. Skasyrsky, M.P. Frolov, "Pulsed Fe^{2+} : ZnS Laser Continuously Tunable in the Wavelength Range of 3.49 - 4.65 μm, *Quantum electronics*, vol. 41, no. 1, p. 1-3, 2011.

[26] L. D. DeLoach, R. H. Page, G. D. Wilke, S. A. Payne, and W. F. Krupke, "Transition Metal-Doped Zinc Chalcogenides: Spectroscopy and Laser Demonstration of a New Class of Gain Media," *IEEE J. Quantum Electron*, vol. 32, no. 6, p. 885-895, 1996.

[27] J.H. Zhang, J.W. Ding, J.X. Cao, Y.L. Zhang, "Infrared, visible and ultraviolet absorptions of transition metal doped ZnS crystals with spin-polarized bands", *Journal of Solid State Chemistry*, vol. 184, no. 3, p.477-480, 2011.

[28] P. C. Lin, C. C. Hua, T. C. Lee, "Low-Temperature Phase Transition of ZnS: The Critical Role of ZnO", *Journal of Solid State Chemistry*, vol. 194, p. 282-285, 2012.

[29] L. Qi, G. Mao, J. Ao, "Chemical Bath-Deposited ZnS Thin Films: Preparation and Characterization", *Applied Surface Science*, vol. 254, no. 18, p. 5711-5714, 2008.

[30] M. Zaien, N. M. Ahmed, Z.Hassan, "Effects of Annealing on the Optical and Electrical Properties of CdO Thin Films Prepared by Thermal Evaporation", *Materials Letters*, vol. 105, p. 84-86, 2013.

[31] M. K. Hatalis, D. W. Greve, "Large Grain Polycrystalline Silicon by Low-Temperature Annealing of Low-Pressure Chemical Vapor Deposited Amorphous Silicon Films", *Journal of Applied Physics*, vol. 63, no. 7, p. 2260-2266, 1988.

[32] Y. Saeed, S. Nazir, A. H. Reshak, A. Shaukat, "First-Principles Study of Spin-Polarized Electronic Band Structures in Ferromagnetic $Zn_{1-x}TM_xS$ (TM = Fe, Co and Ni)", *Journal of Alloys and Compounds*, vol. 508, no. 2, p. 245-250, 2010.

[33] C. Persson, C. Platzer-Björkman, J. Malmström, T. Törndahl, and M. Edoff, "Strong Valence-Band Offset Bowing of $ZnO_{1-x}S_x$ Enhances p-Type Nitrogen Doping of ZnO-like Alloys", *Physical Review Letters*, vol. 97, no. 14, p. 146403-1 - 146403-4, 2006.

[34] T. Zdanowicz, T. Rodziewicz, M. Zabkowska-Waclawekb, "Theoretical Analysis of the Optimum Energy Band Gap of Semiconductors for Fabrication of Solar Cells for Applications in higher Latitudes Locations", *Solar Energy Materials and Solar Cells*, vol. 87, no. 1-4, p. 757-769, 2005.

[35] C. Tablero, "Survey of Intermediate Band Materials Based on ZnS and ZnTe Semiconductors", *Solar Energy Materials and Solar Cells*, vol. 90, no. 5, p. 588-596, 2006.

[36] http://en.wikipedia.org/wiki/File:Solar_Spectrum.png, 10.04.14.

[37] R.H. Misho, W.A. Murad, "Band gap Measurements in Thin Films of Hematite Fe_20_3, Pyrite FeS_2 and Troilite FeS Prepared by Chemical Spray Pyrolysis", *Solar Energy Materials and Solar Cells*, vol. 27, no. 4, p. 335-345, 1992.

[38] J. Ganem, S.R. Bowman, "Use of Thulium-Sensitized Rare Earth-Doped Low Phonon Energy Crystalline Hosts for IR Sources", *Nanoscale Research Letters*, vol. 8, no. 455, 2013.

[39] T.S Navruz, M. Saritas, "The Detailed Analysis of Auger Effect on the Efficiency of Intermediate Band Solar Cells", *Solar Energy Materials and Solar Cells*, vol. 93, no. 11, p. 1913-1922, 2009.

[40] R. Sharma, H.S. Bhatti, "Photoluminescence Decay Kinetics of Doped ZnS Nanophosphors", *Nanotechnology*, vol. 18, no. 46, 2007.

[41] M. Wei, J. Yang, Y.Yan, J. Cao, Q. Zuo, H. Fu, B. Wang, L. Fan, "The Investigation of the Maximum Doping Concentration of Iron in Zinc Sulfide Nanowires, and its Optical and Ferromagnetic Properties", *Superlattices and Microstructures*, vol.54, p. 181-187, 2013.

[42] J. Xiao, A. Kuc, S. Pokhrel, M. Schowalter, S. Parlapalli, A. Rosenauer, T. Frauenheim, L. Mädler, L.G.M. Pettersson, T. Heine, "Evidence for Fe^{2+} in Wurtzite Coordination: Iron Doping Stabilizes ZnO Nanoparticles", *Small*, vol. 7, no. 20, p. 2879-2886, 2011.

[43] D. Mattox, *Handbook of Physical Vapor Deposition (PVD) processing*, William Andrew, second ed., 2010.

[44] Y. Waseda, E. Matsubara, K. Shinoda, *X-Ray Diffraction Crystallography: Introduction, Examples and Solved Problems*, Springer, 2011.

[45] J. Als-Nielsen, D. McMorrow. *Elements of Modern X-ray Physics*. Jon Wiley & Sons, Ltd, 2011.

[46] A.J. Garratt-Reed, D.C. Bell, *Energy-Dispersive X-ray Analysis in the Electron Microscope*, BIOS Scientific Publishers Ltd, 2003.

[47] D.P. Woodruff, T.A. Delchar,*Modern Techniques of Surface Science*, Cambridge university press, 1986.

[48] C. D. Wagner, W. M. Riggs, L. E. Davis, J. F. Moulder, G. E. Mullenberg, *Handbook of X-ray Photoelectron Spectroscopy*, Perkin-Elmer Corporation, 1979.

[49] A.D Rakić, "Algorithm for the Determination of Intrinsic Optical Constants of Metal Films: Application to Aluminum", *Applied Optics*, vol. 34, no. 22, p. 4755-4767, 1995.

[50] *Easy-to-Use Acquisition/Analysis Software for Spectroscopic Ellipsometry (EASE)*, J. A. Woollam Co., Inc., version 2.30.

[51] R.M.A. Azzam, N.M Bashara, *Ellipsometry and polarized light*, Elsevier Science B.V., 1987.

[52] H.G. Tompkins, E.A. Irene, *Handbook of Ellipsometry*, William Andrew Publishing, 2005.

[53] B. Swatowska, T.Stapinski, S. Zimowski, "Properties of a-Si:N:H Films Beneficial for Silicon Solar Cells Applications", *Opto-Electronics Review*, vol. 20, no. 2, p. 168-173, 2012.

[54] S. Riepe, I.E Reis, W. Kwapil, M.A Falkenberg, J. Schon, H. Behnken, J. Bauer, D. Kressner-Kiel, W. Seifert, W. Koch, "Research on Efficiency Limiting Defects and Defect Engineering in Silicon Solar Cells - Results of the German Research Cluster SolarFocus", *Physica Status Solidi C-Current Topics in Solid State Physics*, vol. 8, no. 3, p.733-738, 2011.

[55] Thermo Nicolet Corporation, *Introduction to Fourier Transform Infrared Spectrometry*, 2001, (http://mmrc.caltech.edu/FTIR/FTIRintro.pdf).

[56] B. Fultz, J.M. Howe, *Transmission Electron Microscopy and Diffractometry of Materials*, Springer, 2008.

[57] E.J Samuelsen, *Materials physics: Structure, Diffraction, Imaging and Spectroscopy -Lecture notes*, Department of Physics NTNU, 2006.

[58] http://www.dataq.com/products/software/acquisition.htm

[59] A. Green, K. Emery, Y. Hishikawa, W. Warta, E. D. Dunlop, "Solar Cell Efficiency Tables (version 43)", *Progress in photovoltaics: research and applications*, vol. 22, no. 1 p. 1-9, 2014.

[60] S. L. Diedenhofen, G. Grzela, E. Haverkamp, G. Bauhuis, J. Schermer, J. Rivas, "Broadband and Omnidirectional Anti-Reflection Layer for III/V Multi-Junction Solar Cells", *Solar Energy Materials & Solar Cells*, vol. 101, p. 308-314, 2012.

[61] T.C Chiang, F.J Himpsel, "2.1.22 ZnS.", A. Goldmann, E.-E. Koch (ed.), *Springer-Materials -The Landolt-Börnstein Database* (http://www.springermaterials.com)

[62] A. Luque, A. Martí, "Increasing the Effciency of Ideal Solar Cells by Photon Induced Transitions at Intermediate Levels", *Physical Review Letters*, vol. 78, no. 26, p. 5014-5017, 1997.

[63] http://www.mathworks.se/

[64] J. Twidell, T. Weir, *Renewable Energy Resources*, Taylor & Francis, second ed., 2006.

[65] J. Szlufcik, S. Sivoththaman, J. F. Nijs, R. P. Mertens, R. Van Overstraeten, "Chapter IB-3 Low-Cost Industrial Technologies for Crystalline Silicon Solar Cells", *Practical Handbook of Photovoltaics. Fundamentals and Applications*, second ed., p. 129-159, 2012.

[66] W. Schockley, H. Queisser, "Detailed Balance Limit of Efficiency of p-n Junction Solar Cells", *Journal of Applied Physics*, vol. 32, no. 3, p. 510-519, 1961.

[67] M. Green, "Third Generation Photovoltaics: Solar Cells for 2020 and Beyond", *Physica E: Low-dimentional Systems and Nanostructures*, vol. 14, no. 1-2, p. 65-70, 2002.

[68] R. Swanepoel, "Determination of the Thickness and Optical Constants of Amorphous Silicon", *Journal of Physics E-Scientific Instruments*, vol. 16, no. 12, p.1214-1222, 1983.

[69] E.G. Birgin, I. Chambouleyron, J.M Martinez, "Estimation of the Optical Constants and the Thickness of Thin Films using Unconstrained Optimization", *Journal of Computational Physics*, vol. 151, no. 2, p.862-880, 1999.

[70] N.M Saeed, "Structural and Optical Properties of ZnS Thin Films Prepared by Spray Pyrolysis Technique", *Journal of Al-Nahrain University*, vol.14, no. 2, p. 86-92, 2011.

[71] V. Sa-Yakanit, H.R. Glyde, "Urbach Tails and Disorder", *Comments Condensed Matter Physics*, vol. 13, no. 1, p. 35-48, 1987.

[72] A. Abbad, S. Bentata, H. A. Bentounes, W. Benstaali, and B. Bouadjemi, "Study of Electronic and Magnetic Properties of Binary Zinc Sulfide and Ternary Manganese-

and Iron-Substituted Alloys," *Materials Science in Semiconductor Processing*, vol. 16, no. 3, p. 576-581, 2013.

[73] E.D. Palik, *Handbook of Optical Constants of Solids*, Academic Press Inc, 1985.

[74] M.S. Kim, K.G. Yim, S. Kim, G. Nam, D.-Y. Lee, Jin Soo Kim, Jong Su Kim, J.-Y. Leem, "Growth and Characterization of Indium-Doped Zinc Oxide Thin Films Prepared by Sol?Gel Method", *Acta Physica Polonica A*, vol. 121, no. 1, p. 217-220, 2012.

[75] F. Urbach, "The Long-Wavelength Edge of Photographic Sensitivity and of the Electronic Absorption of Solids", *Physical Review*, vol. 92, no. 5, p. 1324, 1953.

[76] B. Pejova, "The Urbach-Martienssen Absorption Tails in the Optical Spectra of Semiconducting Variable-Sized Zinc Selenide and Cadmium Selenide Quantum Dots in Thin Film Form", *Materials Chemistry and Physics*, vol. 119, no. 3, p.367-376, 2010.